Investigation of Solar Power Tower System for Mass Injera Baking and Cooking Application – a Case of Senkale Military Camp

By

Motuma Lema Yebessa

Adviser: Dr. Addisu Bekele

Thesis Submitted to the Department of Mechanical Engineering

School of Mechanical, Chemical and Materials Engineering

Office of Graduate Studies

Adama Science and Technology University

May 2024

Adama, Ethiopia

Investigation of Solar Power Tower System for Mass Injera Baking and Cooking Application – a Case of Senkale Military Camp

By

Motuma Lema Yebessa

Adviser: Dr. Addisu Bekele

Thesis Submitted to the Department of Mechanical Engineering School of Mechanical, Chemical and Materials Engineering

Presented in Partial Fulfillment of the Requirement for the Degree of Master of science in Thermal Engineering

Office of Graduate Studies

Adama Science and Technology University

May 2024

Adama, Ethiopia

DECLARATION

I hereby declare that this Masters of thesis entitled ***"****Investigation of Solar Power Tower System for Mass Injera Baking and Cooking Application – a Case of Senkale Military Camp****"*** is my original work. That is, it has not been submitted for the award of any academic degree, diploma or certificate in any other university. All relevant resource information used in this paper has been duly acknowledged.

Motuma Lema Yebessa

Name of Student	Signature	Date

RECOMMENDATION OF ADVISOR

I, the advisor of this thesis, hereby certify that I have read the revised version of the thesis entitled *"Investigation of Solar Power Tower System for Mass Injera Baking and Cooking Application – a Case of Senkale Military Camp"* prepared under my guidance by Motuma Lema Yebessa submitted in partial fulfillment of the requirements for the degree of Master of Science in Thermal Engineering**.** Therefore, I recommend the submission of revised version of the thesis to the department following the applicable procedures.

Dr. Addisu Bekele		
Name of Advisor	Signature	Date

APPROVAL BAGE

I, the advisor of the thesis entitled hereby *"Investigation of Solar Power Tower System for Mass Injera Baking and Cooking Application – a Case of Senkale Military Camp"* and developed by Motuma Lema Yebessa, hereby certify that the recommendation and suggestions made by the board of examiners are appropriately incorporated into the final version of the thesis.

Dr. Addisu Bekele	______________	______________
Name of Advisor	Signature	Date

We, the undersigned members of the Board of Examiners of the thesis by Motuma Lema Yebessa have read and evaluated the thesis entitled "*Investigation of Solar Power Tower System for Mass Injera Baking and Cooking Application – a Case of Senkale Military Camp*" and examined the candidate during open defense. Therefore, this is to certify that the thesis is accepted for partial fulfillment of the requirement of the degree of Master of Science in Thermal Engineering.

______________________________	______________	___________
Chairperson	Signature	Date
______________________________	______________	___________
Internal Examiner	Signature	Date
______________________________	______________	___________
External Examiner	Signature	Date

Final approval and acceptance of this thesis proposal is contingent upon submission of its final copy to the Office of Postgraduate Studies (OPGS) through the Department Graduate Council (DGC) and School Graduate Committee (SGC).

______________________________	______________	___________
Head of Department	Signature	Date
______________________________	______________	___________
School Dean	Signature	Date
______________________________	______________	___________
Office of Post Graduate Studies, Dean	Signature	Date

ACKNOWLEDGEMENT

First and foremost, I want to express my gratitude to the Almighty God for giving me the inspiration, strength, and support I have required thought my life.

With great appreciation, I would like to thank Dr. Addisu Bekele, my adviser, for his continuous support, encouragement, insightful feedback, and guidance during my thesis study. It would have been challenging to finish this thesis without his worthwhile advice, continuous support, and kind assistance.

Additionally, I want to express my gratitude to all of my closest friends for their support, advice, and help as well as for their perceptive comment on my work. I would also like to thank Adama Science and Technology University for providing me with a full scholarship to study master's program.

Lastly, I would want to express my sincere gratitude to my family for their inspiration, helpful advice, and support during difficult moments and throughout my life.

TABLE CONTENTS

LIST OF FIGURES

LIST OF TABLES

LIST OF ACRONYMS

Symbol	Description
BCR	Benefit-cost ratio
CPC	Compound parabolic collectors
CSP	Concentrating Solar Power
DR	Daily range temperature of the day
FPC	Flat plate collectors
GHGs	Greenhouse Gases (GHGs).
HTF	Heat Transfer Fluid
LFR	Linear Fresnel Reflector
NPV	Net present value
PTSC	Parabolic Trough Solar Collectors
SPT	Solar Power Towers
TES	Thermal Energy Storage

GREEK LETTER

α	Thermal diffusivity
β	Coefficient of thermal expansion
ρ	Density of clay
μ	Dynamic viscosity
υ	Kinematics' viscosity
ρ	Reflectivity
α	Absorbance
θ	Angle of incidence
ϕ	Latitude
β	Slope
γ	Surface azimuth angle
γ_s)	Solar azimuth angle
θ_z	Zenith
δ	Declination
ω	Hour angle

LIST OF NOMENCLATURES

$T_{am,min}$	Mean daily temperature of the day.
$t_{h,max}$	Times for the occurrence of daily maximum temperatures
C_{pj}	Specific heat of the components of the food
X_j	Percentage composition of the components
m_w	Mass of water vapour
T_{bt}	Boiling temperature of water
T_r	Room temperature
h_{fg}	Latent heat of vaporization
C_{pw}	Specific heat capacity of water
m_{pan}	Mass of pan
$C_{p,pan}$	Specific heat of pan
T_h	Required baking temperature
T_i	Initial temperature of Pan
R_{cond}	Conductive resistance
$R_{conv(in)}$	Internal convection resistance
$R_{rad(ext)}$	External radiative resistance
$R_{con(ext)}$	External convection resistance
K_{air}	Thermal conductivity of the air
Ψ^*_{rec}, Ex_{in}	Exergy of receiver
$\Psi^*_{rec,abs}$	Exergy of heat transfer fluid
$\eta_{I,rec}$	Receiver energy efficiency
$\eta_{II,rec}$	Receiver exergy efficiency
$\Psi^* = Ex_{solar}$	Exergy of heliostat field
H_{tower}	Solar tower height

ABSTRACT

Every human being requires energy for many purposes throughout their existence. Cooking is one of the most energy-required activities. The main sources of energy used for cooking are electricity, natural gas, and biomass. Another promising option for supplying the energy requirement is solar energy. Performance analysis of a solar power tower for mass injera baking is the main goal of this thesis project. Main components of the system are the tower, receiver, high temperature thermal fluid reservoir, baking pan assembly, cold temperature working fluid reservoir, and connecting pipes. Steam or water was used as the heat transfer fluid for this project.

The amount of injera necessary, which is provided to the members twice a day, and the energy required to bake the injera are taken into consideration while designing the chosen solar collector. The solar energy is collected and delivered to the receiver tube by the solar collectors and then HTF (water) is cycled via the baking unit and receiver tube to supply thermal energy to the pan. Utilizing Soltrace and SAM software, the solar field layout and tower height optimization were carried out to enhance outlet temperatures, optical efficiency, and receiver efficiency. Based on the results, the optimal tower height to balance performance and cost is between 55-75 meters. And also for the month of November, the solar collector's maximum outlet HTF temperature, optical efficiency, and receiver efficiency were measured to be 556.78℃, 73.36%, and 65.85%, respectively. At solar noon, when sun irradiation is at its peak, useful energy is 19.267MW, while useful exergy is 13.443MW.

The analysis of mita) pre-heating time, injera baking time, and reheating time was done using transient heat transfer modeling with Python software. The outcome indicates that Mitads need 2 to 3 minutes to bake injera, with a 12.5-minute to preheat mitad to 200°C and a 2.5-minute reheat in between batches. Furthermore, the effects of pan thickness on heating time were also investigated. According to the findings, it takes 12 seconds for a pan with a thickness of 0.004 m to reach the baking temperature, whereas it takes 761 seconds for a pan with a thickness of 0.02 m.

Lastly the project is economically feasible and within eight years and seven months, the project pays for its original investment, according to the results of the economic analysis that was completed.

Keywords: *Injera baking, Solar Power Tower, Biomass, Deforestation, solar noon*

CHAPTER ONE

INTRODUCTION

1.1 Background

Energy is vital to a country's industrial, social, technological, and economic development. Though energy services are essential to all civilizations for meeting basic needs like cooking, lighting, movement, communication, etc., greenhouse gas emissions associated with the provision of energy services are believed to be the main cause of climate change. In developing countries, biomass is the primary energy source (Group, 2013).

Energy sources come in two varieties: renewable and non-renewable. The globe is currently concentrating on mitigating environmental issues by raising energy quality and reducing carbon emissions, in addition to making a concentrated effort to use various sorts of resources. In emerging nations, household energy use makes for over 30% of total energy use. A significant portion of residential energy consumption in these countries comes from cooking, which is one of the most energy-intensive daily tasks (Newell et al., 2019).

If new renewable and cleaner energy sources are not exploited, the number of people who rely on biomass for cooking due to population expansion would increase to 2.7 billion by 2030 (Adem & Ambie, 2017). A more long-term approach would seem to be to use appropriate energy technology designs to utilize other locally available and renewable energy supplies. Among alternative energy sources, solar energy is a clean, abundant, and convenient renewable energy source.

Injera is a circular, savory, sour pancake with a distinct flavor. Its diameter is around 58 centimeters, and its thickness ranges from 2 to 4 millimeters. Injera's primary ingredient is teff, however barley and sorghum are also occasionally used. To make injera whiter these days, some consumers choose to add a few grams of rice flour (Adem & Ambie, 2017).

Injera is made by combining teff flour, water, and starter (batter left over from the previous baking session) and letting it ferment. Once the pan reaches a temperature of approximately 200 °C, the dough will be poured onto the baking pan. It doesn't need to be rolled out because of the viscosity; it may just be poured into the baking pan. The injera will then be taken out of the oven and placed on a serving plate.

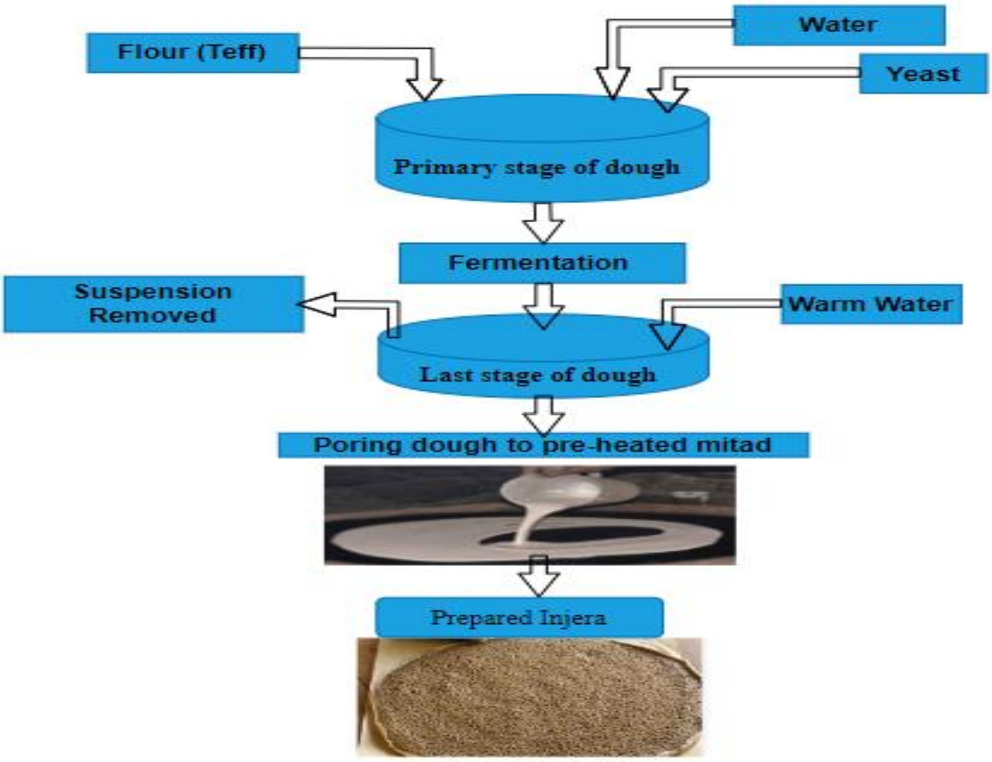

Figure 1. 1: Injera Baking Process (Negash et al., 2021)

1.2 Injera Baking Technology

1.2.1 Biomass Injera stove

Three-stone, Mirt, and Gonzie Injera stoves are the three biomass Injera stoves now in use in Ethiopia.

A. Open Fire Baking Technique

An open-fire stove, also known as a three-stone stove, uses three different stones to support the mitad (clay pan) when baking. Depending on the stones' availability, different stone types and sizes are used. The mitad is often supported by three stones, each measuring 10 to 15 cm high. An open-fire stove with three stones had an average specific fuel consumption of 929 g of wood/kg of injera when tested using the Controlled Cooking Test (CCT) method (Adem & Ambie, 2017).

Figure 1. 2: Three-stone fire baking stove (Adem & Ambie, 2017)

B. Mirt improved Injera Stove

The stove is made up of four cylindrical enclosure parts that are 18–24 cm tall and have a thickness of 4-6 cm. It also has an expansion chamber and a very short chimney that can fit a frying pan or pot (Liyew et al., 2021)

Figure 1. 3: Mirt improved biomass stove (Adem & Ambie, 2017)

1.2.2 Electric Injera stove

The previous Ethiopian Electric Light and Power Authority (EELPA) brought the electric Injera baking baker, also known as the electric Injera Mitad, to Ethiopia forty years ago. The electric Injera stove was produced and marketed to the market by several public and private enterprises. An electric stove used for baking injera in a single-family typically uses 3 to 4 kW of power. (Mulugeta, 2020)

Figure 1. 4: Electric Injera Stove (Adem & Ambie, 2017)

1.2.3 Solar Injera Baking stove

Of all the renewable energy sources, solar energy has the most potential, and even if it is only used in tiny amounts, it will be a significant source of energy. A system of reflectors is used in solar cooking to direct sun energy onto a cooking vessel, where it is transformed into heat energy for cooking (Adem & Ambie, 2017). The steam is supplied to the injera baking stove via a pipe, and when it condenses, it transfers heat to the baking pan that is set on the steel plate that is in touch with the steam (Asfafaw et al., 2019).

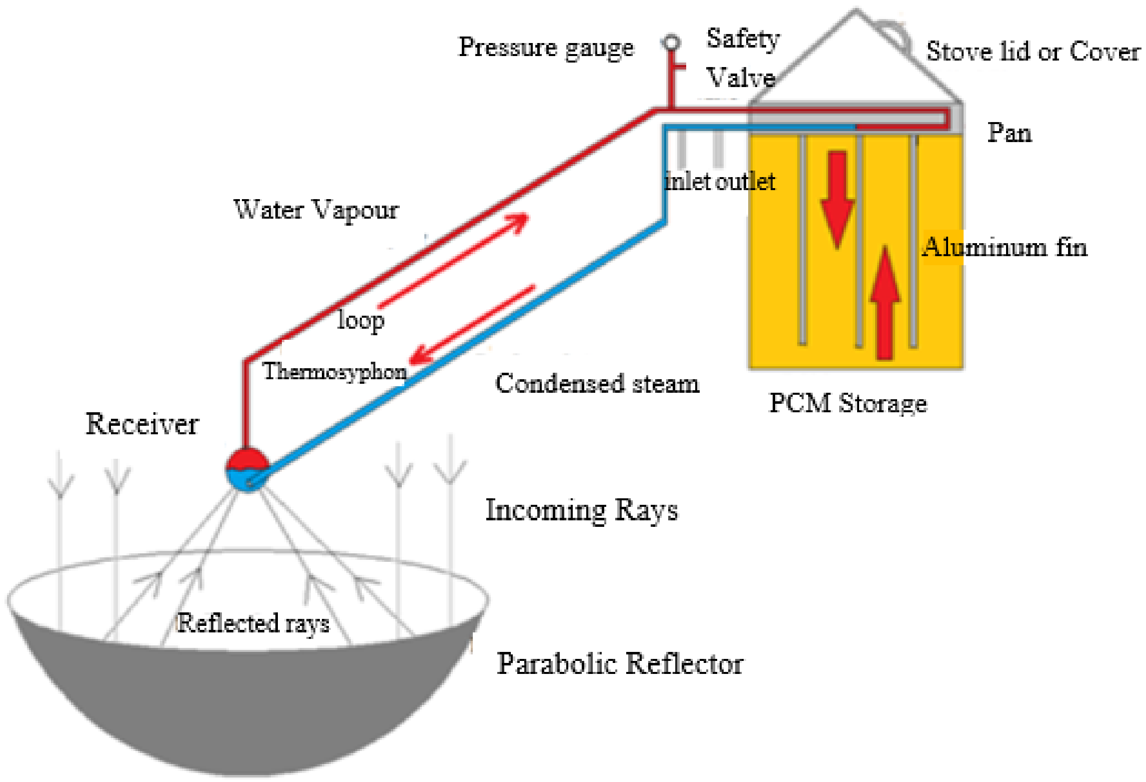

Figure 1. 5: Solar injera baking stove (Asfafaw et al., 2019)

1.3 Problem statement

The problem addressed in this research pertains to the injera baking practices in military camps in Ethiopia, particularly the Senkale Military Camp. While a few camps have access to electricity for baking injera, the majority rely on biomass, specifically firewood, due to limited electricity availability. Firewood is collected from Jibat Forest, located 57.3 km away from Ambo Town, or purchased from the local market for baking injera in this camp. However, the unrestricted use of firewood for baking injera leads to various environmental challenges.

The primary concerns associated with firewood usage include deforestation, both locally and globally, as well as indoor and outdoor air pollution, and the emission of CO2, which contributes to climate change. Women who bake injera are particularly vulnerable to harmful smoke emissions, leading to respiratory problems and other health issues. Although using electricity can mitigate the problems of carbon dioxide inhalation and deforestation, it presents challenges such as high costs and unexpected power fluctuations.

The use of solar energy as an alternative energy source for baking injera at the Senkale Military Camp is suggested by this research as a solution to these problems. Various domestic solar collectors have been developed as a result of numerous studies that have sought to address this issue. But the large-scale mass production of injera is a serious problem that needs to be addressed. Using a central receiver collector or a solar power tower, this approach aims to lessen the aforementioned issue.

1.4 The objective of the study

1.4.1 General Objective

The general objective of this study is the design and investigation of a Solar Power Tower system for steam generation for mass injera baking and cooking applications.

1.4.2 Specific Objectives

The study's specific objectives are:

- To design a solar power tower system and Injera baking stove.
- To model and Simulate the solar power tower and baking unit by varying input variables.
- To evaluate energy and exergy analysis of the system.
- To perform economic analysis of the system

1.5 The Scope and Limitations of the study

The scope of this research encompasses the design and material selection process for both a Solar Power Tower system and an Injera baking mitad. It involves the following key components:

- Design and Material Selection: This phase focuses on designing the Solar Power Tower system and the mitad, while carefully selecting suitable materials for each component. The aim is to ensure optimal performance and efficiency in both systems.
- Mathematical Modeling: Mathematical models are developed to accurately represent the behavior and characteristics of the mitad.
- Solar potential estimation and thermo- physical properties of injera
- Software Simulation: The Solar Power Tower system was simulated using SOLTRACE software, which provides a comprehensive analysis of its performance

and behavior. On the other hand, the transient behavior of the mitad was simulated using Python code, allowing for a detailed examination of its thermal characteristics and performance under varying conditions.

- Economic analysis: Economic analysis is conducted in order to know feasibility of the project using SAM and Solar Pilot software.
- The lack of experimentation limits the research because there is a lack of money and a high number of systems.

1.6 Significance of the study

This work is significant because it has the potential to address the following important issues: women's health, environmental cleanliness, and free energy.

- Free and Sustainable Energy: By harnessing solar power for injera baking, the dependence on expensive and environmentally damaging biomass or electricity is reduced. Additionally, reducing deforestation associated with firewood collection helps combat climate change and air pollution.

- Empowering Women: Replacing traditional cooking methods with solar technology specifically addresses the health risks faced by women who are exposed to harmful smoke emissions while cooking with traditional methods.

- Energy independence for the Senkale military camp: By providing an alternate energy source for injera baking, this system offers the camp greater energy independence and reduces dependence on external resources.

1.7 Outline of the study

This thesis contains seven chapters. In Chapter Two, a literature review is presented, covering topics such as solar energy, solar collectors, and solar injera baking. Chapter Three delves into the materials and methods employed to accomplish the research objectives. Chapter Four explores the estimation of solar potential, along with the thermo-physical properties of injera. Chapter Five delves into the energy demand, as well as the design and performance analysis of the system. Chapter Six encompasses the presentation and discussion of various results. Finally, Chapter Seven concludes the report by offering recommendations for future work.

CHAPTER TWO

LITRETURE REVIEW

2.1 Introduction

Reducing carbon emissions is a global issue because carbon dioxide makes up the majority of greenhouse gases (GHGs). In this case, a variety of strategies, such as promoting renewable energy sources and technical advancements, could be used to lower carbon emissions (Abolhosseini et al., 2014). Renewable energy sources are those that replace themselves naturally without depleting the earth, such as hydropower, geothermal energy, solar energy, wind energy, and ocean energy (tide and wave) (Owusu & Asumadu-Sarkodie, 2016).

2.2 Solar Energy

Energy that can be obtained directly from the Sun is known as solar energy. The reason people can survive on Earth is due to the presence of a greenhouse gas atmosphere (GHG) in the region between the Sun and the planet. The source of all Earth's renewable energy sources that meet human needs is the Sun (Tiwari & Tiwari, 2016)

Solar energy is a good substitute for fossil fuels because of its many benefits, including low long-term costs, environmental friendliness, and adaptability (Guangul & Chala, 2019).

2.2.1 Application of Solar Energy

Applications for solar energy have increased globally since it can be used to produce heat, electricity, and desalinate water, among other things (Maka & Alabid, 2022). Concentrated solar power (CSP), also referred to as solar thermal systems, uses solar radiation to create electricity similarly to solar cells. Sunlight is directed onto a receiver in most solar thermal systems, which uses a solar collector with a mirrored surface to heat a liquid. The superheated liquid is used in a manner similar to coal plants to produce steam, which produces electricity (Sharma et al., 2015).

2.2.2 Solar Thermal Collector

A device that absorbs sunlight and transfers that energy to a heat transfer fluid (HTF) flowing inside the device is referred to as a solar collector (Barone et al., 2019).

(Kalogirou, 2004) Solar collectors come in two varieties: stationary and concentrating. The stationary solar collectors don't follow the sun; instead, they are fixed in place constantly. With the use of mirrors or lenses, solar energy can be reflected or refracted to achieve concentration.

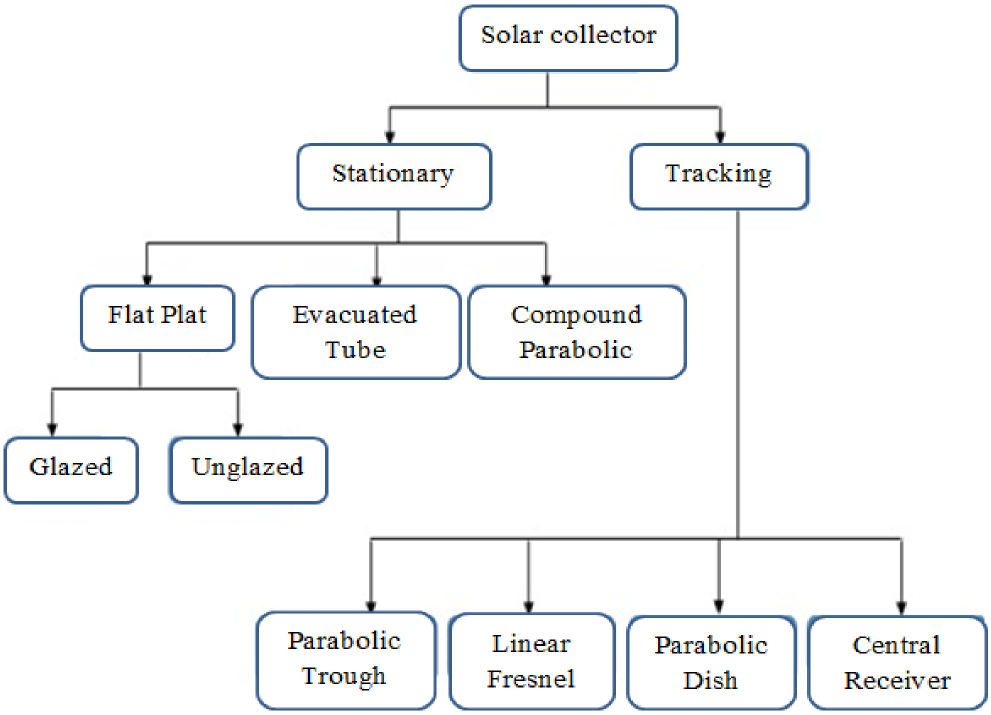

Figure 2. 1: Main classification of solar collector (Sonawane & Bupesh Raja, 2018)

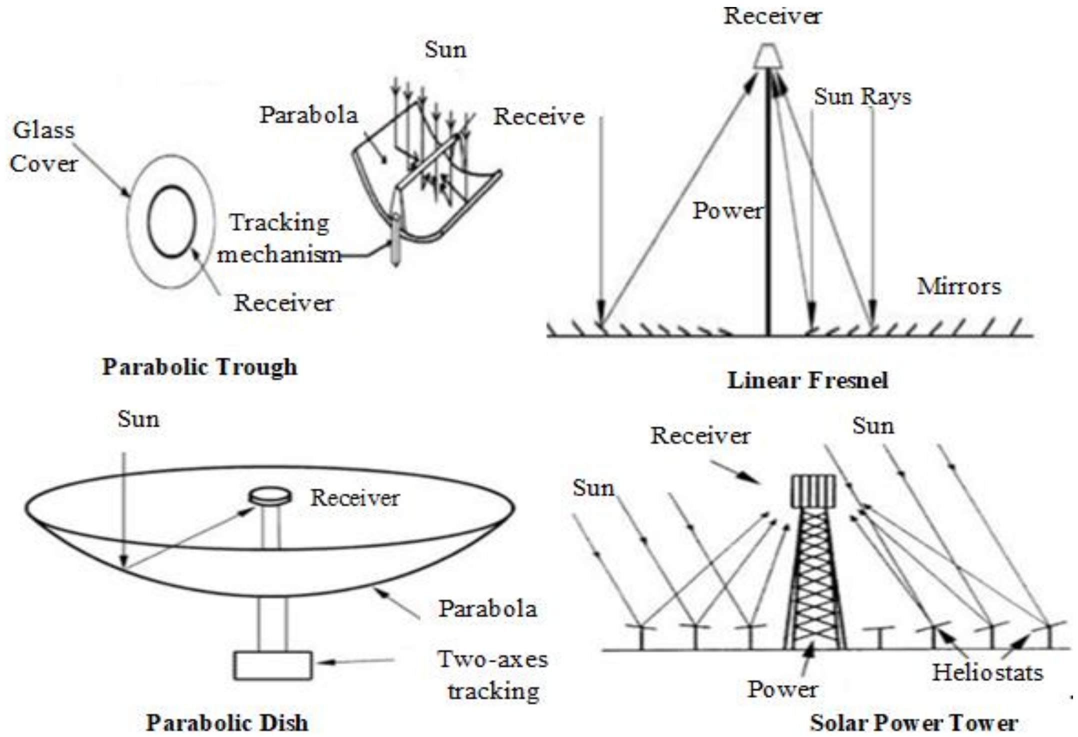

Figure 2. 2: Four main types of solar concentrators (Chu & Meisen, 2011)

Table 2. 1: Solar energy collectors with their respective temperatures (Kalogirou, 2003).

Motion	Collector type	Absorber type	Concentration ratio	Indicative temperature range (°C)
Stationary	Flat plate collector (FPC) Evacuated tube collector (ETC) Compound parabolic collector (CPC)	Flat Flat Tubular	1 1 1–5	30–80 50–200 60–240
Single-axis tracking	Fresnel lens collector (FLC) Parabolic trough collector (PTC) Cylindrical trough collector (CTC)	Tubular Tubular Tubular	10–40 15–45 10–50	60–250 60–300 60–300
Two-axes tracking	Parabolic dish reflector (PDR) Heliostat field collector (HFC)	Point Point	100–1000 100–1500	100–500 150–2000

2.3 Solar Power Tower

Solar radiation is directed toward a central receiver situated on top a tower by a heliostat field in Solar Power Towers (SPT), often referred to as Central Receiver Systems (CRS). Using two axes, these heliostats follow the Sun (Merchán et al., 2021). A huge number of heliostats with independent two-axe tracking systems circle a central tower in the system (Sonawane & Bupesh Raja, 2018). The most recent technology in comparison to PTC technology is tower power technology. Large-scale utility power plants use TSP technology because it is less expensive than PTC and LFC (Sonawane & Bupesh Raja, 2018).

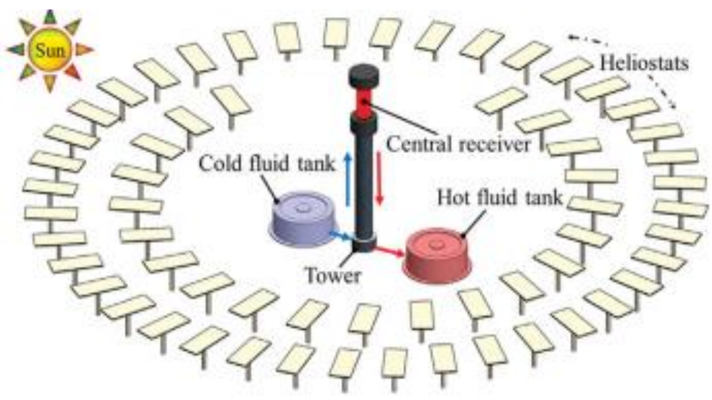

Figure 2. 3: Central receiver tower (Suman et al., 2015)

2.3.1 Components of power tower

The main components of solar towers include Heliostat, central receiver, and Tower (Hassan, 2016).

A. Tower

The tower's main function is to maintain the receiver on top of it. It needs to have room for the receiver's storage tank. The tower's height is the primary design factor.

B. Receiver

Receivers are the most crucial components in concentrated solar power systems because they convert concentrated radiation into heat. The ability of the central receiver to transform focused radiation into heat energy conveyed by the heat transfer fluid determines its energy performance. The primary sources of loss at the receivers are radiation and the convection of the heat into the air. Utilizing a selective coating reduces losses brought on by radiation and reflection.

C. Heliostat

A heliostat is a mirror that tracks the sun's path to continually reflect solar radiation onto the central receiver. The heliostats must follow the sun in order to reflect its rays onto the receiver since the sun moves while the tower remains stationary (Hassan, 2016). These mirrors must be wind-resistant, and have low specific costs in addition to having good reflectivity. Many variables affect the heliostats field's performance, such as shade, cosine, reflectivity, cleanliness, blockage, atmospheric, and spillage losses.

2.3.2 Classification of receiver

For liquid HTFs, there are only two different kinds of receiver designs: cavity and external (Slootweg et al., 2019).

A. External receiver

For the heliostats, external receivers have been created to maximize the receiver's exposure to reflected radiation from all directions (Slootweg et al., 2019).

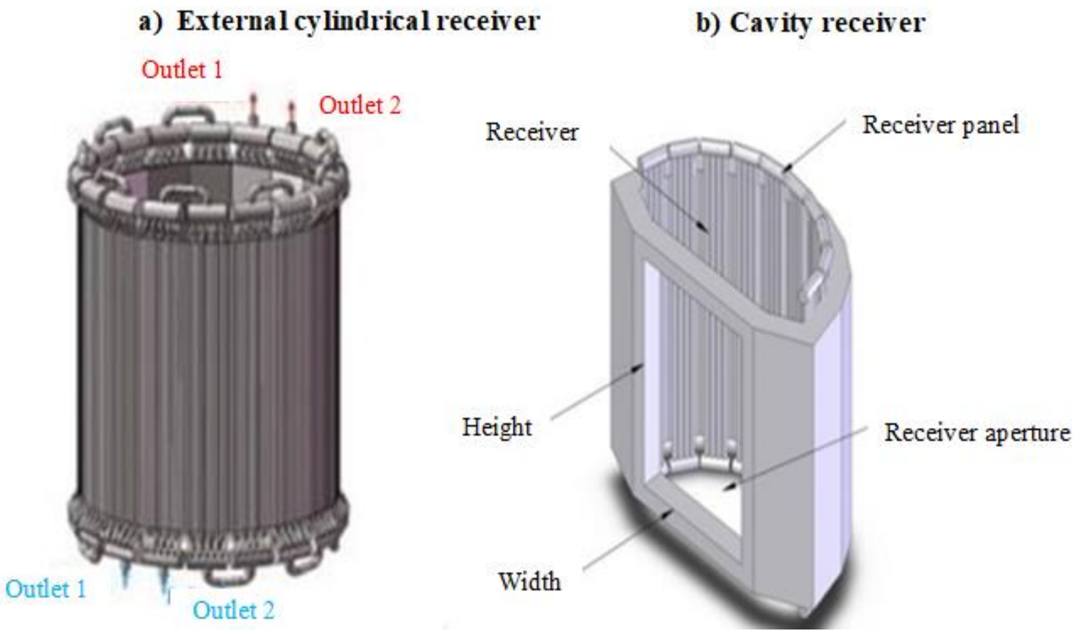

Figure 2. 4*:* Two types of receivers (Kulkarni et al., 2021) (Li et al., 2010)

B. Cavity receiver

This receiver's absorber features tubular panels like the external receiver and is enclosed in a structure that only has one aperture through which concentrated rays can enter (Slootweg et al., 2019). The disadvantage is that the receiver can only receive polar fields due to its small acceptance angle for focused photons.

2.3.3 Heliostat field layout

The primary objective of the heliostat field layout design is to locate the receiver and the mirrors in a particular land region (Zhou & Zhao, 2014). The number and location of heliostats in the solar field determine how much heat is useable at the receiver (Telsnig et al., 2017). In power tower solar collectors, cornfield and radial stagger are two common field layout designs (Srilakshmi et al., 2015).

I. Cornfield

The term "cornfield layout" describes an arrangement in which the heliostats are placed one behind the other in straight rows (Srilakshmi et al., 2015). The rectangular cornfield layout, sometimes called the North-South cornfield layout, is a setup in which heliostats are placed in straight rows and columns in a rectangular array. The rectangular cornfield configuration has the lowest blocking efficiency of any heliostat field type (Rizvi et al., 2021).

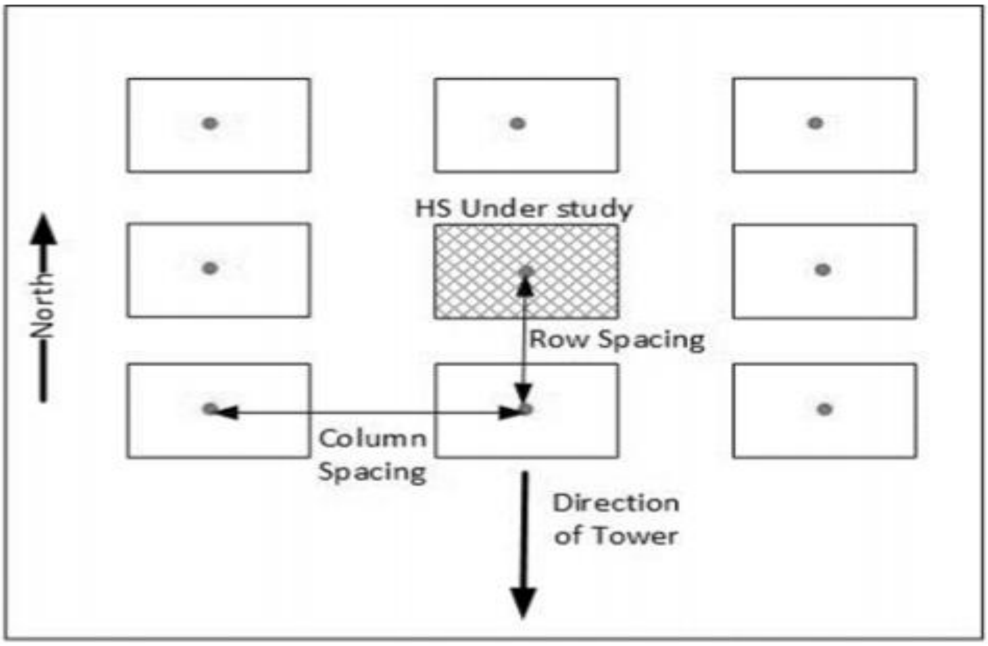

Figure 2. 5: Construction of north–south rectangular cornfield layout (Rizvi et al., 2021).

II. Radial staggered

In this layout, the tower is surrounded by a circle of heliostats. They are often used in plants that have cavity receivers with northern fields or external cylindrical receivers with surrounding field layouts (Srilakshmi et al., 2015). The majority of heliostat field layout ideas use a radial stagger pattern because each heliostat can move freely and suggested that the radial staggered design be used to decrease blocking and shadowing losses (Wah & Kyaing, 2017).

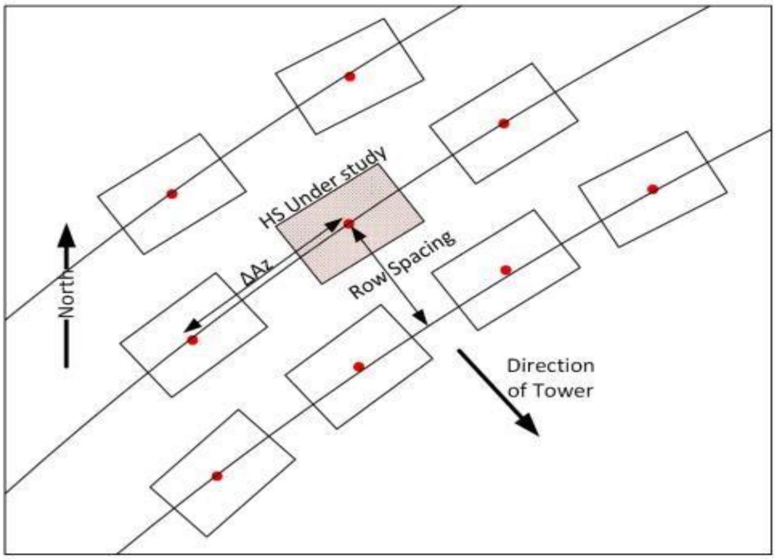

Figure 2. 6: Construction of a radial staggered layout (Rizvi et al., 2021).

2.4 Solar Cookers

Cooking using solar energy is not only economical but also ecologically sustainable, with the potential to reduce the amount of dirty energy sources used for cooking globally by at least 38% on average. Gathering solar radiation and transferring it to food ingredients is necessary for solar cooking in order to cook food items as efficiently as possible (Kanyowa et al., 2021).

2.4.1 Types of Solar cookers

Depending on how heat is delivered to the cooking vessel, solar cookers can be divided into two groups: direct and indirect (Aramesh et al., 2019) (Farooqui, 2014).

A. Direct Solar Cookers

In the direct cooking method, the cooking vessel is heated directly by sunlight without the need of a heat-transfer fluid. Direct solar cookers consist of box, panel, and focused cookers (Herez et al., 2018).

B. Indirect Solar Cookers:

It needs a heat-transferring medium in this kind of cooker for the heat to reach the cooking utensils because the cooking vessel is physically separated from the heat source. Flat plate collectors, evacuated tube collectors, and concentrating type collectors are among the commercially accessible cookers in this class (Muthusivagami et al., 2010).

Larger solar cookers in the form of boxes have been tested by a few organizations (Indora & Kandpal, 2018). According to various institutes that have tested larger-sized box-type solar cookers, the SBC is the ideal method for cooking small amounts of food to suit residential requirements.

2.5 Institutional Solar Cookers and related review

Solar cookers can be either domestic or commercial, depending on the amount of food required. A household is made up of one or more individuals who eat meals together and reside in the same home (Lizaso, 2020). The number of meals prepared in institutional kitchens might range from 25 to a few thousand.

(Kanyowa et al., 2021) Using a Scheffler dish-type solar thermal cooking system, the performance of the system was evaluated analytically and experimentally in order to identify the areas of the system where heat losses are occurring. The device can cook up to 6000 meals a day and generates 3 to 12 kg/cm2 of steam daily. 28 collectors are arranged in the system so that two Scheffler reflectors may be seen. It was demonstrated through experimentation that collectors with an average direct normal irradiation of 800 W/m2 had 70–80% thermal efficiency. The system's estimated 25% overall efficiency indicates significant losses across the entire process.

For institutional solar cooking applications, the Ministry of New and Renewable Energy (MNRE) in India primarily promotes three types of concentrators (Indora & Kandpal, 2018). These include, manually tracked elliptical paraboloid dishes (SK type, PRINCE type), ii) The fixed focus E-W automatically tracked elliptical paraboloid dishes, also known as the Scheffler dish; iii) dual-axis entirely tracked Fresnel paraboloid dishes, also known as the ARUN® dish.

(Muthu & Raman, 2006) in order to improve the future and ensure energy security, large-scale organizations like Tirupathi Devasthanam in Andhra Pradesh and the Brahma Kumari Ashram in Mount Abu have started using solar energy for cooking. The Brahma Kumari Ashram's system consisted of 84 improved parabolic concentrators and it can generate up to 3500 kg of steam per day and prepare meals twice daily for 10,000 people. The sun's reflected light from 84 concentrators is concentrated onto 42 (shell type) receivers with a 35cm diameter, with one parabola reflecting from a higher location to the front side of the receiver and another parabola reflecting from a lower position. When it comes to Tirumala Tirupathi Devasthanam, each unit of the concentrator was connected to a shared steam pipeline that went into the kitchen. The system is made to produce more than 4000 kg of steam every day, enough to cook two meals for roughly 15,000 people, at a temperature of 1800°C and 10 kg/cm2. It is composed of 106 automatically tracked parabolic concentrators.

(Ktistis et al., 2021) the largest soft drink facility in Cyprus implemented the country's first industrial PTC system. The system consists of concrete thermal energy storage (CTES), a steam generator, and 288 m2 of PTC. Two operation methods were created in order to accomplish that, and the system's main CPU controls them both automatically. When there is a need for steam, the first approach is activated, and when the energy can be directly stored in the CTES, the second strategy is activated. The PTC system can produce 940 litters of steam each day, and the HTF is being heated from the CTES to 236 C when Strategy 1 is used, and it can store 107.3 KWh_{th}, and the CTES temperature grew from 290 C to 348 C on a day with an average Direct Normal Irradiance (DNI) of 753 W/m2, when Strategy 2 is used, according to tests of both strategies.

2.6 Solar Injera Baking Related Review

(Abdulkadir et al., 2011) The performance of an injera baking oven that runs on solar power and transfers heat energy to the kitchen through a heat-transfer fluid is suggested and examined. Based on the experimental results, it was found that heating oil to 300°C required about an hour, and it needed 40 minutes to attain the ideal temperature for baking. Every two minutes, injera are taken out of the baking pan and let to come back to the ideal baking temperature for three minutes. About three hours and twenty-eight minutes can be spent baking twenty injera every day, assuming a typical family size. Thus, the suggested system, which runs on solar energy, can effectively bake 20 injera every day.

(Bhave & Kale, 2020) It has been successfully demonstrated that a heat storage/cooking device with fins to increase the rate of heat transmission and solar salt as the PCM for high-temperature cooking is viable. In the experiments, a charge of heat took about 110 minutes to store when beam radiation was available continually on the parabolic dish. When cooking inside, the ideal frying temperature of 170–180 C for the oil was easily attained and consistently maintained by heat transfer from the PCM's frozen state to the cooking vessel through the fins.

(Asfafaw et al., 2019) has illustrated the concept of employing heat storage that has been charged by a solar concentrator to bake bread. Heat-conducting fins on the baking plate extend into the latent heat reservoir. During heat collecting and baking, respectively, these fins facilitate the storage's charge and discharge processes. It also showed that injera could be baked at temperatures between 110 and 150 degrees Celsius, instead of 180 to 220 degrees Celsius as previously believed, as long as there is sufficient and rapid heat transfer during baking.

(Bonsa, 2020) Functionality of a solar parabolic trough collector and the projected thermal energy storage's charging process has been studied using the one-dimensional explicit Finite Difference approach.

The four sun-tracking methods were compared in order to determine which configuration would yield the most energy accumulation. The numerical calculation's result shows that in order to achieve the demand, 277 cylindrical capsules containing 168.1 kg of PCM and four parallel parabolic trough solar collectors are required.

(YOHANES, 2020) the design and practical testing of a solar thermal injera baking system with a 2 m2 parabolic dish collector, working fluid (heated oil), thermal energy storage (PCM) sun salt (60%NaNO3/40%KNO3), and wood ash insulation has been completed. From 2:00 to 11:00 local time, measurements of the ambient temperature (22 to 30 °C), solar radiation (371 to 946 w/m2), receiver surface temperature (193 to 306 °C), and fluid temperature (164 to 254 °C) were made. According to the analysis's results, the receiver's thermal efficiency was 51.44%, its pan heat-up time was 10-15 minutes, its retention time was 3-5 minutes, and its heating time after one lap was 2-3 minutes. The pan's top and bottom surfaces were both warm, at temperatures of 179.5°C and 214.3°C, respectively.

(Seid, 2021) It was intended to develop and test an experimental solar bread-baking system employing 10 kg of D-mannitol, which melts at 440.15K, for heat storage. The findings demonstrated that, for PTC, the maximum thermal efficiency, maximum outlet HTF temperature, and maximum energy efficiency are 456.45K, 51.9%, and 28.5%, respectively. These values are 469.85K, 55.2%, and 31.1%, and 465.25K, 53.6%, 29.7%, with receiver fins. Obtaining a 433K baking plate surface temperature required 55 minutes of baking.

(Jemal et al., 2022) investigated the use of copper-oil and aluminum oxide-oil nanoparticles to enhance the functionality of a parabolic trough solar-powered injera baking pan. And he obtained that the greatest value for the copper-oil solar collector efficiency was 0.3% volume concentration, which was above 60% approximately. Aluminum oxide oil had about 56% efficiency compared to ordinary oil's 48% efficiency. Copper oil was 43% more thermally efficient on average than aluminum oxide oil. The heating gain time for copper oil and aluminum oxide working fluid dropped from the original 26 min (0.05%) to 19 min (0.3%) and from the original 27 min (0.05%) to 21 min (0.3%), respectively. For copper-oil and aluminum-oil Nano fluid at the same volume concentration, the temperature increased by 13.64% and 10.61%, respectively, in comparison to the oil without nanoparticles.

(Yohannis, 2022) a technique for parabolic trough baking injera using solar heat using Nano fluid as the heat transmission medium has been investigated. With an average family size of five people consuming three injera per day, the total amount of energy needed for a single baking session is 17,417.16kJ and thermal efficiency was 49.02%. This translates to a daily requirement of 15 injera, which equates to a three-day baking period requiring 45 injera.

(Alemu, 2020) an experiment has been conducted to see if the performance of a parabolic trough solar-powered injera baking oven improved by combining 7 grams of (CuO) nanoparticle with 10 liters of engine oil. Copper oxide Nano-fluid (CuO) with five different concentrations of nanoparticles in the range of 0.2, 0.4, 0.6, 0.8, and 1.0 grams was created in order to assess the temperature-dependent thermal conductivity. Discovered that at all concentrations of Copper oxide Nano fluid, the thermal conductivity increased by 35% overall, and the working heat transfer oil in the storage and absorber was discovered to be between 211 and 222°C.

(Hosseinzadeh et al., 2021) examined the overall energy and exergy efficiency of a parabolic dish collector-based Nano fluid indirect solar cooker. The volumetric flow rate of MWCNT-oil nano fluid, which varies from 250 to 550 milliliters per minute, and the mass fraction of the nanoparticles in the fluid, which ranges from 0 to 0.5 weight percent, were both investigated. The energy and exercise performance of the solar collector was found to be enhanced by raising the volumetric flow rate of the MWCNT-oil nano fluid from 250 ml/min to 550 ml/min. Whereas the solar collector achieves its highest energy and exergy efficiencies overall, the indirect solar cooker reaches its maximum energy and exergy outputs in the system with a volumetric flow rate of 250 ml/min, where the cooking unit's output thermal power and output thermal exergy rate are, respectively, 145.66 W and 14.71 W. The time required to boil two liters of water is lowered by roughly twenty-three minutes (31.51%) when MWCNT-oil nano fluid with 0.5 weight percent is substituted for thermal oil.

2.7 Working Fluid

The thermal energy supplied by the solar collector is transferred to the thermal energy storage system using a heat transfer fluid (Suman et al., 2015). Water, molten salt, and air are the typical operating fluids for these kinds of systems(Srilakshmi et al., 2015).

➢ Viscosity, ➢ Price, ➢ Toxicity, ➢ Environmental Impact, ➢ density,	➢ specific heat, ➢ thermal conductivity, ➢ compatibility, and ➢ Corrosiveness, and ➢ Stability

2.8 Thermal Insulation

A substance with very low thermal conductivity, or a mixture of materials with this property, is called thermal insulation. Thermal insulators provide many benefits, some of which include energy saving, process control, worker safety, and fire protection. Consider the following desired characteristics while selecting insulating materials (Deshmukh et al., 2017).

- ➢ low thermal conductivity,
- ➢ Non-corrosive,
- ➢ water absorption
- ➢ non-toxic
- ➢ non-flammable, and

Table 2. 2: Some proposed insulating materials' thermal characteristics (Rathan et al., 2021)

Material	**Thermal conductivity(W/mK)**	**Density (kg/m3)**
Ceramic tiles	1.3	880
Cork tiles	0.036-0.38	100-120
Glass Wool (Fiber Glass)	0.04-0.033	10-100
Mineral wool	0.35	70

2.9 Literature Summary and Identified gaps

2.9.1 Literature summary

Table 2. 3: Summary of some studies

Author(s)	Types of study	Types of collectors	Capacity detail			Working fluid	Main finding
			Number of collectors	Number of meals /day	Scale		
(Asfafaw et al., 2019) Injera baking	Experimental	P/Dish	1		Household	Water	
(Seid, 2021) Bread baking	Experimental	PTC	1		Household	Shell Thermal Oil B	η_{th} = 55.2% η_{en} = 31.1 T = 465.25K
(Kanyowa et al., 2021) cooking	Experimental	Scheffler dish	28	6000	Institutional		η_{th} = 70–80% η_{ov} = 25%
(YOHANES, 2020) Ijera baking	Experiential	Parabolic dish	1		Household	Oil	T_f =164 to 254 °C η_{rth} = 51.44% T_{panT} = 179.5°C
(Yohannis, 2022) Injera baking		PTC	1	15	Household	Nano fluid	η_{th} = 49.02%

(Alemu, 2020) Injera baking	Experiential	PTC	1		Household	(CuO) nano fluid	T_f = 211°C Tab = 222°C
(Hosseinzadeh et al., 2021) cooking	experimental	Parabolic dish	1		Household	MWCNT-oil nano fluid	P_{oth}= 145.66 W $P_{o,thex}$=14.71 W
(Jemal et al., 2022) Injera baking		PTC	1				collector efficiency at 0.3% (**η**)
						copper-oil	60%
						aluminum-oil nano fluid	56%
							Amount of steam produced
(Ktistis et al., 2021) Steam production		288 m^2 of PTC			Institutional	Steam	940L/day
(Muthu & Raman, 2006) Cooking		Parabolic dish	84	20,000	Institutional	steam	3500 kg/day
			106	30,000			4000 kg/day

2.9.2 Identified Research Gaps

The literature evaluation indicates that solar injera baking is a practical injera baking method because it has no health risks, is easily accessible, and reduces pollution. All of the studied literature regarding solar Injera baking was intended for small-scale or domestic applications by using parabolic troughs and parabolic dish collectors. Particularly, there hasn't been any institutional Injera baking using solar energy.

A high temperature (180–220°C) is needed for the injera baking procedure (Asfafaw et al., 2014). Due to this reason, a high-performance solar collector is required to offer high temperatures with good efficiency. In spite of the fact that central receiver solar collectors are less expensive for large-scale use and concentrate a lot of light onto a single receiver, which raises temperatures, no research has been done on the use of Power Tower solar cooking in both homes and institutions. In addition, evaluations based on the second law of thermodynamics, such as energy balance and exergy analysis, were not well covered in the literature. Since the Mitad is not typically heated directly by solar-powered Injera baking equipment, as observed from the literatures it took approximately around an hour to heat the fluid to the ideal temperature and an average of 30 minutes to attain the ideal baking surface temperature. Additionally, its heating time after one lap was on average 3 minutes, and its retention duration was 3 minutes.

Additionally, practically all of the injera baking systems tested in the research under review had thermal efficiencies below 60%. Energy inefficiency is primarily related to the time needed to heat up to the predetermined temperature to bake injera. In general, this study investigates solar injera baking by using a solar power tower for large-scale injera baking applications.

CHAPTER THREE

MATERIALS AND METHODS

3.1 Materials

Based on their availability, effectiveness in performing the desired functions, and overall suitability for the purpose of the thesis research, a careful selection of materials was made for the design and analysis. Some of the key components include

Table 3. 1: Material selection

Components	Material	Advantages
Tower and storage container walls	Stainless steel	High corrosion, fire and heat resistance, and high strength properties
Plate to support the mitad	Stainless steel	High corrosion, fire and heat resistance, and high strength properties
Insulator	Glass wool	Low thermal conductivity, less density, affordable price, and it is easy to install
Receiver	Copper tube	High thermal conductivity
Mitad leg and heliostat frame	RHS	Simplicity, low cost, and capacity to withstand a substantial amount of weight and pressure
Heliostat	Aluminum mirror	Is highly recyclable and reusable, reflects light more effectively

3.2 Methodology

This study is conducted in order to develop a productive and effective solar injera baking technology.

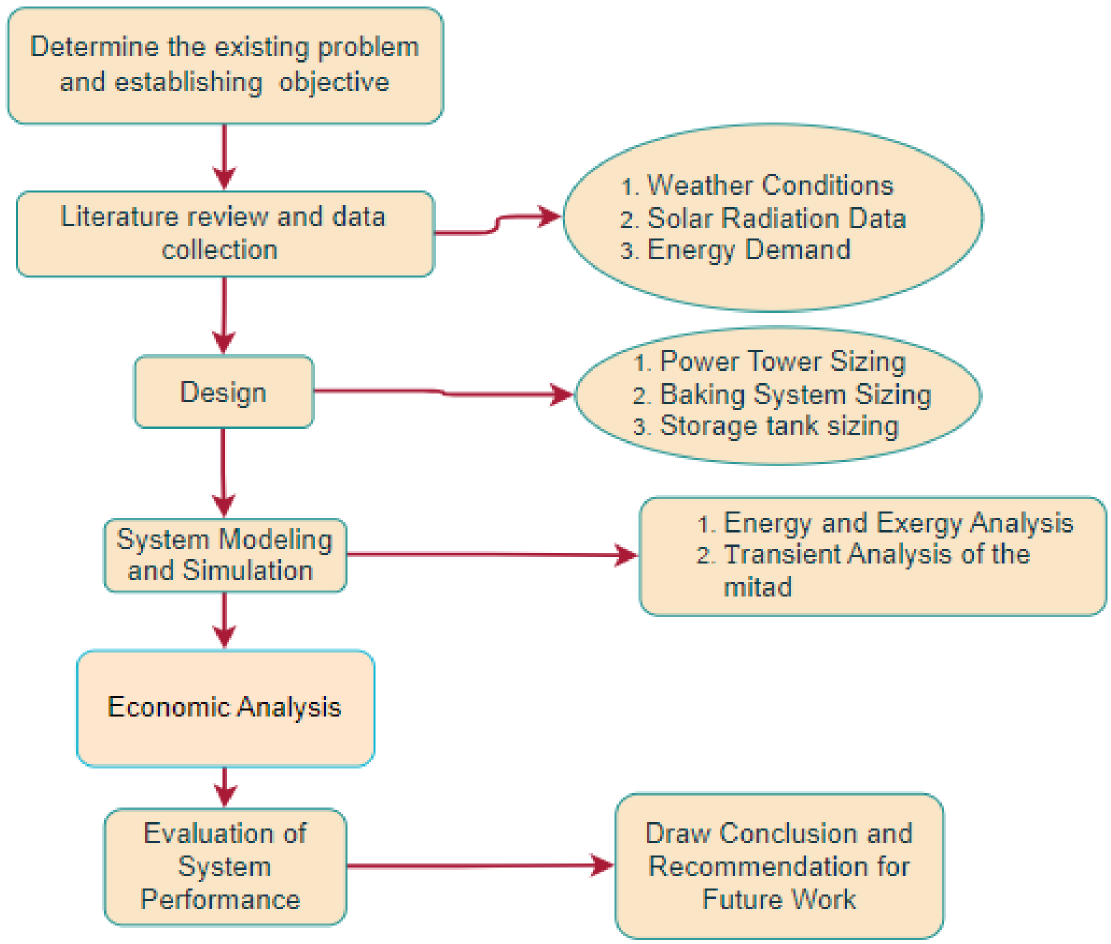

Figure 3. 1: Flow-chart for the methodological approach and progressive

3.2.1 Literature Survey

A literature survey was conducted to gather and review relevant materials on various topics including the basics of solar energy, solar radiation collectors and absorbers, types of solar cookers, injera baking methods, heat transfer fluids, insulation materials, and their selection. The literature survey involved gathering information from diverse sources, including books, journals, electronic media, and catalogs. This comprehensive approach ensured that a wide range of perspectives and findings were included, contributing to a strong scientific foundation for the thesis work.

3.2.2 Data Collection

The study began with an evaluating the daily demand for injera based on an average number of consumers and determining the necessary energy generation to produce the required quantity of injera. The objective is to identify the optimal design that can meet the demand for injera effectively. Data such as the daily demand for injera and other essential information necessary for the study were collected through primary data acquisition methods. The researcher conducted surveys and interviews to gather this information directly from the relevant sources. Furthermore, additional data was collected from the Ethiopian Meteorological Agency and the National Solar Radiation Database (NSRDB) specifically including information on Senkale sun radiation, ambient temperature, and wind speed. Moreover, various online sources such as books, website documents, and local and international journal articles were consulted to gather relevant data for the study.

3.2.3 Modeling and Simulation

The thesis work involved designing a power tower system and a baking system for mass Injera baking. Physical model of component of the system were modeled by CATIA V5 software. To evaluate the performance of the power tower system, Solar Pilot and Sol trace software were utilized for simulating and determining the amount of solar power reaching the system and meeting the energy requirements for indoor cooking. To evaluate the economic analysis of the project the System Advisor Model (SAM software) and Solar Pilot were utilized.

For the transient baking system analysis, Python software was employed. Additionally, Excel was utilized for estimation of solar radiation and visually presenting tabular data in graphical formats, enhancing the understanding and interpretation of the data.

3.2.4 Results and Discussion

The solar power tower and injera baking system are simulated to assess design, performance, and feasibility for mass production of injera. Sol Trace software analyzes receiver efficiency, optical efficiency, and receiver outlet temperature for optimal baking temperature. Python code examines initial heating time, baking surface temperature profiles, idle processes, and mitad temperature variation with thickness. In addition to this the discussion involves analysis of collected useful energy, exergy, heat loss, and thermal efficiency to comprehensively evaluate the system's effectiveness.

3.2.5 Conclusion and Recommendation

The simulation results are thoroughly discussed and based on these findings, appropriate recommendations and conclusions are presented. The discussion provides a comprehensive analysis of the simulation results, and the conclusions and recommendations are carefully addressed, serving as a valuable starting point for future practical work in the field.

3.3 Conceptual Layout of the System

The system is composed of two main subsystems, namely the Solar Power Tower System and the Injera Baking System. In the Solar Power Tower System, solar energy is harnessed by reflecting it onto a receiver, where it is converted into thermal energy. To transfer this thermal energy to the baking pan, a Heat Transfer Fluid (HTF) is employed. The HTF carries the energy from the receiver to a storage tank and then to the baking pan. To ensure the system's safety, a pressure release valve is utilized to release excess steam if the pressure becomes too high. The steam or hot water generated at the bottom of the baking pan is then returned to a cold fluid storage tank, where it cools down by mixing with the water in the tank before being pumped again.

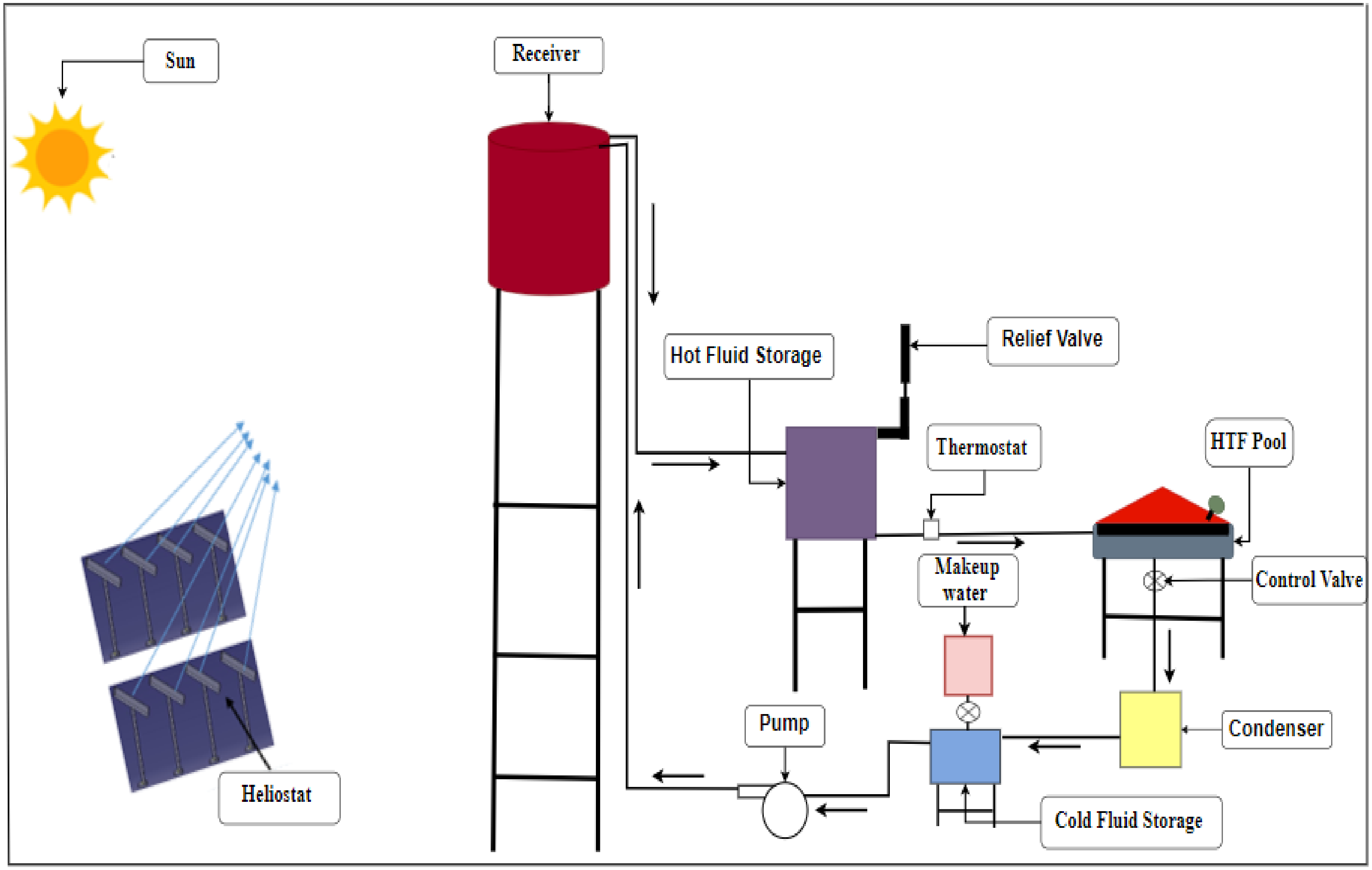

Figure 3. 2: Conceptual layout

CHAPTER FOUR

SOLAR POTENTIAL ESTIMATION AND THERMO-PHYSICAL PROPERTIES OF INJERA

An estimation of the incoming solar radiation is necessary to forecast the solar system's energy output (D. Murray, 2012).

4.1 Sun Earth Angle

Solar Time: At solar noon, when the sun crosses the observer's meridian, it is the apparent angular movement of the sun across the sky (Duffie & Beckman, 2013).

$$Solar\ time - Standard\ time = 4(L_{st} - L_{loc}) + E \tag{4.1}$$

Where, L_{st} - is the standard meridian for the local time zone; L_{loc} -is the longitude of the location. The parameter E is the equation of time (min) and is given by (Duffie & Beckman, 2013):

$$E = 229.2(0.000075 + 0.001868 \cos B - 0.032077 \sin B - 0.014615 \cos 2B - 0.04089 \sin 2B). \tag{4.2}$$

$$B = (n - 1)\frac{360}{365} \tag{4.3}$$

Where n is the day of the year

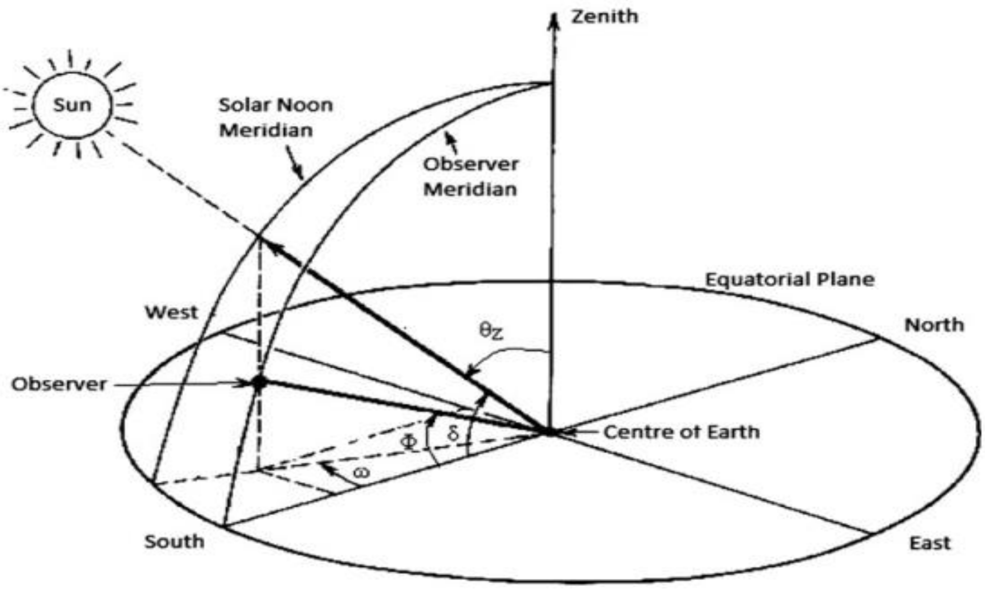

Figure 4. 1: View of different Sun–Earth angles (Shyam & Tiwari, 2018)

Latitude **(ϕ):** Latitude is defined as the angle produced between the radial line that connects an observer's location to the center of the Earth and its projection on the equatorial plane (90 ^{o}– ≤ **ϕ** ≤ 90^{o}). When observing from the north, latitude is positive, but when observing from the south, it is negative.

Declination (δ): is the sun's angular position with respect to the equator's plane during solar noon, north positive−23.45° ≤ δ ≤ 23.45° (Duffie & Beckman, 2013).

$$\delta = 23.45\sin\left[\frac{360}{365}(284+\mathrm{n})\right] \tag{4.4}$$

Where: n is day of the year.

Hour angle (ω): is the angle at which the Sun deviates from the local meridian as a result of the Earth's revolution about its own axis.

$$\omega = (\mathrm{ST}-12)\ \mathrm{x}\ 15^{0} \tag{4.5}$$

Where: ST is the local solar time

The total hour angle from sunrise to sunset is (2$\boldsymbol{\omega}_s$).

Table 4. 1 The northern hemisphere's hour angle value with respect to the time of day (Shyam & Tiwari, 2018).

Time of the day (h)	6	7	8	9	10	11	12
Hour angle (°)	-90	-75	-60	-45	-30	-15	0
Time of the day (h)	12	13	14	15	16	17	18
Hour angle (°)	0	+15	+30	+45	+60	+75	+90

Zenith ($\boldsymbol{\theta_z}$): is angle between a line perpendicular to a horizontal plane and the sun's rays

Slope (β): This is the angle that separates the flat surface that is being studied from the horizontal surface. For slopes that face south, its numerical value is viewed as positive, while for slopes that faces north, it is regarded as negative. **0**° ≤ β ≤ 180°**.** (β > 90◦ indicates that there is a downward-facing component on the surface), (Duffie & Beckman, 2013).

Altitude or solar altitude angle (α): is the angle formed by a horizontal plane and the Sun's rays α = 90^{0}- θ_z.

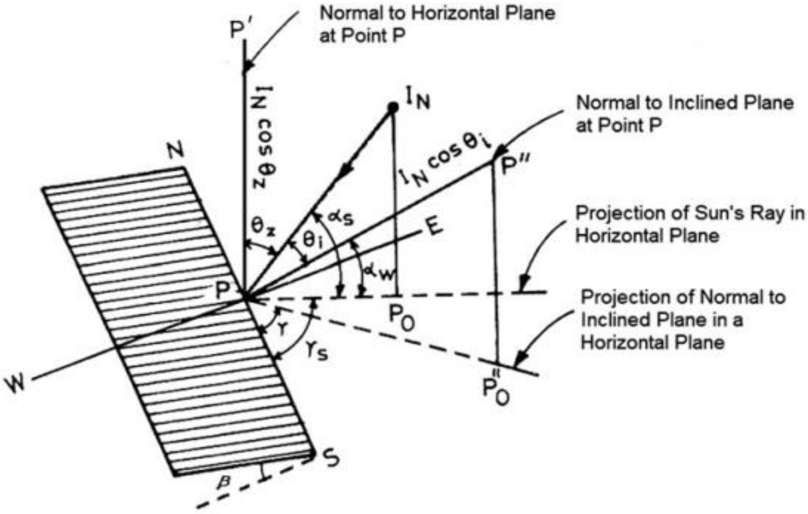

Figure 4. 2: Sun–Earth angles on an inclined surface (Shyam & Tiwari, 2018)

Surface azimuth angle (γ): The displacement of the normal to surface projection on a horizontal plane with zero due south, east negative, and west positive from the local meridian $-180^{\circ} \leq \gamma \leq 180^{\circ}$ (Duffie & Beckman, 2013).

Solar altitude angle (α_s): The complement of the zenith angle, which is the angle formed by the horizontal and the line leading to the sun.

$$\sin\alpha_s = \sin\phi\sin\delta + \cos\phi\cos\delta\sin\omega \tag{4.6}$$

Solar azimuth angle (γ_s): the angle at which the beam radiation projection on the horizontal plane is moved away from the south. east of south, displacements are negative and positive, respectively, west of south (Duffie & Beckman, 2013).

$$\gamma = \text{sgn}\left((\omega)\middle|\cos^{-1}\left(\frac{\sin\alpha\sin\phi - \sin\delta}{\cos\alpha\cos\phi}\right)\right) \tag{4.7}$$

Angle of incidence (θ): tan angle formed by a surface's beam radiation and its normal. Incidence and zenith angles for a horizontal plane are equal (Duffie & Beckman, 2013).

$$\text{Cos}\theta = (\cos\phi\cos\beta + \sin\phi\sin\beta\cos\gamma)\cos\delta\cos\omega + \sin\delta(\sin\phi\cos\beta - \cos\phi\sin\beta\cos\gamma) + \cos\delta\sin\beta\sin\gamma\sin\omega \tag{4.8}$$

Table 4. 2: Suggested Mean Days for Each Month and n-Values by Months (Duffie & Beckman, 2013).

Month	n for ith Day of Month	For Average Day of Month		
		Date	n	δ
January	i	17	17	−20.9
February	31 + i	16	47	−13.0
March	59 + i	16	75	−2.4
April	90 + i	15	105	9.4
May	120 + i	15	135	18.8
June	151 + i	11	162	23.1
July	181 + i	17	198	21.2
August	212 + i	16	228	13.5
September	243 + i	15	258	2.2
October	273 + i	15	288	−9.6
November	304 + i	14	318	−18.9
December	334 + i	10	344	−23.0

4.1.1 Senkale sun shines hours per day meteorological data

Eight years' average sun hour data of senkale were taken to evaluate the solar radiation data.

Table 4. 3: Average sun hour data of senkale

Months	Jan	Feb	Mar	Apr	May	Jun	Jul	Aug	Sep	Oct	Nov	Dec
Ave sun shine hours/day	9.1	8.95	7.81	6.69	6.48	5.3	3.25	3.4	5	8	8.6	9

4.2 Extraterrestrial Solar Radiation

The solar constant is the quantity of solar energy that is received on a unit area of a surface normal to the sun (perpendicular to the direction of radiation propagation) outside of the atmosphere in a unit of time at the mean distance between the earth and the sun, G_{sc} *(*Kalogirou, *2013).*

The extraterrestrial radiation (G_{on}) measured on the plane normal to the radiation on the N^{th} day of the year can be computed throughout the year using; (Kalogirou, 2013)

$$G_{on} = G_{sc}\left[1 + 0.033\cos\left(\frac{360N}{365}\right)\right] \quad (4.9)$$

Where G_{on} = Extraterrestrial radiation measured on the plane normal to the radiation on the **N**th day of the year (W/m^2).

G_{sc} = Solar constant (W/m$_2$), 1367 W/m^2 and N is the day of the year

The extraterrestrial solar radiation incident on a horizontal surface placed parallel to the ground outside of the atmosphere given by *(*Kalogirou, *2013)*

$$G_{oH} = G_{on}\cos\Theta_z$$

$$G_{oH} = G_{on} = G_{sc}\left[1 + 0.033\cos\left(\frac{360N}{365}\right)\right](\sin\phi\sin\boldsymbol{\delta} + \cos\phi\cos\boldsymbol{\delta}\cos\omega) \quad (4.10)$$

Monthly Average Daily Extraterrestrial Radiation on horizontal surface

The total radiation, $\mathbf{H_o}$**,** over a period from sunrise to sunset incident on an extraterrestrial horizontal surface during a day can be obtained by the integration of *(*Kalogirou, *2013)*

$$H_o = \frac{24*3600*G_{sc}}{\pi}\left[1 + 0.033\cos\left(\frac{360n}{365}\right)\right]\left(\frac{2\pi\omega_s}{360}\sin\phi\sin\delta + \cos\phi\cos\delta\cos\omega\right) \quad (4.11)$$

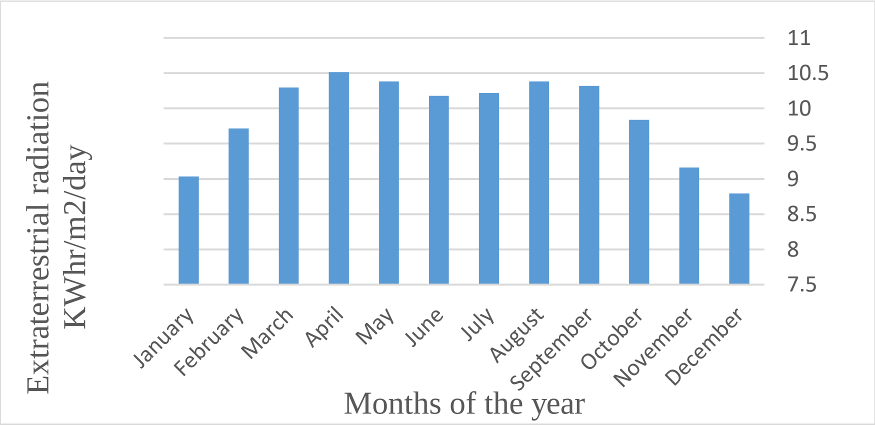

Figure 4. 3: Monthly average daily extraterrestrial radiation on horizontal surface of Senkale

4.3 Prediction of Monthly Average Daily Global, Diffuse and Beam Radiation on a Horizontal Surface

The Angstrom correlation can be used to calculate the monthly average daily global radiation on a horizontal surface from sunshine measurements, as (Duffie & Beckman, 2013).

$$\frac{H}{H_o} = a + b\frac{n}{N} \quad (4.12)$$

Where H is the monthly average daily global radiation, H_o is the monthly average daily extraterrestrial radiation,

n = Monthly average daily hours of bright sunshine

N = Monthly average of maximum possible daily hours of bright sunshine (i.e., day length of average day of month**)** and a and b are empirical coefficients

The regression coefficients a and b can be determined as follows (Shyam & Tiwari, 2018)

$$a_1 = -0.11 + 0.235\cos\phi + 0.32\left(\frac{n}{N}\right) \tag{4.13}$$

$$b_1 = 1.449 + 0.235\cos\phi + 0.694\left(\frac{n}{N}\right) \tag{4.14}$$

The association between the monthly average daily global radiation on a horizontal surface and the number of bright sunshine hours can be used to calculate the monthly average daily diffuse radiation on a horizontal surface (Shyam & Tiwari, 2018)

$$\frac{H_d}{H} = 0.931 - 0.814\left(\frac{n}{N}\right) \tag{4.15}$$

The calculation of monthly average daily beam radiation on a horizontal surface is as follows:

$$H_b = H - H_d$$

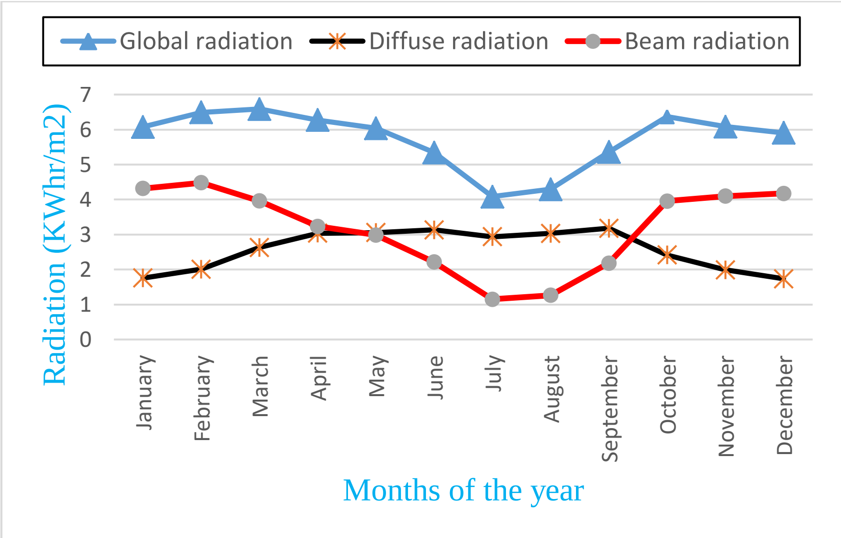

Figure 4. 4: Prediction of monthly average daily global, diffuse and beam radiation on a horizontal surface

4.3.1 Monthly average hourly global solar Radiation on horizontal surface

The monthly average daily global radiation can be used to calculate the monthly average hourly global radiation on a horizontal surface (Duffie & Beckman, 2013)

$$\frac{I}{H} = \frac{\pi}{24}(a + b\cos\omega)\left[\frac{\cos\omega - \cos\omega_s}{\sin\omega_s - \frac{\pi}{180}\omega_s\cos\omega_s}\right] \quad (4.16)$$

The coefficients a_1 and b_1 are given by

$$a_1 = 0.409 + 0.5016\sin(\omega_s - 60) \quad (4.17)$$

$$b_1 = 0.6609 - 0.4767\sin(\omega_s - 60) \quad (4.18)$$

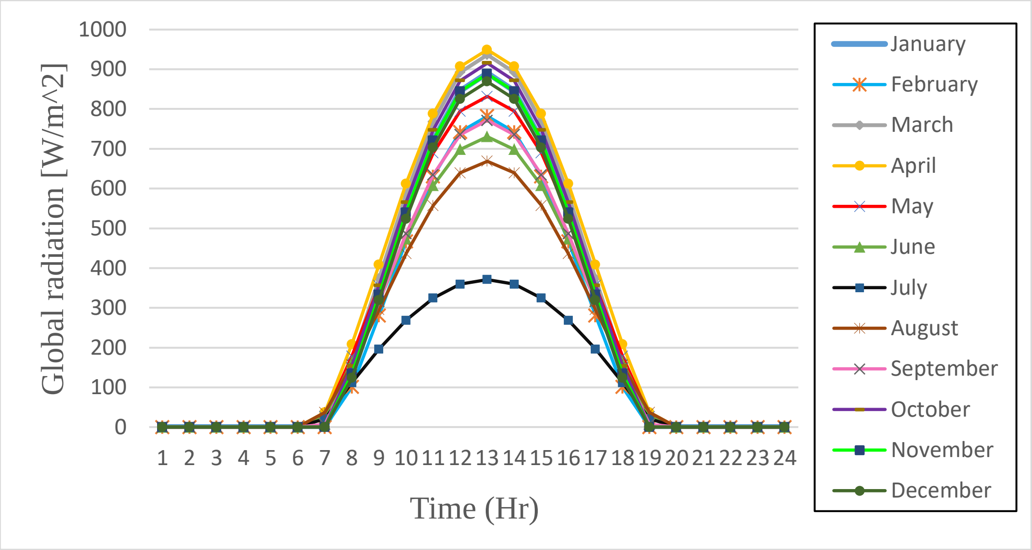

Figure 4. 5: Prediction of monthly average hourly global radiation on a horizontal surface

4.3.2 Estimation of Monthly average hourly diffuse and beam solar radiation on horizontal surface

The horizontal surface's monthly average daily diffuse radiation can be used to calculate the horizontal surface's monthly average hourly diffuse radiation.

(Duffie & Beckman, 2013).

$$\frac{I_d}{H_d} = \frac{\pi}{24}\left[\frac{\cos\omega - \cos\omega_s}{\sin\omega_s - \frac{\pi}{180}\omega_s\cos\omega_s}\right] \quad (4.19)$$

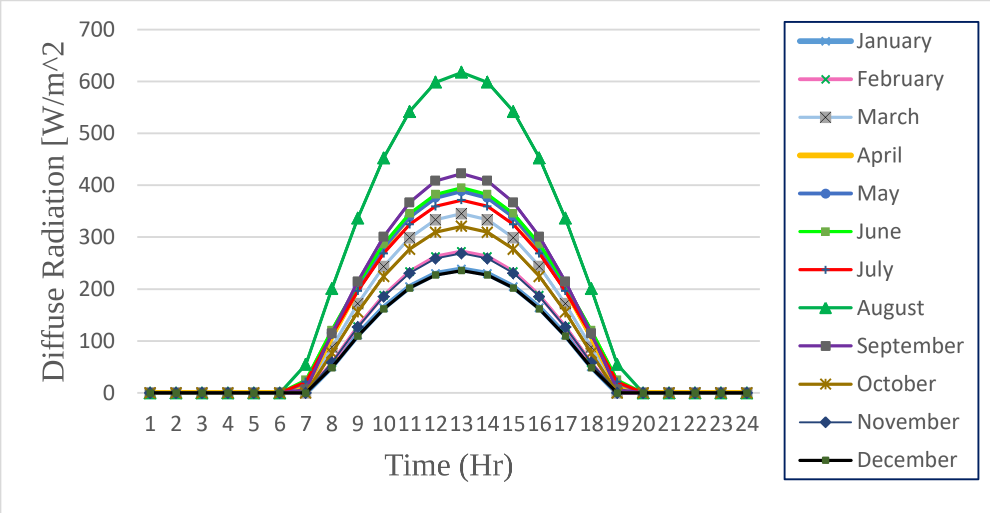

Figure 4. 6: Estimation of Monthly average hourly diffuse solar radiation on horizontal surface.

The monthly average hourly beam radiation on a horizontal surface is calculated as follow:

$$I_b = I_G - I_d$$

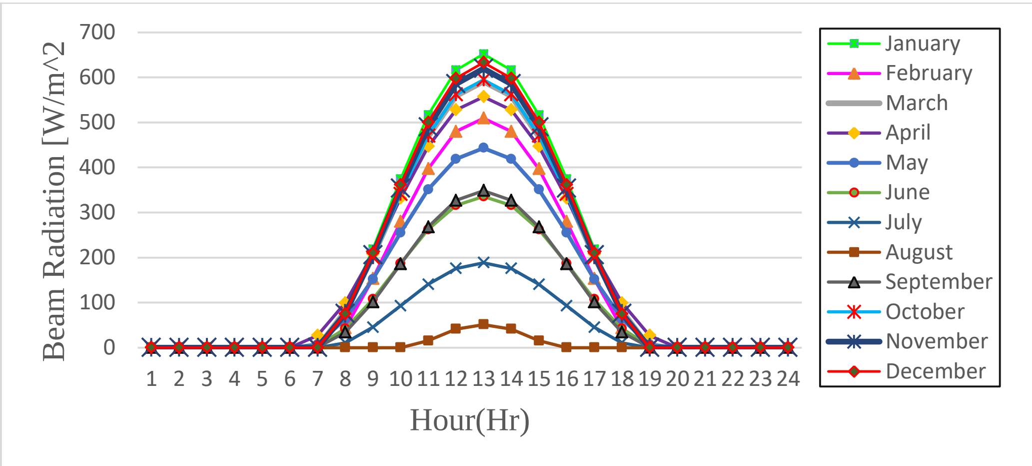

Figure 4. 7: Monthly average hourly beam radiation on a horizontal surface

4.4 Senkale Metrological Temperature Data

Senkale's climatic average from the last ten years was used to get the average monthly temperature. The collected monthly average temperature data for the year of (2013-2022) are shown in table.

Table 4. 4: Monthly average temperature annual climatic conditions of Senkale

Month	Jan	Feb	Mar	Apr	May	Jun	Jul	Aug	Sept	Oct	Nov	Dec
T(Max)	26.8	28.2	29.2	28.2	27.7	25.5	23.5	23.1	24.0	25.6	25.8	25.9
T(Ave)	18.1	19.7	20.7	20.2	19.9	18.6	17.6	17.2	17.4	17.7	17.6	17.5
T(Min)	9.3	11.2	12.2	12.2	12.1	11.7	12	11.3	10.7	9.7	9.3	9

4.4.1 Estimation of Hourly Variation of Atmospheric Temperature

There are mathematical models that can roughly predict the differences in temperature during the day based just on the daily high (maximum) and low (minimum) temperatures (Bellos et al., 2017)

$$T_{am} = T_{am,min} + \frac{DR}{2}\cos\left(2\pi \, x \frac{(t_h - t_{h,max})}{24}\right) \quad (4.20)$$

Where, $T_{am,min}$ = the average daily temperature of the day.

DR= daily range of the day's temperature

t_h = time of the day.

$t_{h,max}$ = A time for the occurrence of daily maximum temperatures

The ambient temperature normally reaches its maximum at 12:00, according to the results of Solar Pilot for Senkale camp which is a time for the occurrence of daily maximum temperatures.

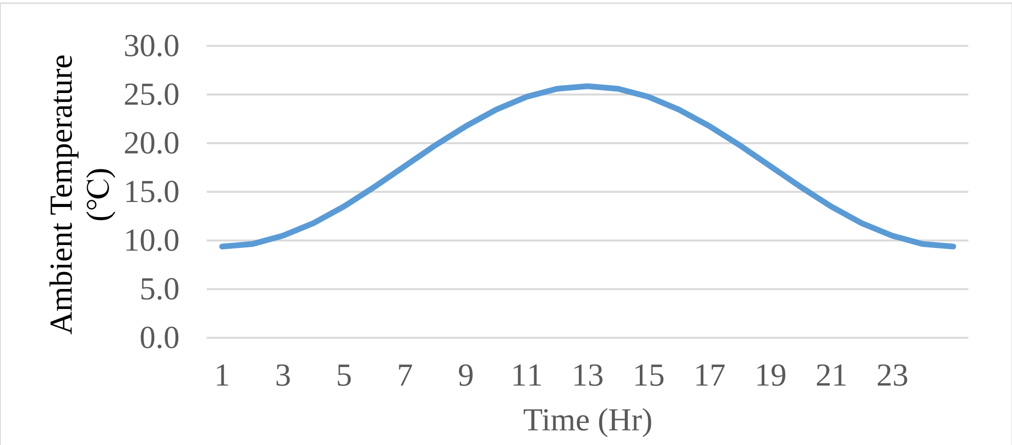

Figure 4. 8: Hourly Ambient Temperature pattern on November 14

4.5 Thermo-physical Properties of Injera

Foods' thermo-physical characteristics play a significant role in the modeling and optimization of heating and cooling systems. Typically, density (ρ), specific heat (Cp), and thermal conductivity (K) are the parameters utilized in a mathematical model of heat transport.

Temperature, material chemical composition (i.e., the amounts of water, ash, protein, carbs, and fat), and physical structure all affect a food's thermo-physical characteristics. Foods are composite materials, so the average value is clearly the pertinent information. This value is obviously a consequence of the component values (Jun & Irudayaraj, 2008).

Table 4. 5: Percentage composition of injera

Major components	Percentage by mass, (%)
Carbohydrate	33.9
Protein	4.2
Fiber	1.7
Ash	1.5
Fat	0.6
Moisture	58.1

4.5.1 Specific Heat Capacity

The ratio of heat gained or lost to temperature change for a unit mass is known as specific heat. The type of heat addition process—at constant pressure or constant volume—determines the specific heat capacity. Nevertheless, the specific heat at constant pressure is typically taken into consideration because pressure changes in heat transfer issues involving food products are typically quite tiny (Farinu, 2006). Mathematically, it can be represented as

$$C_p = \frac{Q}{M\Delta T} \qquad (4.21)$$

Where Q = heat lost or gained (J),

M = mass of product (kg),

ΔT = temperature change in the food material (K),

Cp = specific heat (J/kg.K).

Choi and Okos created a more comprehensive food specific heat prediction model. (Kaletunç, 2007)

$$C_p = \sum_{j=1}^{n} x_j C_{pj} = x_w c_{pw} + x_p c_p + x_f c_{pf} + x_c c_{pc} + x_a c_{pa} + x_{fib} c_{pfib} \qquad (4.22)$$

Where:

C_p = specific heat (J/kgK).

C_{pj}= specific heat of the components of the food (J/kgK), and

$\mathbf{x}_j$= percentage composition of the components.

The table provides empirical formulas to determine the specific heat of the primary elements in meals.

Table 4. 6: Calculating the specific heat of the main component in injera

Components	**Composition** (%) x_j	**Equations (*J/kgK*) $\mathbf{Cp_j\ x_j}$**
Carbohydrate	0.339	$0.339(1.5488+1.9625\times10^{-3}T - 9399\times10^{-6}T^2)$
Ash	0.015	$0.015(1.0926+1.8896\times10^{-3}T -3.6817\times10^{-6}T^2)$
Fiber	0.017	$0.017(1.8459+1.8306\times10^{-3}T - 4.6509\times10^{-6}T^2)$
Fat	0.006	$0.006(1.9842+1.4733\times10^{-3}T - 4.8008\times10^{-6}T^2)$
Protein	0.042	$0.042(2.0082+1.2089\times10^{-3}T - 1.3129\times10^{-6}T^2)$
Moisture	0.581	$0.581(4.1762 - 9.0864\times10^{-5}T^2+5.4731\times10^{-6}T^2)$

The specific heat as a function of temperature becomes:

$$C_p = \sum_{j=1}^{n} x_j C_{pj} = 3.0954 + 7.3158x10^{-4}T + 9.4806x10^{-7}T^2 \qquad (4.23)$$

At the average baking temperature, the specific heat of injera becomes 3095.96 j/kg.k.

4.5.2 Density

A material's density is determined by its mass to volume ratio. Density is a feature that is highly dependent on the mass fractions of the food's primary ingredients. It can be determined by (Jun & Irudayaraj, 2008)

$$\rho = \frac{1}{\sum_{i=1}^{n} x_{i/\rho_i}} \tag{4.24}$$

Where:

ρ = density of the product kg/ m^3,

ρ_i= density of each food composition kg/m^3, and

x_i= mass or weight fraction of each food composition.

The table below provides an empirical relationship for calculating the density of the main food ingredients as a function of temperature (Farinu, 2006).

Table 4. 7: Models for the Density of Food's Major Components (Farinu, 2006)

Components	**Equations**
Carbohydrate	ρ = 1.5991×103-0.31046 T
Ash	ρ = 2.4238×103-2.8063 T
Fiber	ρ =1.3115×103-0.36589 T
Fat	ρ = 9.2559×102-0.41757 T
Protein	ρ = 1.3299×103-0.51840 T
Water	ρ = 997.18 + 3.1439×10-3 T-3.7574×10-3 T2

After determining the densities of the key components at the average baking temperature using the relations shown in the above Table, the density of injera may be calculated.

Components	Composition (%) x_i	Density kg/m^3 ρ_i	$\frac{x_i}{\rho_i}$

Carbohydrate	0.339	1582.025	2.14×10^{-4}
Ash	0.015	2408.365	6.23×10^{-6}
Fiber	0.017	1291.376	1.32×10^{-5}
Fat	0.006	902.624	6.65×10^{-6}
Protein	0.042	1301.388	3.23×10^{-5}
Moisture	0.581	985.987	5.89×10^{-4}
$\sum_{i=1}^{n}\frac{x_i}{\rho_i}$ = **8.617×10^{-4}**			

At the typical average baking temperature which is 200℃, the density of injera becomes:

$$\frac{1}{\sum_{i=1}^{n}\frac{x_i}{\rho_i}} = 1160.5\,\frac{kg}{m^3}$$

4.5.3 Thermal conductivity

A food's thermal conductivity is the amount of heat that moves through it in a unit of thickness and area with a unit temperature differential every unit of time. For thermal conductivity, a more straightforward approximation is provided as

$$\mathrm{K} = \frac{\mathrm{Qx}}{\mathrm{A\Delta T}} \tag{4.25}$$

Where:

K = Thermal conductivity **(**W/m.K**)**

Q = Rate of heat input **(**W)

X = Material thickness parallel to heat flow **(**m)**,**

Δ*T* = Temperature change **(***ºC***),** and

A **=** Contact area normal to direction of heat flow **(**m^2)**.**

A number of physical models have been proposed to predict the thermal conductivity of food. Models that assume different components are stacked in layers either parallel to or perpendicular to the direction of heat flow are the most common (Farinu, 2006).

The series model is shown as:

$$\mathrm{K} = \frac{1}{\sum_{i=1}^{n}\frac{\varepsilon_i}{k_i}} \tag{4.26}$$

On the other hand, the parallel model is represented by:

$$K = \sum_{i=1}^{n} k_i \varepsilon_i \qquad (4.27)$$

Where:

ε_i= the volume fraction of i^{th} component phase (m 3)

k_i = the thermal conductivity of i^{th} phase (W/m.K)

k = thermal conductivity of the product (composite medium) (W/m.K).

From the mass fractions xi and intrinsic densities ρi, the volume fractions can be computed as

$$\varepsilon_i = \frac{x_i/\rho_i}{\sum_{i=1}^{n} \frac{x_i}{\rho_i}} \qquad (4.28)$$

Table 4. 8: Models of the main food ingredients' thermal conductivity

Components	Equations
Carbohydrate	$K = 0.20141+1.3874\times10^{-3}T - 4.3312\times10^{-6}T^2$
Ash	$K = 0.32962+1.4011\times10^{-3}T - 2.9069\times10^{-6}T^2$
Fiber	$K = 0.18331+1.2497\times10^{-3}T - 3.1683\times10^{-6}T^2$
Fat	$K = 0.18071+2.7604\times10^{-3}T - 1.7749\times10^{-6}T^2$
Protein	$K = 0.17881+1.1958\times10^{-3}T - 2.7178\times10^{-6}T^2$
Water	$K = 0.57109+1.7625\times10^{-3}T - 6.7036\times10^{-6}T^2$

Table 4. 9: Calculating the Major Components' Volume Fraction in Injera

Components	Composition (%), x_i	Density (*kg/m3*), ρi	$xi/\rho i$	$\varepsilon_i = \frac{xi/\rho i}{\sum_i^n xi/\rho i}$
Carbohydrate	0.339	1582.025	2.14×10^{-4}	0.248
Ash	0.015	2408.365	6.23×10^{-6}	0.00723
Fiber	0.017	1291.376	1.32×10^{-5}	0.015
Fat	0.006	902.624	6.65×10^{-6}	0.00772
Protein	0.042	1301.388	3.23×10^{-5}	0.03748
Moisture	0.581	985.987	5.89×10^{-4}	0.68353
$\sum$			$8.617x10^{-4}$	

Table 4. 10: The measurement of the main components' thermal conductivity for the parallel model

Components	ε_i	ε_i $\mathbf{k}_i$
Carbohydrate	0.24800	$0.0499+3.4408\times10^{-4}T- 1.0741\times10^{-6}T^2$
Ash	0.00723	$2.3828\times10\text{-}3+1.0129\times10^{-5}T - 2.1014\times10^{-8} T^2$
Fiber	0.01500	$2.7649\times10\text{-}3+1.8746\times10^{-5}T - 4.7525\times10^{-8} T^2$
Fat	0.00772	$1.3806\times10\text{-}3+2.1302\times10^{-6}T - 1.3697\times10^{-9} T^2$
Protein	0.03748	$6.7018\times10\text{-}3+4.4819\times10^{-5}T - 1.0186\times10^{-7} T^2$
Moisture	0.68353	$0.57109xw+1.7625\times10^{-3}T\,xw+6.7036\times10^{-6}\,T^2xw$

At the average baking temperature which is equal to 200℃, the thermal conductivity of the parallel model becomes $K_{parallel}$ =0.878 W/mk

Components	Composition (%) xi	εi	ki	$\frac{\varepsilon i}{ki}$
Carbohydrate	0.339	0.24800	0.38466	0.6447
Ash	0.015	0.00723	0.49789	0.0145
Fiber	0.017	0.01500	0.36346	0.0413
Fat	0.006	0.00772	0.29636	0.026
Protein	0.042	0.03748	0.35358	0.106
Moisture	0.581	0.68353	0.69775	0.9796
$\sum\frac{\varepsilon i}{ki}$ =1.8121*W/m.K*				

$$\text{Kseries} = \frac{1}{\sum_{i=1}^{n}\frac{\varepsilon i}{ki}} = 0.552\,\frac{w}{mk}$$

The literature states that any figure between the series and parallel models can be used to determine the food's thermal conductivity, i.e**. 0.552 <k< 0.878 W/m.K.**

Injera's thermal conductivity, which was utilized in the simulation for this design, is 0.6W/mK.

CHAPTER FIVE

ENERGY DEMAND AND PERFORMANCE ANALYSIS OF THE SYSTEM

5.1 Energy Demand of Injera Baking

The energy used for baking and the energy used to heat the pan together make up the entire amount of energy needed for the baking process. To calculate the energy required to bake injera, the beginning mass of the dough and the final mass of the injera after baking were thus determined.

Table5. 1: 1 Injera's and the baking pan's thermos-physical characteristics (Ambaw, 2015) (Yohannis, 2022) (YOHANES, 2020), (TSEGAYE, 2021) (Mesele Hayelom Hailu et al., 2017) (Jemal et al., 2022) (Bonsa, 2020).

Properties	Value
Specific heat capacity of Teff flour	1.625kJ/kg.K
Teff mass fraction in the dough	0.2732
Initial mass of batter	0.4kg
Thermal conductivity of water	0.68 W/m.K
Mass of Injera	(0.3-0.3455) kg
Moisture content of the dough(water mass fraction)	0.7268
Average clay diameter	(550 – 580) mm
Average clay thickness	20mm
Thermal conductivity of pan	0.391-0.5 W/m.K
Mass of pan	7kg
Bottom insulation thickness	30 to 35 mm
Specific heat of pan	0.9 kJ/kg.K

Hence, the amount of baking energy used is provided by (Mesele H Hailu et al., 2017)

$$Q_{baking} = E_{Usefull} = m_{batter} \text{ x } C_{p,batter} \text{ x } (T_{bt} - T_r) + h_{fg} \text{ x } m_w \qquad (5.1)$$

Where $m_w =$ mass of the evaporated water

$T_{bt} =$ Boiling temperature of water in Senkale ($T_{bt} = 92.62C$).

$T_r =$ The room temperature in the kitchen (18.41^0C)

$h_{fg} =$ The latent heat of vaporization of water (2260KJ/Kg)

$C_{pw} =$ Specific heat capacity of water (4.187 KJ/Kg. K)

The mass of evaporated water, based on the aforementioned assumptions, is given by

$$m_w = m_{batter} - m_{injera} \qquad (5.2)$$

Using above equation by substituting the parameters baking energy required for one Injera is 273KJ. The cooking time of one injera is estimated to be between two and three minutes (YOHANES, 2020). It is possible to compute the amount of power needed to bake injera as:

$$P = \frac{E_{req}}{t} \qquad (5.3)$$

Where: P- the power required for baking one Injera $\Delta t = 3 \times 60 = 180$second

$$P_{Utilized} = P = \frac{E_{Utilized}}{t_{baking}} = \frac{273KJ}{180sec} = 1.52kw$$

The quantity of heat needed to warm a backing medium or the energy needed to raise the pan's surface temperature from its starting point to the temperature needed to bake injera (180-220ºC) is given as (Mesele H Hailu et al., 2017).

$$Q_{heating\ up} = m_{pan} \text{ x } C_{p,pan} \text{ x } (T_h - T_i) \qquad (5.4)$$

Where $m_{pan} =$ mass of pan.

$C_{p,pan} =$ Specific heat of pan.

T_h= **B**aking temperature and T_i = Mitad initial temperature

Using equation 5.4, the amount of energy needed to warm up is 1144KJ. One method of calculating the heating up power is:

$$P_{\mathrm{heating}} = \frac{Q_{\mathrm{heating}}}{t_{\mathrm{heating}}} \tag{5.5}$$

Where t_{heating} is it takes about ten to fifteen minutes for the baking pan's surface to get up to the necessary temperature (YOHANES, 2020). The mitad warming up power is 1.47KW.

According to information from the Senkale Military Camp, two injera are consumed daily by an average of about 3000 people per round, meaning that 6000 injera are consumed daily. Total heat required for baking 6000 Injera is: $E_{\mathrm{Utilized}} = 1638\mathrm{MJ}$

Total heat required $Q_{total} = M_{\mathrm{number}} * Q_{\mathrm{heating\ up}} + 6000 * Q_{\mathrm{baking}}$

Where, M_{number} = number of mitad

In order to bake 8-hour number of mitad required (n) is equal to

$$M_{\mathrm{number}} = \frac{\mathrm{Total\ time}}{8\mathrm{h}} = \mathrm{n} = \frac{12\ \mathrm{min} + 6000\mathrm{x}3\mathrm{min} + (6000 - \mathrm{n})\mathrm{x}2\mathrm{min}}{8\mathrm{x}60\mathrm{min}} \cong 63$$

$$Q_{\mathrm{total}} = 63 * 1.144\mathrm{MJ} + 1638\mathrm{MJ} = 1710\mathrm{MJ}$$

The necessary total energy can be computed by taking into account the energy lost during baking and assuming a safety factor of 1.5 (YOHANES, 2020). As a result, 2565MJ of total energy are needed.

5.2 Heliostat Field Layout Design

(Wah & Kyaing, 2017) The majority of heliostat field layout designs employ a radial stagger pattern to minimize obstruction and permit unrestricted movement of each heliostat. Axial spacing, radial spacing, number of rows, number of heliostats, and characteristic diameter are among the factors that are displayed in the picture below, along with the steps involved in establishing a radial staggered heliostat field.

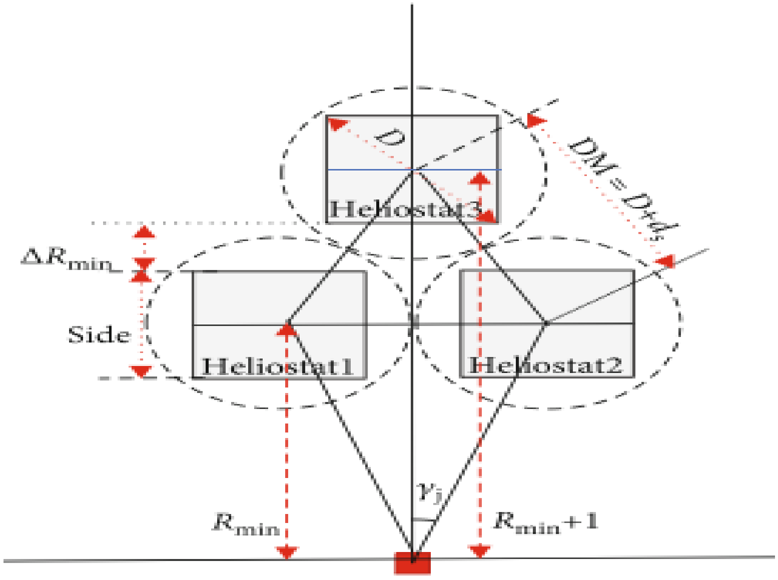

Figure 5. 1: Fundamental definitions in the heliostat field (Faye et al., 2021) (Saghafifar, 2016)

5.2.1 The Characteristic Diameter

$$DM = \left(\sqrt{1 + f^2} + d_s\right) . L_h \tag{5.7}$$

Where f is the ratio between the width and the length of the heliostat, ds is any additional space needed to separate nearby heliostats, and L_h is the length of the heliostat.

Assume heliostat width and height is 4mx4m and ds is equal to 1.5 and then DM ≅ 12m and length of heliostat is square root of heliostat area.

Table 5. 2: The inputs and parameters of the central tower receiver model

Parameter	**Value**	**Units**	**Reference**
Receiver height	9-11	m	(Ortega et al., 2008), (Collado & Guallar, 2013)
Receiver diameter	8-10	m	(Ortega et al., 2008), (Collado & Guallar, 2013)
Tube outer diameter	20-56	mm	(Albarbar & Arar, 2019)
Tube thickness	1-5	mm	(Albarbar & Arar, 2019)

5.2.2 The Radial and Azimuth Spacing

The minimum radial separation between the heliostat rows is determined as follows (Atif & Al-Sulaiman, 2017):

$$\Delta R_{min} = DM \text{ x } \cos 30^0 \qquad (5.8)$$

The number of heliostats in each row in the first zone can be used to calculate the radial distance (R_{min}) between the tower and the first row of heliostats (Saghafifar, 2016).

$$R_{min} = \text{Nhel1} \frac{DM}{2\pi} \qquad (5.9)$$

Where $Nhel_1$ represents how many heliostats there are in each row of the first zone which is assumed to be 20. The azimuth angular spacing for the first zone of the heliostat field can be found using (Saghafifar, 2016)

$$\Delta az_1 = 2\sin^{-1} \frac{DM}{2R_{min}} \qquad (5.10)$$

Where Δaz_1 denotes the first zone's azimuth angular spacing in rad

The i^{th} zone's azimuth angular separation can be calculated by (Saghafifar, 2016)

$$\Delta az_i = \frac{\Delta az1}{2^{i-1}} \qquad (5.11)$$

Where Δaz_i is the i^{th} zone's azimuth angular spacing in rad.

The radial distance between the tower and the i^{th} zone's first row is determined using (Saghafifar, 2016)

$$R_i = 2^{i-1} \frac{DM}{\Delta az_1} \qquad (5.12)$$

Where R_i is the i^{th} zone's first row's radius in meters.

5.2.3 Number of rows and heliostats

The i^{th} zone's number of rows is set by (Saghafifar, 2016)

$$Nrow_i = \frac{R_{i+1} - R_i}{\Delta R_{min}} \qquad (5.13)$$

Where $Nrow_i$ is the field's i^{th} zone's total number of heliostat rows depending on this

$Nrow_1 \cong 4, Nrow_2 = 8, Nrow_3 = 15, Nrow_4 = 30\ , Nrow_5 = 59, , Nrow_6 = 118$

For each row in the i^{th} zone, the number of heliostats is determined as (Saghafifar, 2016)

$$Nhel_i = \frac{2\pi}{\Delta az_i} \qquad (5.14)$$

Where $Nhel_i$ is the total number of heliostats in the i^{th} zone's each rows.

$Nhel_1 = 20, Nhel_2 = 40, Nhel_3 = 80, Nhel_4 = 160, Nhel_5 = 320, Nhel_6 = 640$

5.2.4 Tower Height

The tower should be constructed sufficiently high to reduce interference from nearby heliostats. (D. J. Murray, 2012). There is no upper limit to the maximum distance to tower height ratio (Pidaparthi, 2017). The two primary building materials for towers are free-standing steel or reinforced concrete. At tower heights under 120 meters (400 feet), freestanding steel towers are often more affordable. However, towers higher than 120 meters have shown to be more cost-effective when constructed using reinforced concrete. First ring radius is typically expressed as a function of receiver total height (h_T), which typically falls between $h_{T/2}$ and h_T (Faye et al., 2021)

5.3 Modeling of Optical Efficiency

The energy loss of the heliostat field is measured by the optical efficiency, η_{opt}. The optical efficiency is typically determined using (Atif & Al-Sulaiman, 2015)

$$\eta_{opt} = \eta_{at} \times \eta_{ref} \times \eta_{s\&b} \times \eta_{cos} \qquad (5.15)$$

Where $\eta_{s\&b}$ is for shadowing and blocking efficiency, η_{ref} for mirror reflectivity, η_{at} stands for atmospheric attenuation efficiency, and η_{cos} is for cosine efficiency.

The Atmospheric Attenuation Efficiency

While traveling from the mirror to the receiver, reflected light is affected by atmospheric attenuation. Losses due to atmospheric attenuation are determined by the distance between the receiver at the top of the tower and the heliostat. It's also impacted by certain weather conditions (Eddhibi et al., 2015)

$$\eta_{at} = \begin{Bmatrix} 0.99321 - 0.0001176 * \text{dist} + 1.97 \times 10^{-8} \text{ x dist}^2 & \text{dist} \le 1000\text{m} \\ \exp(-0.0001106 \text{ x dist}) & \text{dist} > 1000\text{m} \end{Bmatrix}$$

Mirror reflectivity

It is the degree of reflection; it is affected by deterioration and cleanliness.

The Shadowing and Blocking Efficiency

When one heliostat casts a shadow on another heliostat next to it, shadowing has taken place. As a result, the reflector is not exposed to all of the incident solar flux. When a heliostat in the front blocks the reflected flux from another heliostat, blocking losses happen (Wah & Kyaing, 2017)

The Cosine Efficiency

Energy losses resulting from cosine effects η_{cos} happen when the sun's rays strike the heliostats and are then less reflected to the receiver. The sun position and the specific heliostat's position in relation to the receiver both affect this effect. The angle of incidence $(\beta)_{inc}$ is connected to the scalar product of the solar vector τ_{solar} and the heliostat normal $n_{heliostat}$, that is (Ewert & Fuentes, 2015)

$$\eta_{cos} = \cos(\beta_{inc}) \qquad (5.16)$$

5.4 Modeling of the Central Receiver

5.4.1 System's equivalent capacity

In order to determine the amount of incident thermal energy on the central receiver (Q_{re}), the rated capacity (the required net output power) of the suggested SPT system and the thermal energy capacity of the TES subsystem are required. An average solar power plant without thermal storage is thought to be able to supply the required electricity for nine hours. The following equation determines the equivalent capacity of an SPT system with a (x)-hour thermal energy storage capacity: (Albarbar & Arar, 2019).

$$\text{Equivalent capacity} = \text{Rated capacity x } \frac{(9 + \text{x})}{9} \qquad (5.17)$$

5.4.2 Direct Normal Irradiance (DNI)

Because the amount of solar radiation in the environment changes over time, it is crucial to select a time when the device will perform at its peak level. This time is employed, which is selected to be midday, to establish the system's ideal design point. This is often when the DNI concentration of solar radiation is at its highest. This study made use of a histogram chart to pinpoint the DNI that was most frequent during the year. The DNI number that occurs most frequently, according to the histogram chart in Figure below, is 100 W/m2, which is then followed by 1000 and 900 W/m2. The solar radiation at start and end of the day, which is normally ignored when designing a solar system, is indicated by the 100 W/m2 (Albarbar & Arar, 2019).

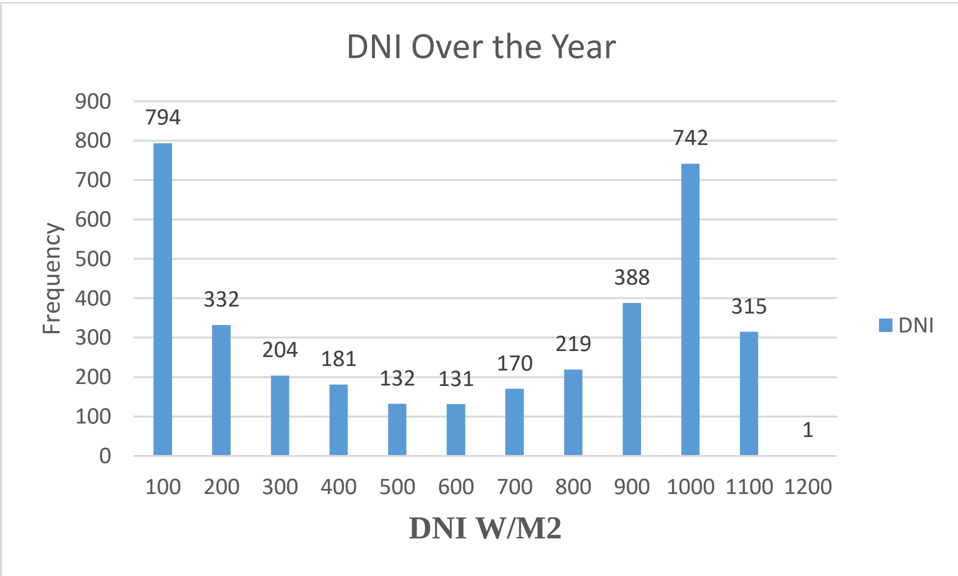

Figure 5. 2: A histogram chart of the Annual DNI for the area

5.4.3 Reflecting Area of the Heliostat

Evaluating the useful active reflecting area (A_h) of the heliostat field requires calculating the required thermal energy that the heliostat field must reflect to the central receiver. This can be determined by (Albarbar & Arar, 2019).

$$Q_h = \frac{\text{Equivalent capacity}}{\eta_{opt} \text{ x } \eta_{re} \text{ x} \eta_p} \tag{5.18}$$

$$Q_h = Q_{solar} = IA_h \tag{5.19}$$

In this case, I = Incoming radiation or direct normal irradiance (DNI)

A_h = Represents the heliostats' total reflecting area

In the given equation, Q_h represents the required thermal energy reflection of the heliostat field subsystem (measured in W), whereas DNI represents the hourly solar radiation per square meter, or Direct Normal Irradiance (DNI), for the region (measured in W/m2) (Albarbar & Arar, 2019). The mirror area (A_h), m^2 is then determined by:

$$A_h = \frac{Q_h}{DNI} \quad (5.20)$$

Heliostat area A_H and height L_H is given by

$A_H = \frac{A_{Mh}}{d_M}$ and $L_H = \sqrt{A_H}$, $A_{Mh} = L * W$

Where d_M = fraction of the heliostat′s mirror area which is equal 0.9583 (Collado, 2008).

$$A_{Mh} = \text{heliostat's mirror area}$$

Total number heliostat is equals to $\frac{A_h}{A_{MH}}$

5.4.4 Geometry of the receiver

5.4.4.1 Receiver outer geometry calculations

The outer receiver shape is important in assessing receiver efficiency since it can affect the receiver's total thermal heat losses. Receivers' exterior geometry is composed of their whole surface area (Are), height (H_{re}), and diameter (D_{re}) (Albarbar & Arar, 2019).

5.4.4.2 Height and Diameter of the Receiver

The receiver surface area (A_{re}) can be described by

$$A_{re} = \pi \text{ x } D_{re} \text{ x } H_{re} \quad (5.21)$$

Where: A_{re} = the total surface area (m2) of the receiver. The external cylindrical receiver's aspect ratio fall between 1.2 and 1.5 and it can be calculated using (Albarbar & Arar, 2019).

$$\text{Aspect Ratio} = \frac{H_{re}}{D_{re}} \quad (5.22)$$

Furthermore, the receiver area may be rewritten as;

$$A_{re} = \pi \text{ x } D_{re}^2 \text{ x AR}$$

5.4.4.3 Interior geometry of the receiver

Equation below is used to determine the inner diameter of tube (Albarbar & Arar, 2019).

$$d_{in} = d_{out} - t \tag{5.23}$$

Where d_{in} and d_{out} are receiver tube inner and outer diameter and t is thickness of receiver tube.

For this design outer diameter and thickness of 40mm and 2mm are used respectively.

5.5 Heat Transfer Fluid's Temperature

Heat exchange occurs whenever a fluid comes into contact with a solid body and there is a temperature differential between the two states. Energy was transferred from the heat transfer fluid to the baking pan using the next two techniques:

Heat is transferred by convection from the working fluid to the plate and by conduction from a pan-supporting plate to the baking pan.

Presumptions made during analysis;

- The pan surface temperature is considered to be 200°C for one-dimensional heat flow in the y-direction (average)
- There is negligible contact resistance between the pan and the plate
- The pan is well insulated from side and bottom.

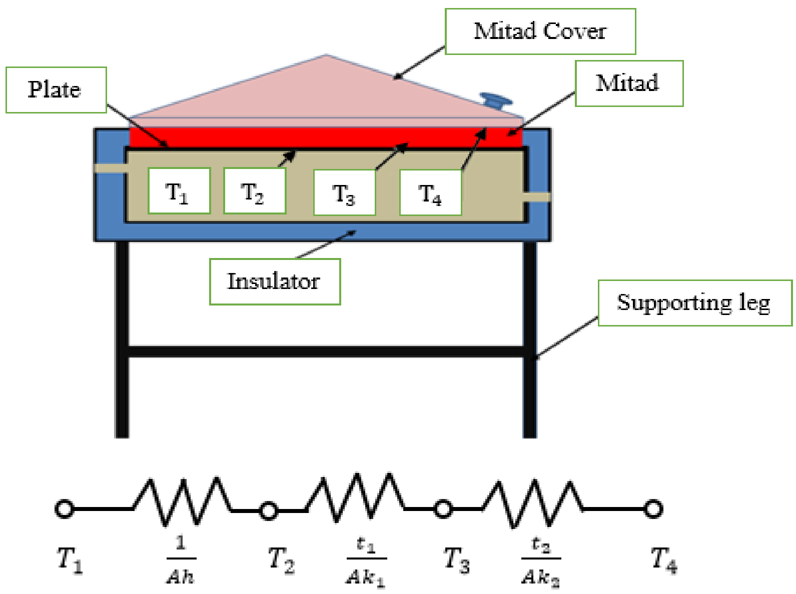

Figure 5. 3 Heat flow through mitad and its thermal resistance model

Where:

- T_1—Hot water temperature (°C)

- T_2: Surface temperature (°C) of the plate
- T_3- Lower surface temperature of a baking pan (°C)
- T_4: A baking pan's upper surface temperature of 200 °C

The rate of heat transmission from the working fluid to the surface of the baking pan can therefore also be expressed as follows (Shah & Sekulic, 2003)

$$Q = \frac{T_1 - T_4}{\frac{1}{hA} + \frac{t_1}{k_1 A} + \frac{t_2}{K_2 A}} \tag{5.30}$$

Where;

- t_1: Thickness of the plate =1mm
- t_2: Thickness of the baking pan = 20mm
- h: Convection Heat Transfer Coefficient of working fluid
- K_1: Thermal conductivity of supporting plate stainless steel 1%C, K1= 43w/m. K
- K_2: Cooking pan thermal conductivity
- A: Area of the pan,

Area of the pan is computed as $A = \frac{\pi D^2}{4} = 0.264 m^2$

Where D is the diameter of the pan = 0.58m

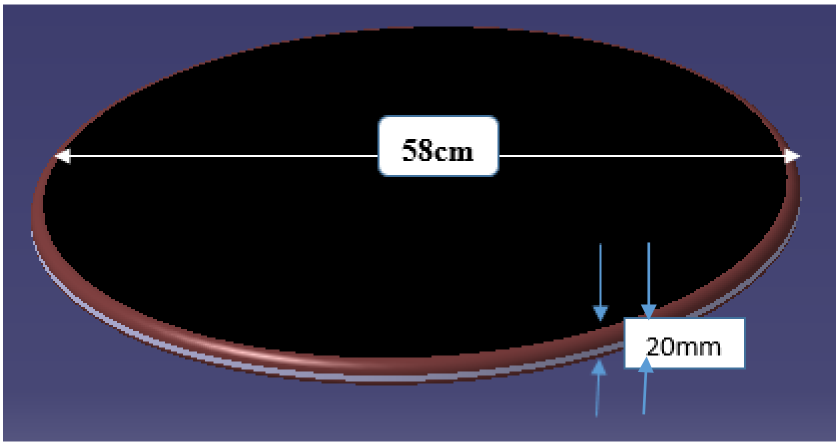

Figure 5. 4: Baking pan

Heat transfer through a pan by conduction

The maximum temperature that the heat transfer fluid can reach below the baking surface is determined using a steady-state heat transfer as this method focuses on the fluid's stable temperature after the heat transfer process reaches equilibrium. The pan's upper surface temperature (T_{pus}) is equivalent to the temperature needed to bake injera, which is T_{pus} = 200°C. Then utilizing conduction heat transfer, it is necessary to determine the lower surface temperature of the pan (T_{lsp}).

$$Q = \frac{K_p A(T_{lsp} - T_{pus})}{t_p} \tag{5.31}$$

Where $K_p =$ thermal conductivity of pan,

$t_p =$ thickness of pan,

$$T_{lsp} = Tpus + \frac{Qxtp}{Kp \times A} = 200°C + 1470 * \frac{0.02}{0.5 * 0.264} = 422.7°C$$

Heat transfer through a plate by conduction

The top surface temperature (T_{up}) of the plate (carbon steel) and the bottom surface temperature of the pan (T_{bsp}), as calculated in the previous formula, are equal. The plate's lower surface temperature T_{lp} can then be calculated using

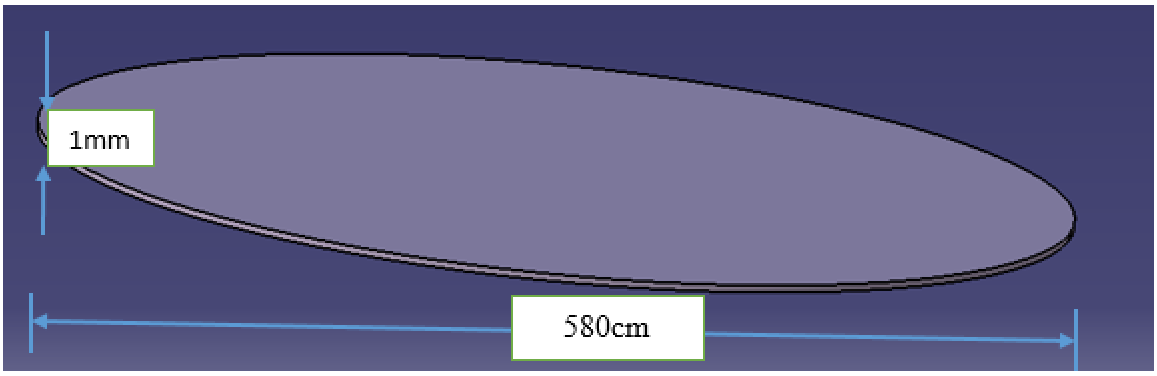

Figure 5. 5 Plate

$$Q = \frac{K_{plate} A(T_{lp} - T_{up})}{t_{plate}}$$

$$T_{lp} = T_{up} + \frac{Q \times t_{plate}}{K_{plate} A} = 422.7°C + 1470 * \left(\frac{0.001}{43 * 0.264}\right) = \mathbf{422.8}°C$$

5.5.1 The heat transfer fluid's convective heat transfer coefficient.

Based on information on the properties of heat transfer fluids, estimate the heat transfer coefficient at the film temperature (T_{fm}) by assuming that the temperature is (T_{fluid}) is 450°C

$$T_{fm} = \frac{T_{fluid} + T_{lp}}{2} = \frac{450 + 422.8}{2} = 436.5°C = 709.5K$$

The properties of working fluid or water taken at this film temperature from heat and mass transfer data hand book are:

- Density of fluid; $\rho = 0.31024 \frac{\mathrm{kg}}{\mathrm{m}^3}$
- Kinematics viscosity; $v = 79.288\mathrm{x}10^{-6} \frac{\mathrm{m}^2}{\mathrm{s}}$
- Dynamic viscosity; $\mu = 24.5804\mathrm{x}10^{-6} \frac{\mathrm{kg}}{\mathrm{m.s}}$
- Specific heat capacity; $c = 2.09112 \frac{\mathrm{KJ}}{\mathrm{Kg°C}}$
- Coefficient of thermal expansion $\beta = \frac{1}{\mathrm{T}} = \frac{0.141*10^{-2}}{\mathrm{K}}$
- Pradtle number; $\mathrm{Pr} = 1.0009 \frac{\mathrm{m}^2}{\mathrm{kg}}$
- Thermal diffusivity , $\alpha = {}^{\mathrm{k}}/_{\rho\mathrm{c}} = 0.5786\mathrm{x}10^{-4} \frac{\mathrm{m}^2}{\mathrm{s}}$

The Nusselt number for stationary circular discs with an isothermal temperature can be calculated as (Kobus & Wedekind, 1995):

Nusselt number,

$$\mathrm{Nu} = C_f \mathrm{Re}_{\mathrm{d}}^{\mathrm{n}} \mathrm{Pr}^{\frac{1}{3}} \qquad 9x10^2 \leq \mathrm{Re}_d \leq 3\mathrm{x}10^4 \tag{5.32}$$

$$C_f = 0.356, n = 0.6$$

$$\mathrm{Re}_d = \frac{\rho v d}{\mu} = 20496$$

Then, $\mathrm{Nu} = 138$

For a horizontal circular plate, the effective length of the heat transfer surface can be computed using the relationship.

$$\mathrm{L_c} = \frac{\mathrm{A_s}}{\mathrm{P}}$$

Where, A_s is the surface area and p is the perimeter. For a circular horizontal surface characteristic length is equal to one-fourth of its diameter D/4.

$$\mathrm{l} = \frac{\mathrm{A}}{\mathrm{P}} = \frac{\pi \mathrm{D}^2}{4\pi \mathrm{D}} = \frac{\mathrm{D}}{4} = 0.145\mathrm{m}$$

Hence, the average convective heat transfer coefficient can be determined using the formula

$$\mathrm{h} = \frac{\mathrm{Nuk_{htf}}}{\mathrm{L}} \cong 647.2 \frac{\mathrm{W}}{\mathrm{m}^2.\mathrm{k}}$$

Where $\mathrm{k_{htf}}$ =Thermal conductivity of water vapour is assumed to be constant (0.68 W/m·K).

The heat transfer to the plate is equivalent to the heat delivered by the working fluid and neglect the heat lose through the plate.

$$hA(T_{htf} - T_{lp}) = \frac{-K_pA(T_{pus} - T_{lp})}{t_p}$$

$$T_{htf} = 429.44°C$$

The heat transfer working fluid temperature is T_{htf} for the following iteration.

Then film temperature is given as,

$$T_f = \frac{T_{fluid} + T_{lp}}{2} = \frac{429.444 + 422.8}{2} = 426°C = 700K$$

- Density of fluid; $\rho = 0.3123 \frac{kg}{m^3}$
- Kinematics viscosity; $v = 78.128x10^{-6} \frac{m^2}{s}$
- Dynamic viscosity; $\mu = 24.4024x10^{-6} \frac{kg}{m.s}$
- Specific heat capacity; $c = 2.0877 \frac{KJ}{Kg°C}$
- Coefficient of thermal expansion $\beta = \frac{1}{T} = \frac{0.143*10^{-2}}{K}$
- Pradtle number; $Pr = 1.00048 \frac{m^2}{kg}$
- Thermal diffusivity , $\alpha = {}^{k}/_{\rho c} = 0.772x10^{-4} \frac{m^2}{s}$

At this film temperature, T_{fm} , the working fluid's properties are measured.

The Reynold number and the Nusselt number are now calculated by substituting the fluid properties values.

$$Re_d = \frac{\rho vd}{\mu} = 20784$$

Then, Nu = 139. Hence, the average convective heat transfer coefficient can be determined using the formula

$$h = \frac{Nuk_{htf}}{L} = 652 \frac{W}{m^2.k}$$

The heat transfer to the plate is equivalent to the heat delivered by the water and neglect the heat lose through the plate.

$$hA(T_{htf} - T_{lp}) = \frac{-K_pA(T_{pus} - T_{lp})}{t_p}$$

$$T_{fluid} \cong 429.395°C$$

The error between the consecutive iteration is given as:

$\text{Error} = \frac{T_f - T_i}{T_f} = \frac{429.444 - 429.395}{429.395} = 0.0113\%$

Thus, error between two consecutive iteration is negligible so the optimum temperature of the working fluid is $T_1 \cong 430°C$ then; we can get the receiver outlet temperature from thermal energy loss between bottoms of mitad's to receiver outlet which is equal to 430*1.25≅ 538°C

5.5.2 Total Mass Flow Rate

A constant mass flow rate, referred to as the total mass flow rate, is assumed to exist inside the main pipe that enters and exits the external receiver. Using the thermal energy absorbed by the heat transfer fluid, one can determine the mass flow rate of water entering the receiver at 88°C ($Q_{abs,}$) as (Albarbar & Arar, 2019).

$$Q_{abs} = \dot{m}_{total} \text{ x } Cp_w \text{ x } (T_{out,w} - T_{in,w}) \quad (5.44)$$

For the months of November 14, at solar noon we have thermal energy absorbed by the heat transfer fluid, **19.267MW.** From the graph we can get average mass flow rate of $15\frac{kg}{s}$

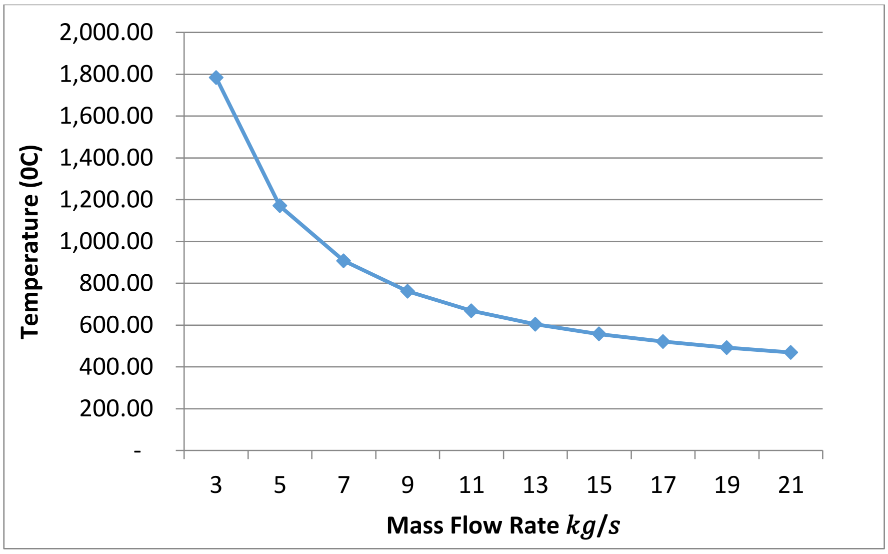

Figure 5. 6: Mass Flow Rate

5.5.3 The quantity of tubes and headers

Number of tubes per header, number of flow passes, and inner diameter of tubes are related to the total cross-sectional area of the fluid route (Asec) in (m2) (Albarbar & Arar, 2019).

$$A_{sec} = n_{tubes/header} * \frac{\pi}{4} d_{in}^2 x n_{flow\ path} \tag{5.24}$$

The Gema solar power plant's fluid is moving at a speed of around 2.8 m/s in the receiver tube (Albarbar & Arar, 2019).

$$A_{sec} = \frac{\dot{m}_{total}}{\rho_w x V_{tube}} \tag{5.25}$$

Then, by substituting above parameter $A_{sec} = 0.00536m^2$ and the number of tube per header is calculated from equation (5.24) $n_{tubes/header} \cong 5$

5.5.4 Length of a header

$$\text{Header length} = d_{out}\ x\ n_{tubes/header} + \left(1.2x10^{-3}x(n_{tubes/header} - 1)\right) \tag{5.26}$$

Where $(n_{tubes/header} - 1)$ is the number of gaps between tubes in a header, (d_{out}) is the outside diameter of the tube receiver (in m), and 1.2 $x10^{-3}$ is a rough weld thickness (in m) (Albarbar & Arar, 2019).

Then, header length $\cong 204.8mm$

The number of headers for a receiver can therefore be stated as a result.

$$n_{header/receiver} = \frac{\pi\ x\ D_{re}}{\text{header length}} \cong 138 \tag{5.27}$$

Then it is possible to determine the total number of receiver tubes ($n_{tubes\ total}$) as;

$$n_{tubes\ total} = n_{header/receiver}\ x\ n_{tubes/header} = 690$$

It is possible to calculate the mass flow rate inside a tube by

$$\dot{m}_{tube} = \frac{\dot{m}_{total}}{n_{flow\ path} x\ n_{tubes/header}} \ldots\ldots\ldots\ldots\ldots\ldots\ldots\ldots\ldots\ldots\ (4.34)$$

Check to see that the diameter and thickness of the selected tube match the calculated outside geometer of receiver the following formula is used (Albarbar & Arar, 2019).

$$\text{Max No. of tube per receiver} = \frac{\pi x D_{re}}{d_{out}} \tag{5.29}$$

The tube diameter and receiver diameter have an impact on the maximum number of tubes that can fit in each receiver. As a result, there are approximately 706 tubes per receiver at (Dre = 9 m and dout = 40 mm). However, the model result for the overall number of tubes is 692, which is fewer than the maximum.

5.6 Energy and exergy analysis for the central receiver

5.6.1 Thermal Energy of Receiver

The total incident thermal energy at the central receiver Q_{re} can be computed by

$$Q_{re} = Q_{in} = Q_{solar}\eta_{opt} \tag{5.33}$$

Where, η_{opt} is the optical efficiency and Q_{re} is the total incoming thermal energy on the receiver in W/m2.

Following is an expression for the total thermal energy absorbed by heat transfer fluid:

$$Q_{abs} = Q_{re} \text{ x } \eta_{re} \tag{5.34}$$

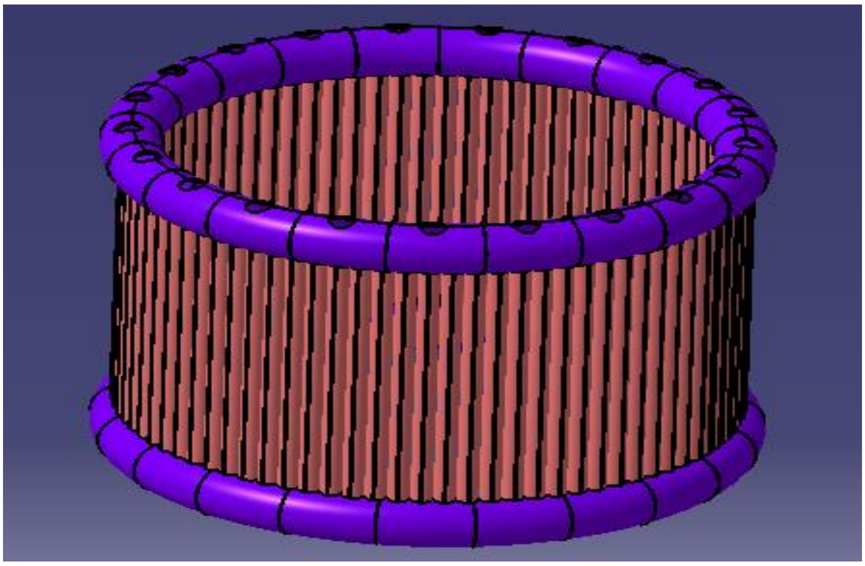

Figure 5. 7: Receiver

The general equation for the energy balance of the receiver's body can be described as follows:

$$Q_{re} = Q_{loss,total} + Q_{abs} \tag{5.35}$$

Where $Q_{loss,total}$ (W) represents all heat transfer losses, including convection, emissive, reflection, and conduction losses.

$$Q_{loss,total} = Q_{conv,air} + Q_{em} + Q_{ref} + Q_{cond} \tag{5.36}$$

The following figure, where r_{in} and r_{out} are the inner and outer radii of a tube (m), respectively, serves as an illustration of the energy balance model for a receiver tube.

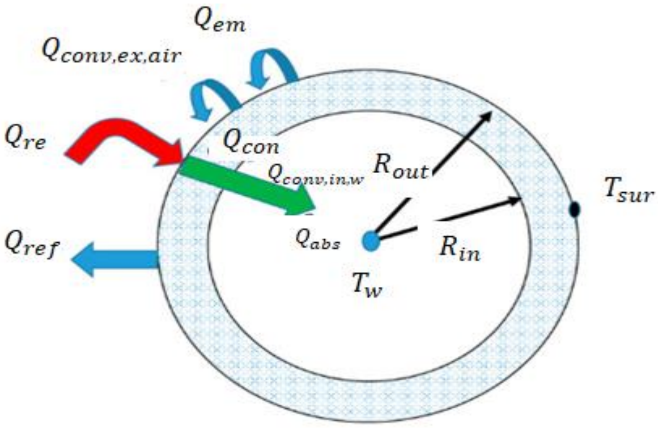

Figure 5. 8: Energy balance model for a receiver tube.

5.6.2 Surface Temperature of the Receiver

The receiver surface temperature is dependent on the incident solar energy and the temperature of the HTF passing through the tubes. The surface temperature of the receiver is taken to be constant.

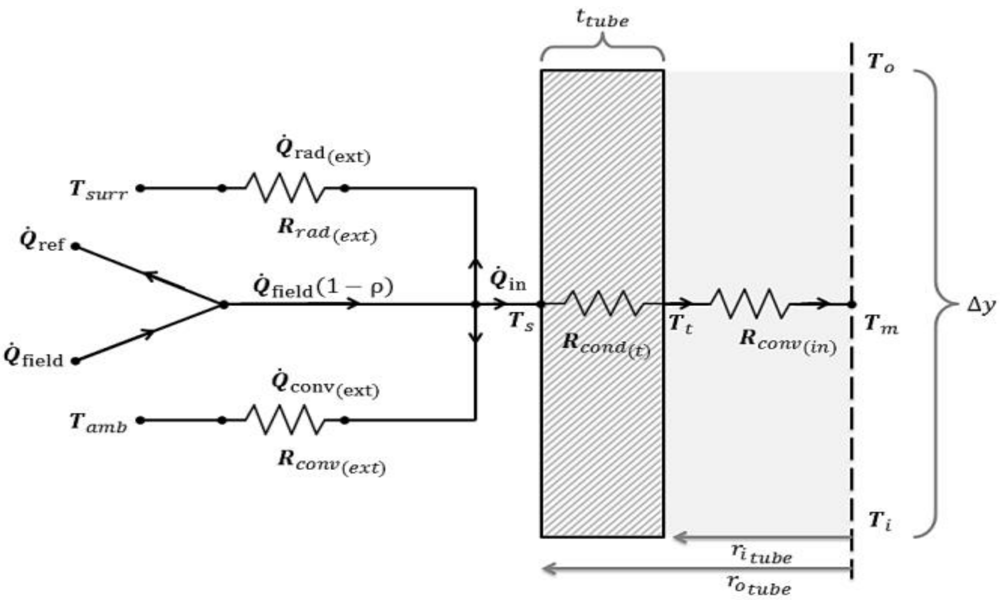

Figure 5. 9: Thermal resistance circuit diagram of a receiver tube (De Meyer et al., 2016).

$$Q_{field} - Q_{ref} = Q_{field}(1-\rho) = Q_{in} + Q_{conv} + Q_{rad} \tag{5.37}$$

Where, Q_{field} = receiver's incident flux. The receiver reflectivity (ρ) affects the reflected radiation (Q_{ref}) from the receiver. Accordingly, the energy transferred to the heat transfer fluid (Qin) is influenced by incident flux onto the receiver, reflected radiation, external thermal radiation loss (Q_rad), and external convective heat loss (Q_conv).

$$Q_{conv} = \frac{(T_s - T_{amb})}{R_{conv(ext)}} \tag{5.38}$$

$$Q_{rad(ext)} = \frac{(T_s - T_{surr})}{R_{rad(ext)}} \tag{5.39}$$

$$Q_{in} = \frac{(T_s - T_t)}{R_{cond}} = \frac{(T_t - T_m)}{R_{conv(in)}} = \frac{(T_s - T_m)}{R_{cond} + R_{conv(in)}} = \dot{m}C_p(T_o - T_i) \tag{5.40}$$

The following temperature indicators show the receiver surface temperature: (T_s), ambient temperature (T_{amb}), outside or sky temperature (T_{surr}), inner tube temperature (T_t), mean heat transfer fluid temperature (T_m), and temperatures of the heat transfer fluid intake (T_i) and outlet (T_o). (De Meyer et al., 2016).

$$R_{rad(ext)} = \frac{1}{h_{rad(ext)}A_s} \tag{5.41}$$

$$R_{con(ext)} = \frac{1}{h_{conv(ext)}A_s} \tag{5.42}$$

$$R_{cond} = \frac{L_t}{K_t A_t} \tag{5.43}$$

Regarding radiation and convection losses, the corresponding exposed surface area (As) is utilized, whereas the cross sectional area (A t) is used for heat conduction from the outer tube region to the inner tube area. Both the cross section length (Ls) and the tube thickness (t) are the same. The heat transfer coefficients (h) corresponding to the external convection resistance (R conv(ext)), interior convection resistance (R conv(in)), and external radiative resistance (R rad(ext)) are as follows:

$$R_{cond} = \frac{\ln\frac{r_{out}}{r_{in}}}{2 * \pi * H_{re} \,\mathrm{x}\, K_t} = 3.93 * 10^{-6}\,\frac{W}{°C}$$

Where $K_t$is the receiver tub's thermal conductivity which 388 W/m°C

Internal forced convection

$$R_{conv(in)} = \frac{1}{h_{conv(in)} \,\mathrm{x}\, A_{in}} \tag{5.45}$$

$$h_{conv(in)} = \frac{K_{htf} x Nu_{htf}}{D_i} \tag{5.46}$$

Where: K_{htf} = Thermal conductivity of water is assumed to be constant $(0.68\ W/m \cdot K)$.

Nu_{htf} = Internal forced convection

D_i = Receiver inner tube diameter

$$Q_{in,tube} = \frac{(T_s - T_{flm})}{R_{cond} + R_{conv(in)}} \tag{5.47}$$

However, energy transmitted to the receiver (Q_{in}) is given as $Q_{in} = 19.267MW$ and number of tube is equals to 692

$$T_{htf} = \left(\frac{T_{in,htf} + T_{out,htf}}{2}\right) = \frac{250 + 556}{2} \cong 403°C$$

Heat transfer by mixed convection occurs as the fluid flows through the receiver (Aicher & Martin, 1997). Let us assume that pure natural convection heat transfer correlations occur during downward flow and pure forced convection heat transfer correlations occur during upward flow.

The Nusselt number for pure natural convection heat transfer inside a vertical pipe is given as (Kang & Chung, 2010):

$$Nu_H = 0.65Ra^{0.25} \tag{5.48}$$

Assume the pipe's inner surface temperature to obtain the Rayliegh Number, which is used to determine the nusselt number of inside flow natural convection which is $T_s = 600$.

$$T_{flm} = \left(\frac{T_t + T_\infty}{2}\right) = \frac{403 + 600}{2} = 502°C \cong 774.5K$$

Properties of working fluid at film temperature are given as;

- Kinematics viscosity; $v = 95.4x10^{-6} \frac{kg}{ms}$
- Pradtle number; $Pr = 1.0075 \frac{m^2}{kg}$

$$Ra = \frac{g\beta(T_t - T_\infty)D^3}{v^2} Pr$$

$$\mathrm{Ra} = 12879$$

$$\mathrm{Nu_{NL}} \cong 6.92$$

The Nusselt number for pure forced laminar convection heat transfer is determined using (Aicher & Martin, 1997).

$$\mathrm{Nu_{FL}} = \left[3.66^3 + 0.7^3 + \left[1.615^3 \mathrm{x}\sqrt{\mathrm{Gz}} - 0.7\right]^3 + \left[\left(\frac{2}{1 + 22\mathrm{xPr}}\right)^{1/6} \mathrm{x}\sqrt{\mathrm{Gz}}\right]^3\right]^{1/3}$$

With the Graetz number defined by:

$$\mathrm{Gz} = \mathrm{Re.Pr.}\frac{\mathrm{d}}{\mathrm{L}}$$

Reynold Number: $\mathrm{Re_D} = \frac{\rho \mathrm{xVxD_h}}{\mu}$

Where D_h is given as: $\mathrm{D_h} = \frac{4\mathrm{A_h}}{\mathrm{p}} = \frac{4\pi \mathrm{D}^2/4}{\pi \mathrm{D}} = \mathrm{D}$

$$\mathrm{Re_D} = \frac{\mathrm{VxD}_h}{v} \cong 1057$$

Then $\mathrm{Gz} \cong 3.482$and $\mathrm{Nu_{FL}} \cong 7.479$

The mixed convection heat transfer Nusselt number is expressed as (Aicher & Martin, 1997):

$$\mathrm{Nu_M} = \sqrt{\mathrm{Nu_{FL}}^2 + \mathrm{Nu_{NL}}^2}$$

Then $\mathrm{Nu_M} \cong 10.189$, $\mathrm{h_{conv(in)}} = 192.5 \frac{\mathrm{W}}{\mathrm{m^2.k}}$ and $\mathrm{R_{conv(in),tube}} = 8.357 * 10^{-3} \frac{\mathrm{W}}{\mathrm{K}}$

$$\mathrm{T_s} = 636℃$$

Now use the surface temperature of the pipe $\mathrm{T_s} = 636℃$ and continue the iteration

$$\mathrm{T_{htf}} = \left(\frac{\mathrm{T_t} + \mathrm{T_\infty}}{2}\right) = \frac{403 + 636}{2} = 520 = 793K$$

Properties of working fluid at film temperature are given as;

- Kinematics viscosity; $\mathrm{v} = 100\mathrm{x}10^{-6} \frac{\mathrm{kg}}{\mathrm{ms}}$
- Pradtle number; $\mathrm{Pr} = 1.0093$

$$Ra = \frac{g\beta(T_t - T_\infty)D^3}{v^2} Pr$$

$$Ra = 13573$$

$$Nu_{NL} \cong 7.02$$

The Nusselt number for pure forced laminar convection heat transfer is determined using (Aicher & Martin, 1997).

$$Nu_{FL} = \left[3.66^3 + 0.7^3 + \left[1.615^3 x\sqrt{Gz} - 0.7\right]^3 + \left[\left(\frac{2}{1 + 22xPr}\right)^{1/6} x\sqrt{Gz}\right]^3\right]^{1/3}$$

With the Graetz number defined by:

$$Gz = Re.\,Pr.\frac{d}{L}$$

Reynold Number: $Re_D = \frac{\rho x V x D_h}{\mu}$

Where, D_h is given as: $D_h = \frac{4A_h}{p} = \frac{4\pi D^2/4}{\pi D}$

$$Re_D = \frac{VxD_h}{v} \cong 1008$$

Then $Gz \cong 3.33$and $Nu_{FL} \cong 7.32$

The mixed convection heat transfer Nusselt number is expressed as(Aicher & Martin, 1997):

$$Nu_M = \sqrt{{Nu_{FL}}^2 + {Nu_{NL}}^2}$$

Then $Nu_M \cong 10142$, $h_{conv(in)} = 191.575 \frac{W}{m^2.k}$ and $R_{conv(in),tube} = 8.395 * 10^{-3} \frac{W}{K}$

$$T_s = 637°C$$

Check the error

$$Error = \frac{637 - 636}{636} = 0.16$$

Therefore, the pipe outside temperature is determined from above equation and it is equals to 712.7°C

5.7 Thermal Energy Losses in the Receiver

Convection, emissive, and reflection heat losses are the three main types of heat losses to which the external receiver is subjected. In computations for thermal energy loss, conduction heat loss the lowest component of heat loss is typically ignored.

5.7.1 Convection Heat Loss

The external receiver's convection heat loss ($Q_{conv,\ air}$) results from convection loss between the body of the receiver and the surrounding air flow field. Considering a cylindrical receiver, the total convection losses are represented by;

$$\mathbf{Q_{conv,\ air}} = h_{\mathbf{total}} \mathbf{x}\, A_{re} \text{ x } (T_{surf} - T_{amb}) \tag{5.53}$$

Where h_{total} = the sum of the convection heat coefficients for forced and natural convection (W/m2K).

$$h_{total} = \left(h_{nc}^{3.2} + h_{fc}^{3.2}\right)^{1/3.2} \tag{5.54}$$

5.7.1.1 Forced Convection Coefficient

The wind speed (m/s) and roughness of the receiver surface directly affect forced convection heat loss. A cylindrical receiver surface's roughness is estimated and given by;

$$\text{Surface roughness} = \frac{r_{out}}{D_{re}} \tag{5.55}$$

Next, using the calculated surface roughness ($\frac{K_s}{D_{re}} = 222 \times 10^{-5}$) where K_s is effective sand grain roughness height. If a more accurate estimate cannot be found, it is advised to utilize the radius of a single receiver tube as a rough approximation for Ks. Since the surface roughness is found between $\frac{K_s}{D_{re}} = 75 \times 10^{-5}$ and $\frac{K_s}{D_{re}} = 300 \times 10^{-5}$ apply the liner interpolation to get the Nusselt number (Siebers & Kraabel, 1984).

At, $\frac{K_s}{D_{re}} = 75 \times 10^{-5},\ Nu_D = 0.3 + 0.488 * Re_D^{0.5}\left(1 + \left(\frac{Re_D}{282000}\right)^{0.625}\right)^{0.8}, Re < 7 \times 10^7$ (5.56)

For $\frac{K_s}{D_{re}} = 300 \times 10^{-5},\ Nu_D = 0.0135 R_e^{0.89},\ 1.8 \times 10^5 < Re < 4.0 \times 10^6$ (5.57)

Table 5. 3: Relationships for the theoretical physical properties in dry air

Property	Correlation
Fluid density (ρ), [kg/m^3]	$\rho_{air} = \frac{351.99}{T_{fm}} + \frac{344.84}{T_{fm}^2}$
Specific heat capacity, [J/(kg.K)]	$Cp_{air} = 1030.5 - 0.19975xT_{fm} + 3.9734x10^{-4}xT_{fm}^2$
Dynamic Viscosity[$10^{-6}pa.s$]	$\mu_{air} = \frac{1.4592xT_{fm}^{\frac{3}{2}}}{109.10 + T_{fm}}$
Thermal conductivity [w/(m.k)]	$K_{air} = \frac{2.334x10^{-3}xT_{fm}^{\frac{3}{2}}}{164.54 + T_{fm}}$

$$T_{fm} = \frac{T_{surf} + T_{amb}}{2} = 365℃ = \mathbf{638K}$$

$$\rho_{air} = \frac{351.99}{T_{fm}} + \frac{344.84}{T_{fm}^2} = 0.5524kg/m^3$$

$$Cp_{air} = 1030.5 - 0.19975xT_{fm} + 3.9734x10^{-4}xT_{fm}^2 = 1064.8\frac{J}{Kg.K}$$

$$\mu_{air} = \frac{1.4592xT_{fm}^{\frac{3}{2}}}{109.10 + T_{fm}} = 24.26x10^{-6}\frac{Kg}{ms}$$

$$K_{air} = \frac{2.334x10^{-3}xT_{fm}^{\frac{3}{2}}}{164.54 + T_{fm}} = 0.0469\frac{W}{mk}$$

$$Re_D = \frac{D_{re}\ x\ v_{wind} x\ \rho_{air}}{\mu_{air}} \cong 204{,}930$$

Where v_{wind} = Annual average wind speed of the area 1 $\frac{m}{s}$

Then $Nu_D = 594.4$ and the forced convection coefficient (h_{fc}) is calculated as;

$$h_{fc} = \frac{Nu_D\ x\ K_{air,flm}}{D_{re}} = 3.0954\frac{W}{m^2.k}$$

Where K_{air} is the thermal conductivity of the air (in W/mK), D_{re} is the receiver diameter (in m), and $Nu_D$is the average Nusselt number.

5.7.1.2 Natural Convection Coefficient

Because of its exceptionally large receiver diameter, the external receiver can be treated as a vertical plate in natural convection analysis, hence ignoring curvature effects. (Siebers & Kraabel, 1984). On such a vertical flat surface, natural convection flow will usually be turbulent along most of the surface height due to the large size and high operating temperature. The following correlation can be used to compute the heat transfers from cylindrical, external-type receivers via pure turbulent natural convection.

$$\mathrm{Nu_h} = 0.098\mathrm{x}\mathrm{Gr_H}^{1/3}\left(\frac{\mathrm{T_{sur}}}{\mathrm{T_\infty}}\right)^{-0.14} = 816.43 \qquad (5.58)$$

Where $\mathrm{Gr_H}$is the dimensionless parameter of the Grashof number, $\mathrm{T_{sur}}$ is surface temperature, and $T_\infty$is ambient temperature, when each property is evaluated at $\mathrm{T_\infty}$. $\mathrm{Gr_H}$, or the Grashof number, can be computed by;

$$\mathrm{Gr_H} = \frac{\mathrm{g\ x\ \beta\ x\ (T_{surf} - T_{amb})\ x\ H_{re}^3}}{\mathrm{V^2}}\mathrm{xPr} = 9.64\mathrm{x}10^{11}$$

Where, v = the kinematic viscosity of the air (101.26x10^{-6}m^2/s), g(m/s^2) = the

Gravitational acceleration, Pradtle number$(\mathrm{Pr}) = 0.6967$ and β is the volume expansion

coefficient ($\frac{1}{T_{fm}}$, 1/K).

The natural convection coefficient ($\mathrm{h_{nc}}$) can then be calculated using

$$\mathrm{h_{nc}} = \frac{\mathrm{Nu_h\ x\ K_{air,flm}}}{\mathrm{H_{re}}} = 3.48\frac{\mathrm{W}}{\mathrm{m^2.k}}$$

The $\mathrm{h_{total}} = 4.098\frac{\mathbf{W}}{\mathbf{m^2.k}}$ and $\mathbf{Q_{conv,\ air}} = 0.836\mathrm{MW}$

5.7.2 Emissive Heat Loss

Emissions of heat result from the outer receiver wall's discharge of infrared radiation. After that, utilizing can be used to compute the overall emissive heat loss.

$$\mathrm{Q_{em}} = \varepsilon\ \mathrm{x}\ \sigma\ \mathrm{x}\ \mathrm{A_{re}}\ \mathrm{x}\left(\mathrm{T_{surf}^4} - \mathrm{T_{amb}^4}\right) \qquad (5.59)$$

When σ is the Stefan-Boltzmann constant (5.67 10^{-8} W/m^{2}K^4) and ε is the emissivity of the coated surface =0.9.

5.7.3 Reflective Heat Loss

Due to the receiver material's reflectivity, which is intended for an opaque surface, there is reflective heat loss.

$$\text{Reflectivity} = 1 - \alpha$$

Where α is the surface absorptivity =0.95; as a result, Q_{ref} (W) is the reflected heat loss for an external receiver.

$$Q_{ref} = (1 - \alpha)\, xQ_{re} \qquad (5.60)$$

5.7.4 Exergy efficiency of the receiver

A portion of the energy contained in the isolation Q* rec is transferred by the receiver to the fluid passing through it in order to facilitate heat transfer. The total exergetics power input from the heliostat field to the receiver is expressed as by (Boukelia et al., 2020).

$$\Psi^{*}_{rec} = Ex_{in} = Q_{rec}\left(1 - \frac{T_o}{T_r}\right) \qquad (5.61)$$

Where: $Q_{rec}$is the receiver's net energy interception rate, and Tr is the temperature that the receiver has absorbed.

This formula determines the exergy rate carried heat transfer fluid (Ratlamwala et al., 2012)

$$\Psi^{*}_{rec,abs} = Ex_u = Q_u\left(1 - \frac{T_o}{T_{htf,o}}\right) \qquad (5.62)$$

Where $Q_u = Q_{HTF} =$ energy received by heat transfer fluid and then

Therefore, the central receiver subsystem's energy efficiency and exergy efficiency are defined as (Atif & Al-Sulaiman, 2018) (Boukelia et al., 2020);

$$\eta_{I,rec} = \frac{Q_{HTF}}{Q^{*}_{rec}}$$

$$\eta_{II,rec} = \frac{Ex_u}{Ex_{in}}$$

5.7.5 Energy and exergy analysis for the heliostat field

The sun's beams are reflected and concentrated onto the central receiver by the heliostat field, which has a total aperture area of A_h and is composed of dozens or hundreds of heliostats. The entire isolation is related to the entire region and can be supplied as (Xu et al., 2011) (Atif & Al-Sulaiman, 2018).

$$Q^* = A_h \times q^* \tag{5.63}$$

Where q^* stands for the amount of solar energy received per square meter, which is believed to be the direct normal irradiation (DNI) (Xu et al., 2011).It should be noted that the DNI fluctuates depending on a number of variables, including one's location on the globe, the weather, and the time of day. Nonetheless, it is assumed that the system is in a steady state and that q* is a constant.

The heliostat field partially delivers the incident solar radiation Q^* to the central receiver as solar isolation Q^*_{rec}, while remaining fractionQ^*_0 is lost to the environment as a result of various loss mechanisms.

Hence, the heliostat field's energy balance and exergy balance are given by;

$$Q^* = Q_{solar} = Q^*_{rec} + Q^*_0 \tag{5.64}$$

$$\Psi^* = \Psi^*_{rec} + \Psi^*_0 \tag{5.65}$$

Where, Ψ^*_0 is the exergy lost (irreversibility) and Ψ^*_{rec} is the exergy provided to the receiver.

The solar radiation-related exergy on the heliostat mirror surface is provided by (Boukelia et al., 2020)

$$\Psi^* = Ex_{solar} = Q_{solar} * \left[1 - \frac{4T_{amb}}{3T_{sun}}(1 - 0.28lnf)\right] \tag{5.66}$$

In this case, f is the dilution factor ($1.3*10^{-5}$) denotes the mixing ratio of solar energy from the sun (T_{sun}) to radiation from the environment (Boukelia et al., 2020). Where T_{sun} is the sun's outer surface temperature, which is 5,800 K and T_o is assumed to be the ambient temperature (Atif & Al-Sulaiman, 2018).

The heliostat field's exergy destruction rate is therefore given as:

$$Ex_{d,heliostat} = Ex_{solar} - Ex_{in} \tag{5.67}$$

Following that, the heliostat field subsystem's energy and exergy efficiencies are provided by (Boukelia et al., 2020):

$$\eta_{I,h} = \frac{Q^*_{rec}}{Q^*} \ and \ \eta_{II,h} = \frac{\Psi^*_{rec}}{\Psi^*} \quad (5.68\ )$$

5.7.6 Pump Power

$$\dot{W}_{pump} = \frac{Qx\Delta P_{total}}{\eta_{pump}} \quad (5.69)$$

Where Q is the HTF volume flow rate (in m3/s), ΔP_{total} is the total pressure drop in Pa, η_{pump} is the pump efficiency, which is assumed to be a constant 75%, and $\dot{W}$ is the needed pump power (in W)(Albarbar & Arar, 2019).

The mass flow rate ($\dot{m}$) and fluid density (ρ) can be used to compute the volume flow rate (Q).

$$Q = \frac{\dot{m}_{total}}{\rho} \quad (5.70)$$

There are two primary causes of pressure loss in a receiver: first, as indicated by the equation below, pumping heat transfer fluid to the receiver's location at the summit of a solar tower:

$$\Delta P_{tower} = \rho_w x g x H_{tower} \quad (5.71)$$

Where, H_{tower} tower height.

Second, pressure drop is a result of pumping HTF through the receiver tubes, and the following equation can be used to calculate it: In actuality, the pressure drop for all internal flow types—laminar or turbulent, circular or noncircular tubes, smooth or rough surfaces is found to be conveniently expressed as.

$$\Delta P_{tube} = \rho_w * f * \frac{H_{re}}{D_{in}} * \frac{X^2_{tube}}{2} \quad (5.72)$$

The flow is laminar because of the Reynold number, which is computed above when calculating the internal convection coefficient and equals 1008

Circular Tube, laminar: $f = \frac{64\mu}{\rho D V_m} = \frac{64}{Re}$

Where, f = the smooth tube's fiction factor in turbulent flow. The tower pressure drop plus the reception tube pressure drop add up to the total pressure drop, which is calculated as follows:

$$\Delta P_{total} = \Delta P_{tube} x \frac{n_{header/receiver}}{n_{flow\ path}} + \Delta P_{tower} \quad (5.73)$$

5.7.7 Baking System's Thermal Efficiency

The system thermal efficiency is the ratio of net usable energy used to the gross energy supply, which is calculated by:

$$\text{Thermal efficiency} = \eta_{\text{pthermal}} = \frac{\text{Usefull energy utilized}}{\text{Gross input energy required}} = \frac{E_{\text{Usefull}}}{E_{\text{Gross}}} \qquad (5.74)$$

Determination of the total amount of steam needed in a single session

A. Amount of heat required per a day or total energy required to bake 6000 injera as determined above is
= 2565MJ

B. The mass of water vapour necessary to produce the appropriate level of heat is
$M_{total} = \frac{Q_{total}}{C_p * \Delta T}$

By considering loses in the whole system including steam released through relief valve total mass of water vapour required increased by two.

$$M_{\text{total}} = \mathbf{2} * \frac{2565000\text{Kj}}{4.187 * (538 - 18.41)} = \mathbf{2,358\ Kg}$$

Then amount of vapour required to bake a single injera is 0.393

Design of cold water storage tanker: a cold water storage tank is cylindrical structures which have a size of

$$V_c = \frac{Q_{\text{total}}}{C_p * \rho_{\text{water}} * \Delta T} \qquad (5.75)$$

$$= \frac{2565000\text{KJ}}{4.187\frac{\text{KJ}}{\text{kg.k}} * 1000\frac{\text{kg}}{\text{m}^3} * (250 - 18.41)} = 2.645\text{m}^3$$

Assume the tank is filled twice per a day and considering the thermal expansion of water, it seems sense to believe that the capacity of the water chamber may have increased by two times is $\frac{2.645*2}{2}\text{m}^3 = 2645\text{litter}$.

Design of hot water storage tanker: a hot water tank is cylindrical structures which have a size of

$$V_c = \frac{M_{\text{total}}}{\rho_w}$$

Because of the thermal expansion of water, it seems sense to believe that the capacity of the water chamber may have increased by four times $9.432\text{m}^3 = 9432$ litter.

A. Volume of cavity under the mitad needed for baking one injera is

$$V = \frac{m}{\rho} \tag{5.76}$$

5.7.8 Flow of Energy from Sun to Baking pan

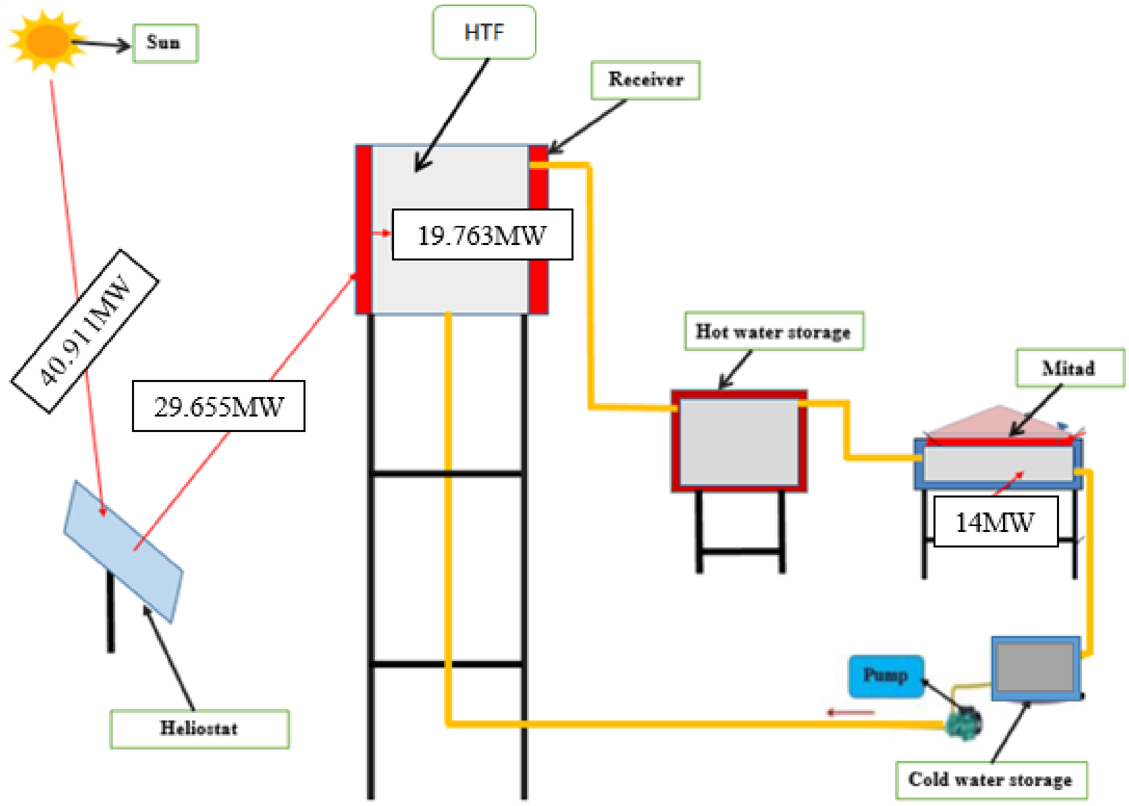

Figure 5. 10: Energy flow diagram

5.8 Mathematical Modeling for Baking Pan

The mathematical model for the baking pan was constructed based on the following assumptions in order to analyze the heat-up time:

- The temperature fluctuates exclusively along the thickness or in an axial direction.
- There's no production of heat.
- The baking pan's thermal conductivity remains consistent.
- When the pan is first heating up, it is left uncovered.

- The amount of heat lost through the left and right edges and the glazing material between the pan and the hot water negligible.

General 1D Transient Heat Conduction Equation

$$\rho C_p \frac{\partial T}{\partial t} = K \frac{\partial^2 T}{\partial x^2} \tag{5.77}$$

$$\frac{\partial T}{\partial t} = \alpha \frac{\partial^2 T}{\partial x^2} \tag{5.78}$$

Where ρ is density (kg/ m 3), $\boldsymbol{C_p}$ specific heat capacity (J /kg.K) and T is temperature of baking pan vary with space and time.

Density of mitad is given as:

$$\rho = \frac{m}{V} = \frac{7\text{Kg}}{\left(3.14 * 0.02 * \frac{0.58^2}{4} \text{m}^3\right)} = 1325 \frac{\text{kg}}{\text{m}^3}$$

Initial and boundary conditions

Initial condition at t *=0*

The baking pan is initially at a constant room temperature.

T_{initial} =18.41°C

Boundary Conditions for t >0

At x = 0 (at the bottom of the baking pan)

T_{bottom} = lower surface temperature of the pan (T_{lsp}) = 423°C

Internal Node: Through conduction, the internal node directly interacts with both of its surrounding nodes. The temperature of node I at t + 1-time step is stated clearly as follows:

$$\left(\frac{T_i^{n+1} - T_i^n}{\Delta t}\right) = \alpha * \left(\frac{T_{i-1}^n - 2 * T_i^n + T_{i+1}^n}{\Delta x^2}\right) \tag{5.79}$$

$$T_i^{n+1} = T_i^n + \left(\frac{\alpha * \Delta t}{\Delta x^2}\right) * (T_{i-1}^n - 2 * T_i^n + T_{i+1}^n) \tag{5.80}$$

Let $\boldsymbol{\tau} = \left(\frac{\alpha * \Delta t}{\Delta x^2}\right)$ Where $\boldsymbol{\tau}$ – diffusion number,

$\alpha = \frac{\boldsymbol{k}}{\boldsymbol{\rho C_p}}$**,** heat diffusivity

t- Represents the time step

Δt – Small time change of total time for simulation

$$T_i^{n+1} = T_i^n + \tau * (T_{i-1}^n - 2 * T_i^n + T_{i+1}^n) \qquad (5.81)$$

Where, i represent the node location on discretized domain.

Now let us discretize the 1D domain in to (say 20) segments or equally spaced grid

1----2-----3------4----5---20

Note temperature at node 1 is known and we have convection BCs at last node.

To apply equation 5.81, we consider interior node

Let i = 2 and n = 0 Eq 5.81) becomes

$T_2^1 = T_2^0 + \boldsymbol{\tau} * (T_1^0 - 2 * T_2^0 + T_3^0)$;

Similarly, for i = 3, 4, 5...20and n = 0 we get

$$T_3^1 = T_3^0 + \boldsymbol{\tau} * (T_2^0 - 2 * T_3^0 + T_4^0)$$

$$T_4^1 = T_4^0 + \boldsymbol{\tau} * (T_3^0 - 2 * T_4^0 + T_5^0)$$

$$T_5^1 = T_5^0 + \boldsymbol{\tau} * (T_4^0 - 2 * T_5^0 + T_6^0)$$

.

$$T_{19}^1 = T_{19}^0 + \boldsymbol{\tau} * (T_{18}^0 - 2 * T_{19}^0 + T_{20}^0)$$

The Upper Surface (N^{th}) Node: presuming that radiation heat transfer has no influence and that the upper surface of the baking pan is exposed to air convection during the heating up process. It is possible to express the node's heat balance clearly as follows:

$$-k * A * \frac{\partial T}{\partial t} + h * A * (T_\infty - T_i^n) = \rho * C_p \left(\frac{\Delta x}{2}\right) * A * \frac{\partial T}{\partial t} \qquad (5.82)$$

$$-k * \left(\frac{T_i^n - T_{i-1}^n}{\partial x}\right) + h * (T_\infty - T_n^t) = \rho * C_p \left(\frac{\Delta x}{2}\right) * \frac{T_i^{n+1} - T_i^n}{\partial t}$$

$$T_i^{n+1} = (Fo) * \left((2 * Bi) * T_\infty + 2 * T_{i-1}^n \left(\left(\frac{1}{Fo}\right) - (2 * Bi)\right) * T_i^n\right) \tag{5.83}$$

5.8.1 Analyzing Pan Surface Heat Transfer Coefficients

5.8.1.1 Convection and Radiation heat loss during heating and re-heating up

It is believed that 200 °C is the standard baking temperature, or the mitad surface temperature, at which baking can start.

1. **Convective Heat Transfer Coefficient**

   Free convection heat transfers to the surrounding area of the baking pan both during the heating process and in between baking cycles. Transient convective heat transfer happens between a fluid medium and the solid food item in various food processing applications, such as cooling.

   The coefficient of heat transfers from the surface of the pan to the surrounding s;

$$h_c = Nu \frac{K}{L_c}$$

Where, Nu– is the Nusselt number

k – Thermal conductivity of evaporated water fluid

L_c – The characteristic length

For a horizontal circular plate, the effective length of the heat transfer surface can be computed using the relationship.

$$L_c = \frac{A_s}{P}$$

Where, $A_s$the surface area and p is the perimeter. Effective length is D/4 for a circular horizontal surface diameter D (Bergman, 2011).

$$D_h = \frac{A}{P} = \frac{\pi D^2}{4\pi D} = \frac{D}{4} = 0.145m$$

The air characteristics will be taken into consideration at the mean temperature between the pan and surround in order to calculate the convective heat transfer coefficient between them.

$$T_m = \frac{T_{amb} + T_p}{2} = \frac{200 + 18.41}{2} = 110°C$$

Properties at the average film temperature:

- Thermal of air K=0.03242
- Kinematics viscosity; $v = 24.152\text{x}10^{-6}\,\frac{m^2}{s}$
- Pradtle number; $Pr = 0.69172\,\frac{m^2}{kg}$
- Thermal diffusivity , $\alpha = 3.231\text{x}10^{-5}\,\frac{m^2}{s}$

A dimensionless parameter called the Raleigh Number can be computed using (Kitamura & Kimura, 2008).

$$Ra_D = \frac{g\beta(T_\infty - T_s){D_h}^3}{\alpha v}$$

The non-dimensional parameters' thermo-physical characteristics were evaluated at the film temperatures, and the volume expansion coefficient (β) for air was computed using the formula β = 1/T∞.

Total Nusselt numbers of natural convection over horizontally heated, upward-facing circular discs (Kitamura & Kimura, 2008)

$$\text{Nusselt number,} \begin{bmatrix} Nu = 0.71 * {Ra_D}^{1/4},\ \text{for } 2x10^5 < Ra_D < 4\text{x}10^7 \\ Nu = 0.16 * {Ra_L}^{1/3},\text{for } 4x10^7 < Ra_D < 3\text{x}10^{10} \end{bmatrix} \qquad (5.84)$$

Next, $R\alpha = 3.3\text{x}10^8$ is discovered between $4x10^7 < Ra_D < 3\text{x}10^{10}$ therefore the nusselt number is determined using the second equation and $Nu = 111$

Hence, the average convective heat transfer coefficient can be determined using the formula

$h = \frac{Nuk_{htf}}{D_h} = \mathbf{25}\,\frac{\mathbf{W}}{\mathbf{m^2.k}}$

2. **Radiative heat transfer coefficient**

Since it is anticipated that the mitad would remain open during heating and reheating, the radiative heat transfer coefficient from the surface of the baking pan to the surrounding area is given as:

$$h_r = \varepsilon_p \sigma \frac{\left(T_p + 273\right)^4 - (T_{amb} + 273)^4}{\left(T_p - T_{amb}\right)} \qquad (5.85)$$

Where; $\boldsymbol{\sigma}$ – Stefan Boltzmann constant [$5.67x10^{-8}$ W/m^2.K],

T_p – surface baking pan temperature

T_{amb} – ambient temperature

$\varepsilon_\mathbf{p}$ –Emissivity of the baking pans or fired clay which is 0.91given by:

The radiative heat transfer coefficients of pan are determined as:

$$\mathrm{h_r} = 0.91 * 5.67\mathrm{x}10^{-8} * \frac{(200+273)^4 - (18.41+273)^4}{(200-18.41)} \cong \mathbf{14}\,\frac{\mathbf{W}}{\mathbf{m^2k}}$$

5.8.1.2 Convection and Radiation heat loss during Injera baking

Convective Heat Transfer Coefficient from Injera to lid cover.

One can compute the dimensionless parameter known as the Raleigh Number using

(Kitamura & Kimura, 2008).

$$\mathrm{Ra}_D = \frac{\mathrm{g}\beta(\mathrm{T}_\infty - \mathrm{T_s})D_h{}^3}{\alpha\mathrm{v}}$$

The thermo-physical properties of the non-dimensional parameters were assessed at the film temperatures and the formula $\beta = 1/T\infty$ was used to get the volume expansion coefficient (β) for air.

Total Nusselt numbers of natural convection over horizontally heated, upward-facing circular discs (Kitamura & Kimura, 2008).

Nusselt number,
$$\mathrm{Nu} = 0.71 * \mathrm{Ra_D}^{1/4}, \text{ for } 2x10^5 < \mathrm{Ra_D} < 4\mathrm{x}10^7$$
$$\mathrm{Nu} = 0.16 * \mathrm{Ra_L}^{1/3}, \text{for } 4x10^7 < \mathrm{Ra_D} < 3\mathrm{x}10^{10}$$

According to the heat and mass transfer data handbook, the characteristics of water vapor at film temperature are: $\mathrm{T_{flm}} = 127.5°\mathrm{C}$

- Kinematics viscosity; $\mathrm{v} = 24.34\mathrm{x}10^{-6}\,\frac{\mathrm{m}^2}{\mathrm{s}}$
- Coefficient of thermal expansion $\beta = \frac{1}{\mathrm{T}} = \frac{0.25*10^{-2}}{\mathrm{K}}$
- Pradtle number; $\mathrm{Pr} = 1.0598\,\frac{\mathrm{m}^2}{\mathrm{kg}}$
- Thermal diffusivity , $\alpha = 2.34\mathrm{x}10^{-5}\,\frac{\mathrm{m}^2}{\mathrm{s}}$

Where, $A_s$the surface area and p is the perimeter**.** Effective length is D/4 for a circular horizontal surface diameter D (Bergman, 2011)

$$D_h = \frac{A}{P} = \frac{\pi D^2}{4\pi D} = \frac{D}{4} = 0.145\mathrm{m}$$

Then $R\alpha = 1.94\mathrm{x}10^7$ and $\mathrm{Nu} = 47.16$

Hence, the average convective heat transfer coefficient can be determined using the formula

$$h = \frac{\mathrm{Nu}k_w}{L} = 221.16 \frac{W}{m^2.k}$$

Convection heat transfer coefficient from the lid covers to the ambient.

Additionally, the convection heat transfer coefficient between the ambient and lid cover is equal to $6.8\frac{W}{m^2k}$

Radiation from lid cover to ambient or surrounding

The sky temperature or (temperature of the surrounding) (T_{sky}) given by (Rawat, 2017):

$$T_{sky}=Ta - 6 = 12.41℃$$

And the radiative heat transfer coefficient is expressed as:

$$h_{2r} = \varepsilon_{lc}\sigma \frac{(T_{lc} + 273)^4 - \left(T_{sky} + 273\right)^4}{\left(T_{lc} - T_{sky}\right)} = \mathbf{6.3}\frac{W}{m^2k}$$

Where, T_{lc}- temperatures of lid cover (^{0}C).

5.9 Economic Analysis

5.9.1 Investment cost

The total installed costs during the building of the power tower plants are split into two categories: direct and indirect capital costs (Pidaparthi, 2017).

5.9.1.1 Direct Capital Cost

Thermal energy storage, site upgrades, tower and receiver, Injera baking system and heliostat field system expenditures are examples of direct capital costs. Several unknowns in the assessment of these direct expenses cannot be predicted during the project's building phase. An additional percentage is added to the sum direct costs to account for these risks (Pidaparthi, 2017) (Blampain, 2018).

5.9.1.1.1 Heliostat field Cost

The foundation, steel supporting structure, motors and controls, mirrors, and assembly (including installation and checkout) are all included in the heliostat field costs. This cost is then multiplied by volume effects (which account for learning curve advantages indicated by a progress ratio p_r), cost effects (caused by scaling factor s), and price index pi (which represents variations in heliostat sub-costs over time). The scaling effect is the ratio of the heliostat area under inquiry, Ah, to that of the reference heliostat, A0h, with s as the exponent. It deals with changing the heliostat sizes (Augsburger, 2013; Blampain, 2018; Pidaparthi, 2017).

$$C_{h,tot} = C_h x N_{hel} \qquad (5.86)$$

Where

$$C_h = C_o x \left(\frac{A_h}{A_h^o}\right)^s x(pr)^{\log_2 \left(\frac{V_h}{V_h^o}\right)} xpi \qquad (5.87)$$

Where $A_h^o = 43.3m^2$ and $V_h^o = 21500$ (Pidaparthi, 2017)

5.9.1.1.2 Individual optical enhancement of heliostats

The optical quality of a heliostat is a measure of its ability to reflect a circular and a specular picture on the receiver surface. (Pidaparthi, 2017). The tracking error and the slope are included in a single "root-sum-square" (RSS) number that is "bundled" to calculate these costs (Augsburger, 2013; Pidaparthi, 2017). Savings on costs are shown with a negative number. The heliostat optical improvement cost is expressed as the sum of the optical improvement costs for each heliostat (C h, optic) and the heliostats overall (C h, opt):

$$C_{h,opt} = C_{h,optic} x N_{hel} \qquad (5.89)$$

Where

$$C_{h,optic} = 0.01x10^{-3} x \left(\frac{1}{\sigma_{rss}^2} - \frac{1}{{\sigma_{rss}^o}^2}\right) x A_h \qquad (5.90)$$

With $\sigma_{rss}^o = 4.14mrad$ and $\sigma_{rss} = 2.6mrad$ (Augsburger, 2013) and The optical improvement cost per heliostat ($C_{h, optic}$) is =**14.34$**

5.9.1.1.3 Site modification

The construction of roads, fences, storm water control systems, water delivery infrastructure, and blow down evaporation ponds are examples of site improvements (Pidaparthi, 2017).The total reflecting area of the heliostat field, A_{sf}, and the site improvement cost per square meter, C_s = 16 \$/m2, are used to determine the overall site improvement cost as follows:

$$C_{s,tot} = C_s x A_{sf} \qquad (5.91)$$

5.9.1.1.4 Cost of the Tower

The tower cost $C_{t,\,tot}$ is determined by the tower height H_t the fixed tower cost $C_{t,\,fixed}$ and an exponential term that depends on the tower cost scaling exponent k_t. When calculating the tower's scaling costs with height, the fixed tower cost is used as the base amount (Augsburger, 2013; Pidaparthi, 2017). The fixed tower cost for a tower height of 30 < H < 90 meters is \$226,000. Thus, the entire tower cost $C_{t,\,tot}$ can be written as follows:

$$C_{t,tot} = C_{t,fixed} x e^{k_t x H_t} \qquad (5.92)$$

Where $k_t = 0.0113$ (Pidaparthi, 2017)

5.9.1.1.5 Receiver cost

The receiver's price is contingent upon both its specific type and its location. The receiver cost, $C_{r,\,tot}$ is computed similarly to the tower cost. The ratio of the receiver area A_{rec} to that of the reference receiver A^0_{rec} is multiplied by the reference receiver cost $C_{r,\,ref}$ (Augsburger, 2013; Pidaparthi, 2017). There is a scaling exponent rec k that applies to this ratio. For the Water/Steam External Receiver, the reference receiver cost equals$c_{r,ref} = \$\,72{,}740$. At this point, the receiver cost can be computed as:

$$C_{r,tot} = C_{r,ref} x \left(\frac{A_{rec}}{A^0_{rec}}\right)^{k_{rec}} \qquad (5.93)$$

Where, A_{rec} = receiver area, $k_{rec} = 0.7$ and A^0_{rec} = reference receiver area

The cost for the heliostat field, the tower and receiver, and site preparation can now be added together to determine the subtotal direct cost of the plant, or $C_{d,\,s}$.

$$C_{d,s} = C_{r,tot} + C_{t,tot} + C_{h,tot} + C_{s,tot} \qquad (5.94)$$

5.9.1.1.6 Contingency

During the construction stage, there may be some uncertainty in the predicted costs for each of the direct cost categories that were computed above (Blampain, 2018). As a percentage of the subtotal direct costs, a contingency CP is therefore applied (Pidaparthi, 2017). The following formula is used to get the contingency costs, $C_{c\ tot}$:

$$C_{c,tot} = C_{d,s} x CP \tag{5.95}$$

With CP = 5% (Pidaparthi, 2017)

By adding the subtotal direct costs and the contingency costs, the total direct costs of the plant $C_{d,\ tot}$ may now be computed and are given as follows:

$$C_{d,tot} = C_{d,s} + C_{c,tot} \tag{5.96}$$

5.9.1.2 Indirect costs

The cost for engineering, procurement, and construction (EPC), the cost of buying the land needed for the plant, and a sales tax paid as a percentage of the total direct cost are all included in these cost (Pidaparthi, 2017).

5.9.1.2.1 Engineering, Procurement and Construction

The plant's design and construction are covered by the EPC expenditures. Examples of expenses that fall under this category include commissioning fees, legal fees, site studies, permits, and inventories of spare parts (Pidaparthi, 2017). Now, the entire EPC cost, $C_{EPC,\ tot}$ can be written as follows:

$$C_{EPC,tot} = C_{d,tot} x EPCP \tag{5.97}$$

With EPCP = 5 % (Weinrebe et al., 2014)

5.9.1.2.2 Cost of Land

The expenditures associated with buying the land are the land costs for the plant. The entire land area needed A_l, multiplied by the cost per total land area, C_l yields the total cost of the land, $C_{l,tot}$. The land area is given in acres.

$$C_{l,tot} = C_l x A_l \tag{5.98}$$

5.9.1.2.3 Sales tax

As a percentage of the total amount of direct charges, sales tax is a one-time tax that is imposed. A sales tax rate (STR) and the percentage basis (STB) of the total direct costs are used to calculate the sales tax cost, or CST. Here is one way to depict it:

$$C_{ST,\text{tot}} = STRxSTBxC_{\text{d,tot}} \tag{5.99}$$

Sales tax basis of total direct costs (%) 80 and Sales tax rate (%) 14.5 (Pidaparthi, 2017). By adding up the subtotal indirect costs, the plant's total indirect costs may be determined and are represented as follows:

$$C_{\text{i,tot}} = C_{\text{EPC,tot}} + C_{\text{l,tot}} + C_{ST,\text{tot}} \tag{5.100}$$

The complete direct and indirect costs can now be added up to determine the overall installed costs of the power tower plant in $C_{\text{inst, tot}}$.

$$C_{\text{inst,tot}} = C_{\text{d,tot}} + C_{i,\text{tot}} \tag{5.90}$$

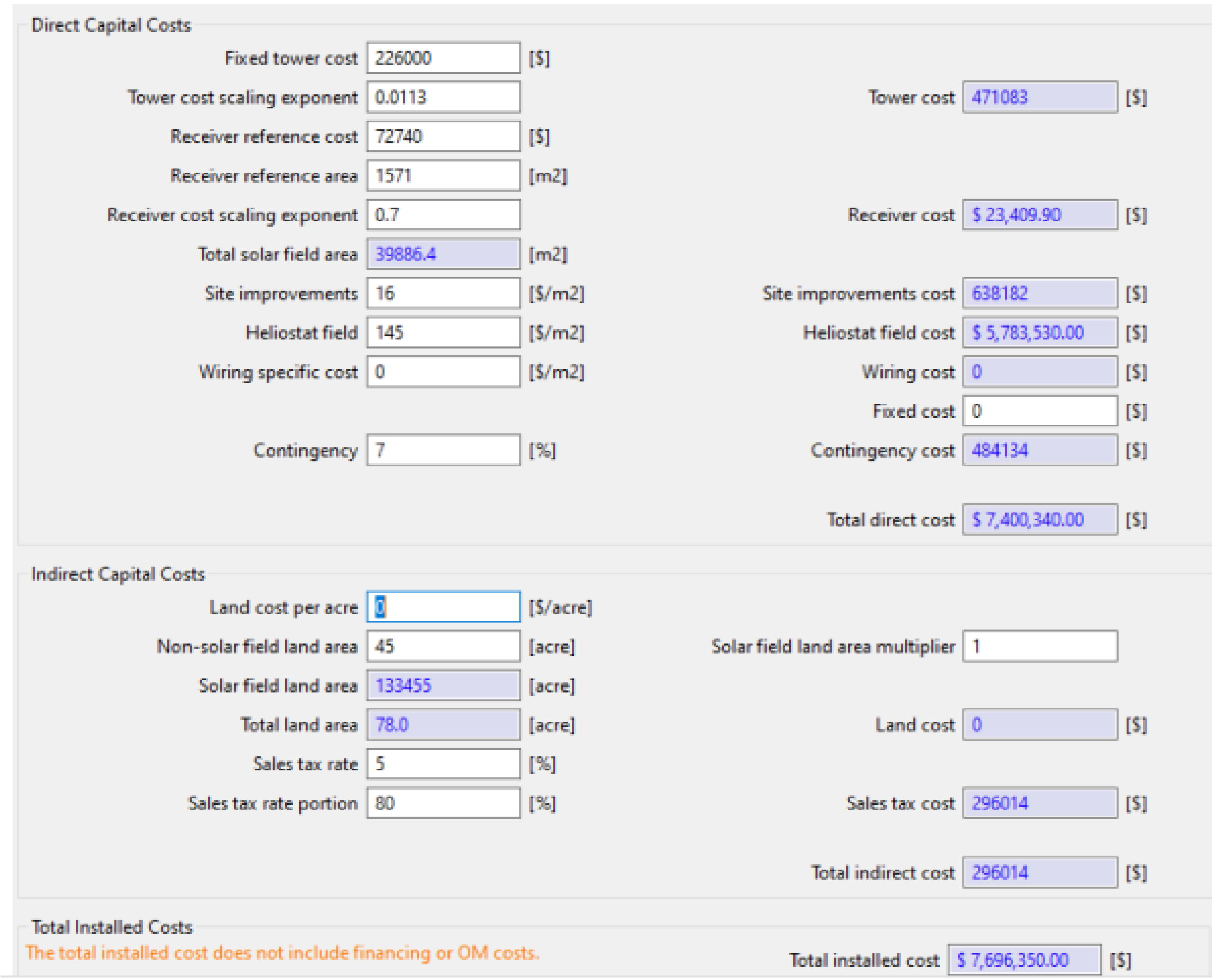

Figure 5. 11: Cost analysis using Solar Pilot

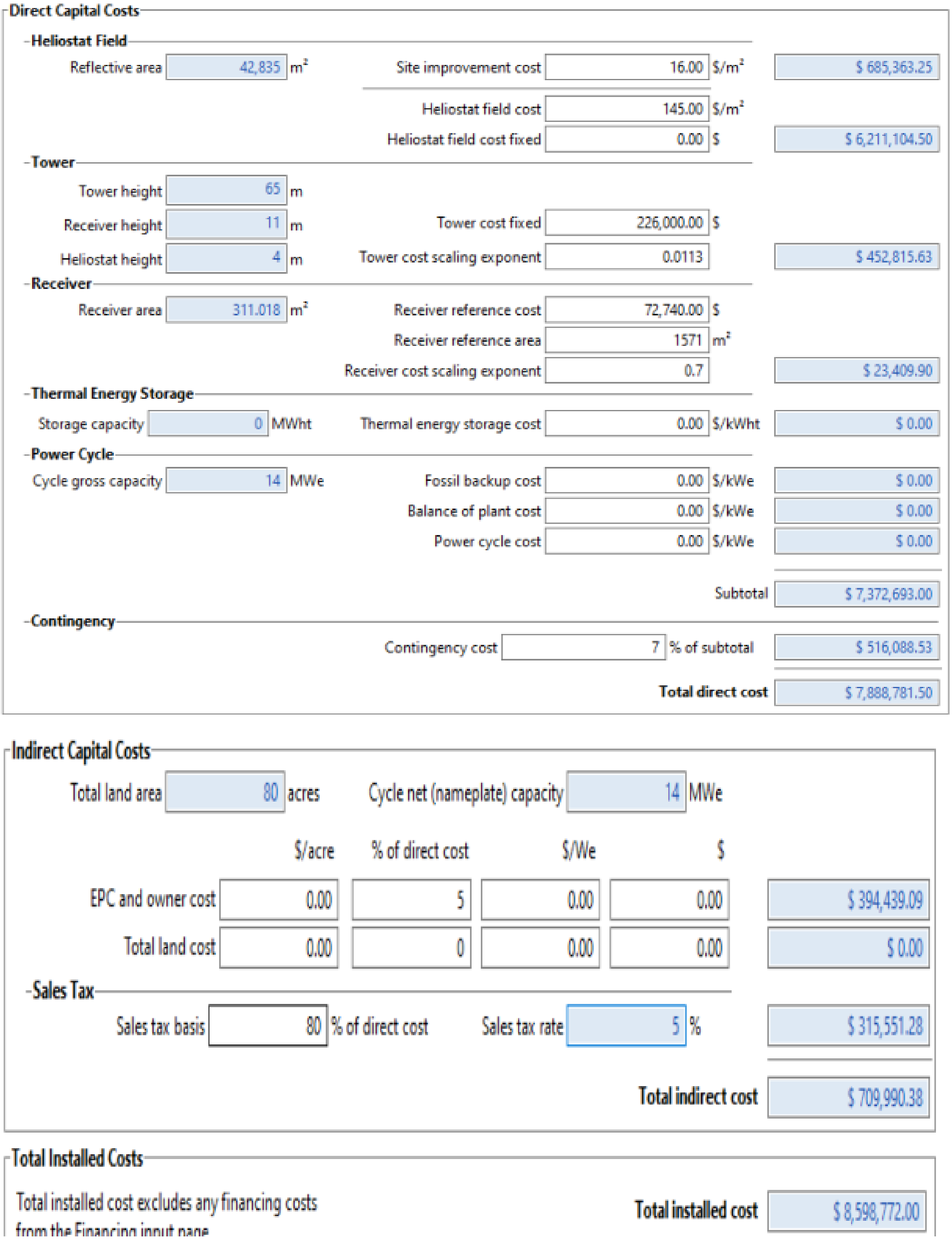

Figure 5. 12: Cost analysis of power tower using SAM software

Table 5. 4: Comparison of SAM and Solar Pilot

	SAM	Solar Pilot
Total heliostat reflective area (m2)	43,797	39,886
Heliostat field Cost ($)	6,211,104.50	5,783,530.00
Site improvement cost($)	685,363.2	5 63,8182
Receiver cost ($)	23,409.90	23,409.90
Tower cost ($)	452,815.63	471,083
Contingency cost ($)	516,088.53	484,134
Total Direct Cost ($)	**7,888,781.50**	**7,400,340.00**
Engineering, procurement and construct ($).	394,439.09	-------------
Sales tax cost ($)	315,551.28	296,014
Total Indirect Cost($)	**709,990.38**	**296,014**
Total Installed Cost($)	**8,598,772.00**	**7,696,350.00**

Transport costs and supplier profit should be taken into account, as the power tower system's cost is determined using international prices. Assume supplier profit accounts for 20% of total costs and transportation accounts for 10%. The equipment costs $ 8,598,772.00 in international price.

Special transport cost is calculated at 10% of total costs ($8,598,772.00* 10% = **$ 859,877.20).** Before profit, the total installed cost is $**859,877.20** + $ 8,598,772.00= **$9,458,649.2** Supplier profit (estimated at 20% of total installed cost (before profit)): $**9,458,649.2*** 20% = **$1,891,729.84**

Solar Power tower system total installation cost (including profit) = Supplier profit + total installed cost (before profit) = ($**9,458,649.2** + $**1,891,729.84**) = **$11,350,379.04**

5.9.2 Maintenance and operations (O&M)

Multiple approaches have been used to analyze the operations and maintenance (O&M) costs of a power tower plant. The annual rate of 2% of the total investment is used by (Pidaparthi, 2017) to calculate the O&M expenses. Then total maintenance and operations cost of the Power system is **$ 227,007.58**

5.9.3 Cost of Injera Baking System

Each material utilized in the fabrication process, as well as the cost of hiring labor and professionals, must be known in order to determine the cost of the solar thermal injera baking system.

5.9.3.1 Material cost

Table 5. 5: List of materials used, along with their related costs, to build the mitad

Material	Use	Specification	Quantity	Unit price (ETB)	Total price (ETB)
Stainless steel sheet	Cold water storage tank	$1m \times 2m \times 2mm$	7	5,330	37,310
Stainless steel sheet	Hot water storage tank	$1m \times 2m \times 2mm$	9	5,330	47,970
Glass wool	Insulation	Pack	145	450	65,340
Steel pipe	Transporting fluid	Ø 3 1/3inch and 6m	121	350	36,000
Pan	Baking injera	Ø0.58x20mm	63	250	15,7500
Control valve	Flow control	Ø2/5 inch	126	150	18,900
Steel pipe	Transporting fluid	Ø2/5 inch and 6m length	11	250	2,750
Pump	To pump water from cold Water storage tank to receiver	pcs	1	16,000.00	16,000.00
RHS	Mitad leg	40mm×40mm and 6m length	63	2000	126,000
Others cost					63,000

Total costs for assembly and labour cost per mitad is 1120 ETB (Seid, 2021), and maintenance and operating cost per mitad are around 1000 ETB (YOHANES, 2020). Total starting cost is equal to the sum of the material and fabrication costs

$$= 570{,}770 + 70560 = \mathbf{641{,}330 ETB}$$

5.9.4 Solar tower injera baker economic benefit

Despite its expensive initial cost, it avoids the health risks associated with utilizing a biomass baking system, as well as the costs of wood and electricity. Conversely, the energy cost of the electric cooking stove was determined using the general electricity pricing of Ethiopian Electric Power Corporation (EEPCo), which is 2.124 birr per kWh.

Annual benefit is = (**112000*365*2.124+54*12) /56 = 1,550,531.57**$

In capital budgeting, the profitability of an investment is assessed using net present value, or NPV. NPV accounts for inflation and rate of return when comparing the worth of money received now with the same amount in the future. Three fundamental steps in discounted cash flow (DCF) methods form the basis of net present value (NPV).
The first step is to figure out each cash flow's present value, discounting it using the project's capital cost while accounting for all inflows and outflows. Secondly, total these cash flows; this is the project's net present value, or NPV. The last step is to decide whether or not to choose the project. If the project's net present value (NPV) is positive, it ought to be accepted; if not, it ought to be rejected. The following are the net present value, benefit cost ratio, and simple payback period:
Over the course of the project, the present cost is calculated as follows:

$$P_c = C_{inst} + A_c \left[\frac{((1+r)^n - 1)}{r(1+r)^n}\right]$$

Where C_{inst} = Totals installation cost $\mathbf{11,350,379.4}$\$ A_c= Annual cost = 228,132.58\$, r = discount rate = 9% n= life span of the

$$P_c = 1{,}350{,}379.4 + 228{,}132.58 \left[\frac{((1+0.09)^{25} - 1)}{0.09(1+0.09)^{25}}\right]$$

$$P_c = 13{,}591{,}231.64\$$$

The present value of benefit during the lifetime of the project is determined as:

$$P_b = A_b \left[\frac{((1+r)^n - 1)}{r(1+r)^n}\right]$$

Where A_b = Annual benefit = 1,550,531.57\$,

$$P_b = A_b \left[\frac{((1+r)^n - 1)}{r(1+r)^n}\right]$$

$$P_b = 1{,}550{,}531.57\left[\frac{((1+0.09)^{25}-1)}{0.09(1+0.09)^{25}}\right]$$

$$P_b = 15{,}230{,}219.79\$$$

Net present value is determined as NPV = $P_b - P_c = \mathbf{1,638,988.15}\$$

Annual saving $A_s = A_b - A_c = \mathbf{1,322,399}\$$

Payback period: When system benefits equal system expenses, a period of time known as the payback period—also called the break-even point—appears. is determined as:

$$\text{PBP} = \frac{C_{inst}}{A_s} \approx \mathbf{8.6\ year}$$

Benefit-Cost Ratio (BCR) is the system's present value of benefits divided by its present value of costs.

$$\text{BCR} = \frac{\text{Present worth of benefit}}{\text{Present worth of cost}} = \frac{15{,}230{,}219.79}{13{,}591{,}231.64} = 1.12$$

CHAPTER SIX

RESULTS AND DISCUSIONS

The findings and analysis from the thesis research are presented in this chapter. Important subjects addressed include: Using Soltrace and SAM software to analyze receiver efficiency, optical efficiency, project cost, and receiver output temperature; choosing tower height and field layout. Additionally, utilizing Python code transient analysis of mitad has been done.

6.1 Simulation of solar field

6.1.1 Selection of Tower Height

The selection of tower height and layout for a solar power tower system is a critical decision that can have a significant impact on the overall performance of the system.

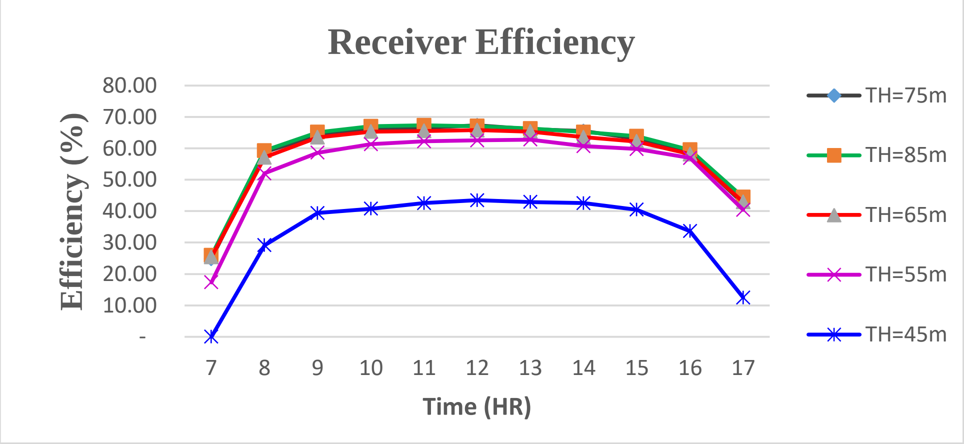

Figure 6. 1: Hourly Receiver efficiency for different tower height

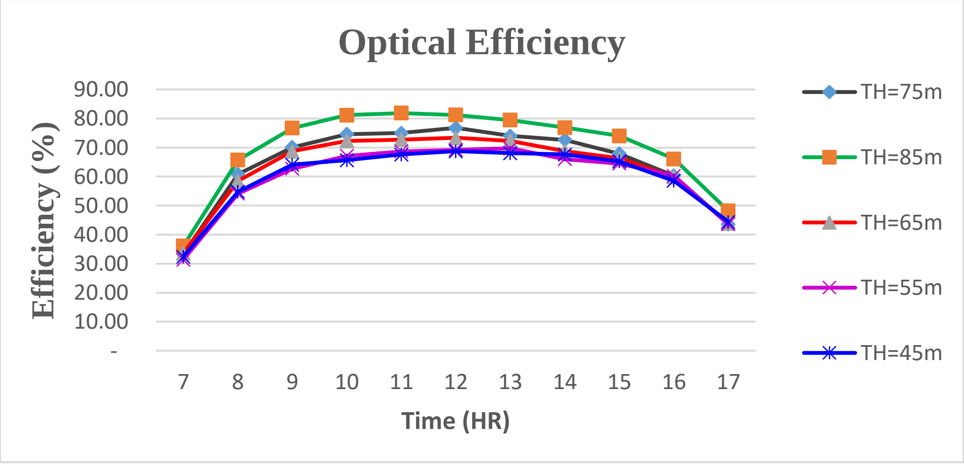

Figure 6. 2: Hourly optical efficiency for different tower height

Figure 6. 1 and Figure 6. 2 shows the optical, and receiver efficiency of a solar power tower system at different tower heights for month of November. The graph shows that as the tower height increase optical efficiency and receiver efficiency increase. This is because a taller tower reduces losses due to scattering and reflection. However, the heliostats nearest to the tower may prevent reflected sunlight from reaching the receiver when the tower is shorter. This is because the beams intersect with the tower structure or other heliostat mirrors before they reach the target since the angle between the heliostat, the receiver, and the sun grows shallower.

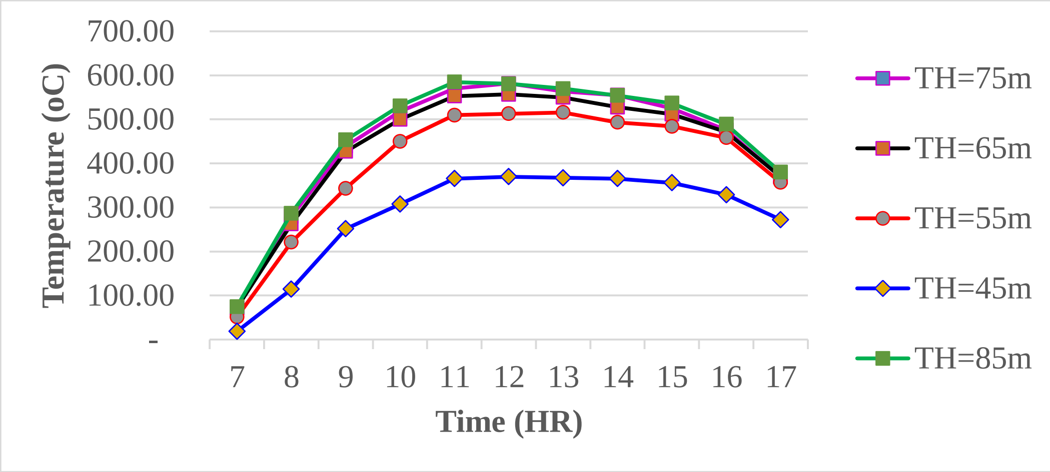

Figure 6. 3: Hourly Receiver Outlet Temperature for different tower height

Figure6. 3 show the receiver outlet temperature versus time of day at different tower heights, from 45 meters to 85 meters for month of November. The graph shows that the receiver outlet temperature is generally higher at higher tower heights. For example, at midday, the receiver outlet temperature for 85meter tower height is about 580.83 degrees Celsius, while the receiver outlet temperature at 45 meters is about 369.96 degrees Celsius.

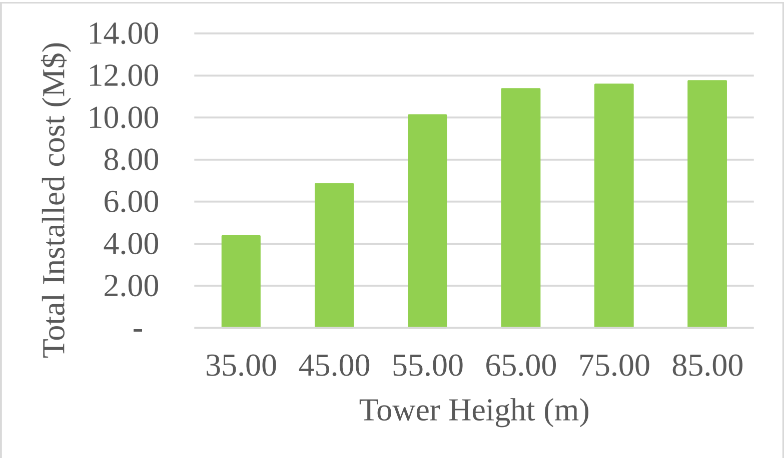

Figure 6. 4: Tower Cost vs Tower Height

According to the graph, the tower height and tower cost are positively correlated. This implies that as a tower's height increases, so does the tower's cost. Moreover, taller towers are more susceptible to wind loads, which can increase structural requirements, more complicated engineering and maintenance costs. However, taller towers offer the advantage of potentially higher efficiency, shorter towers, on the other hand, are:

- Cheaper to build and maintain.
- Less susceptible to overheating and wind loads.

However, they also have lower concentration ratios and suffer from higher spillage losses, leading to reduced efficiency compared to taller towers.

6.1.2 Field layout

The solar field design is simulated using Solar Pilot software. The simulation findings show that in order to obtain the necessary total reflecting area (AT) of 39,886 square meters for the heliostats, a total of 2635 individual heliostats are needed. The following figures provide more information about the chosen radial stagger design for the heliostat field.

	Units	Value	Mean	Minimum	Maximum	Std. dev
Total plant cost	$	7696351				
Simulated heliostat area	m^2	39886				
Simulated heliostat count	-	2570				
Power incident on field	kW	39886				
Power absorbed by the receiver	kW	29261				
Power absorbed by HTF	kW	19267				
Cloudiness efficiency	%	100.00				
Shadowing and Cosine efficiency	%	89.19				
Reflection efficiency	%	87.57				
Blocking efficiency	%	99.53				
Image intercept efficiency	%	100.00				
Absorption efficiency	%	94.37				
Solar field optical efficiency	%	77.74				
Optical efficiency incl. receiver	%	73.36				
Incident flux	kW/m2	99.696	0.000	965.105	208.641	
No. rays traced	-	46763				
No. heliostat ray intersections	-	10000				
No. receiver ray intersections	-	8716				

a. Flux simulation results summary (SolTrace Simulation)

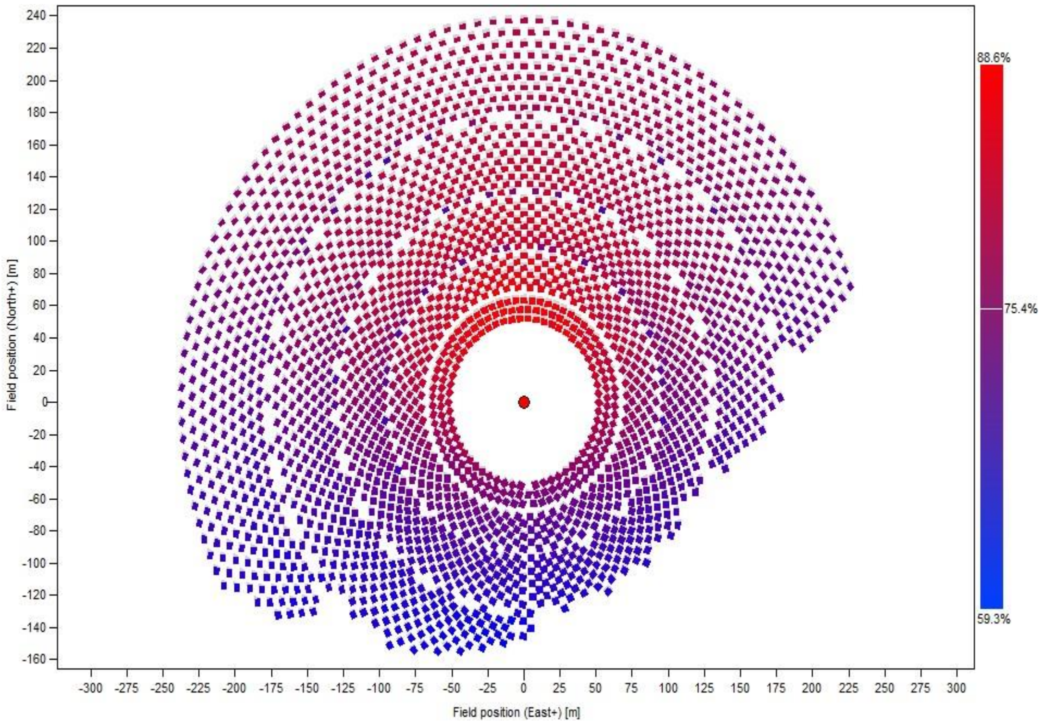

I) At solar noon

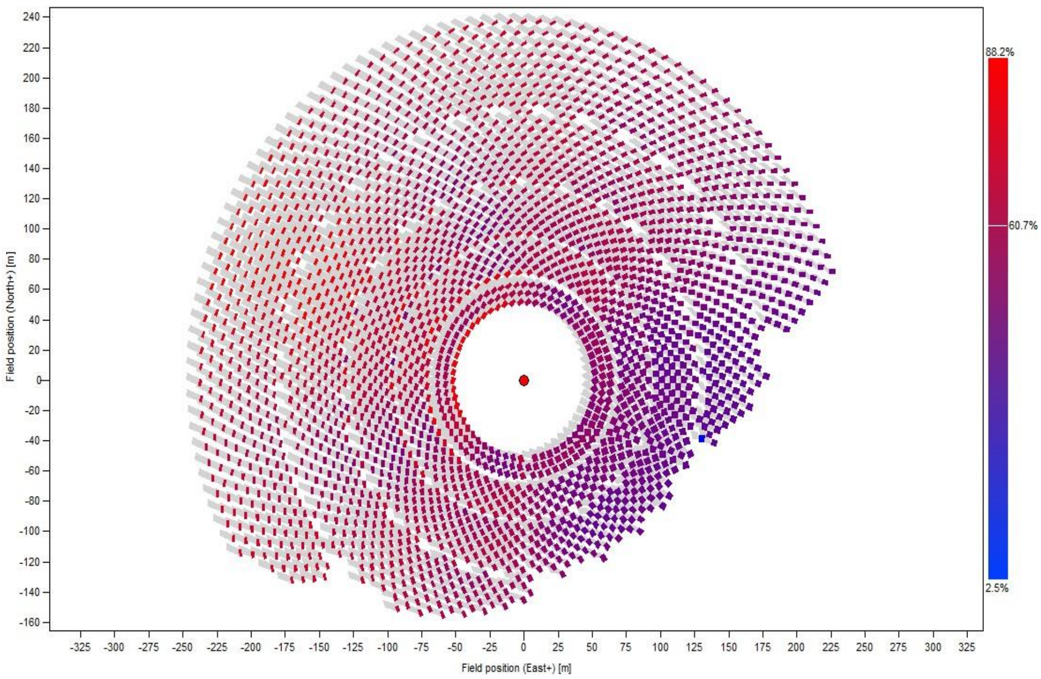

II) Morning at 2:00 hour

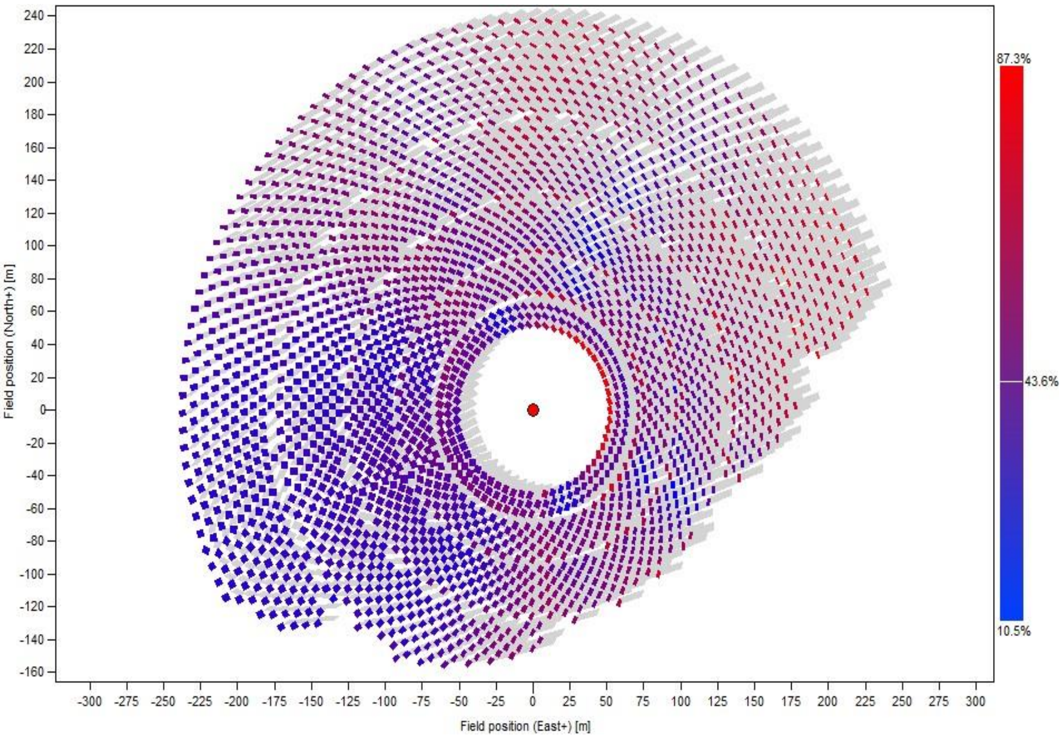

III) Afternoon at 10: hour

b. Layout based on total efficiency

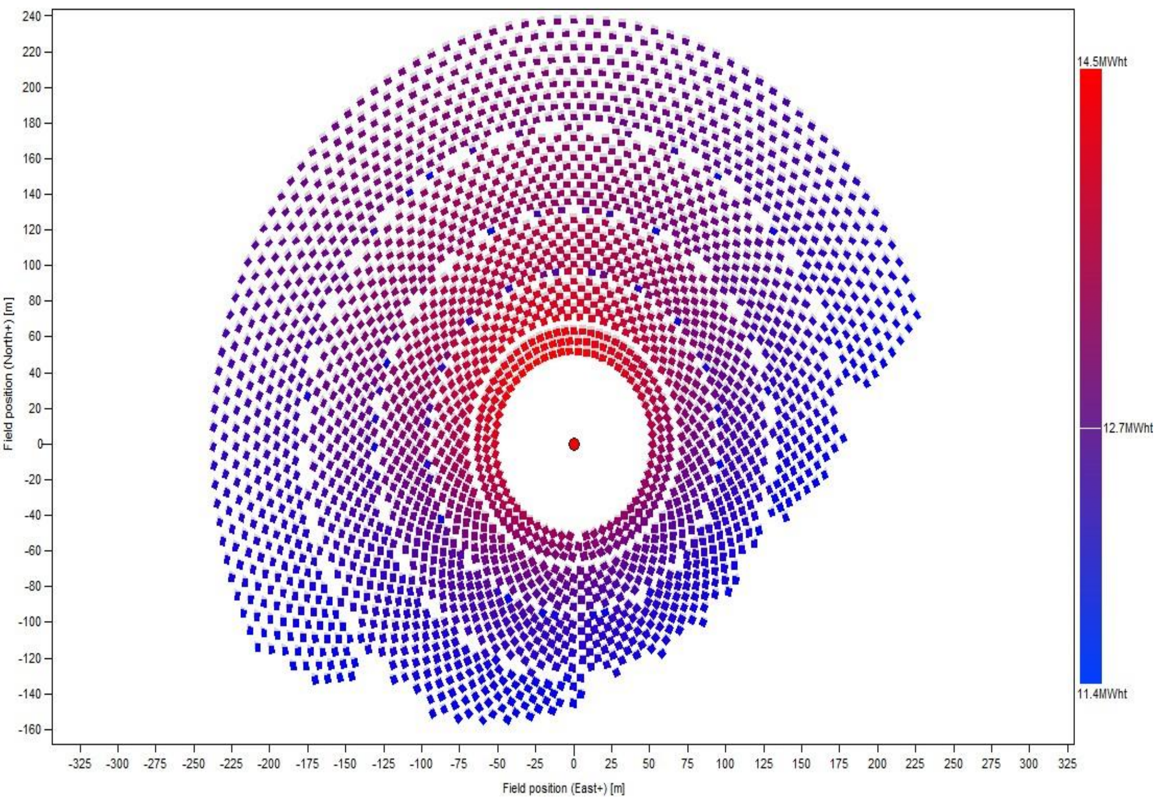

c. Layout based on annual energy

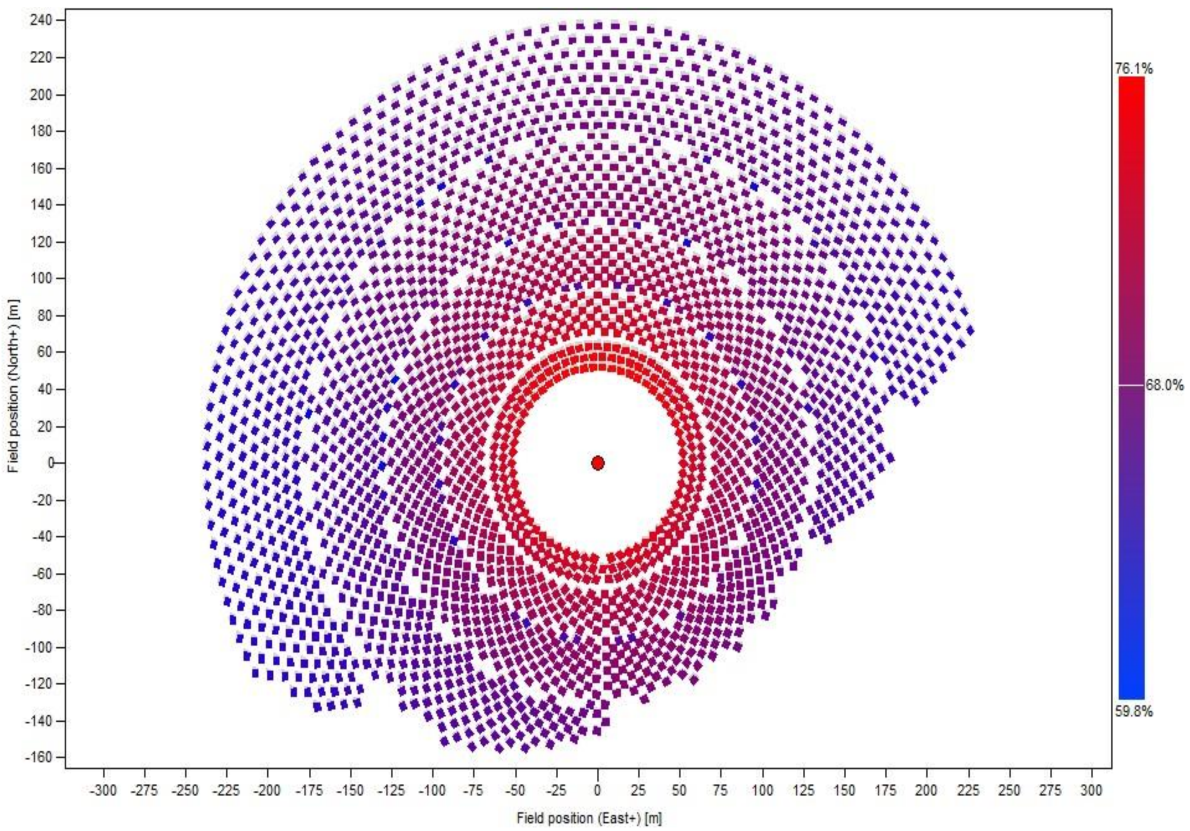

d. Layout based on annual efficiency

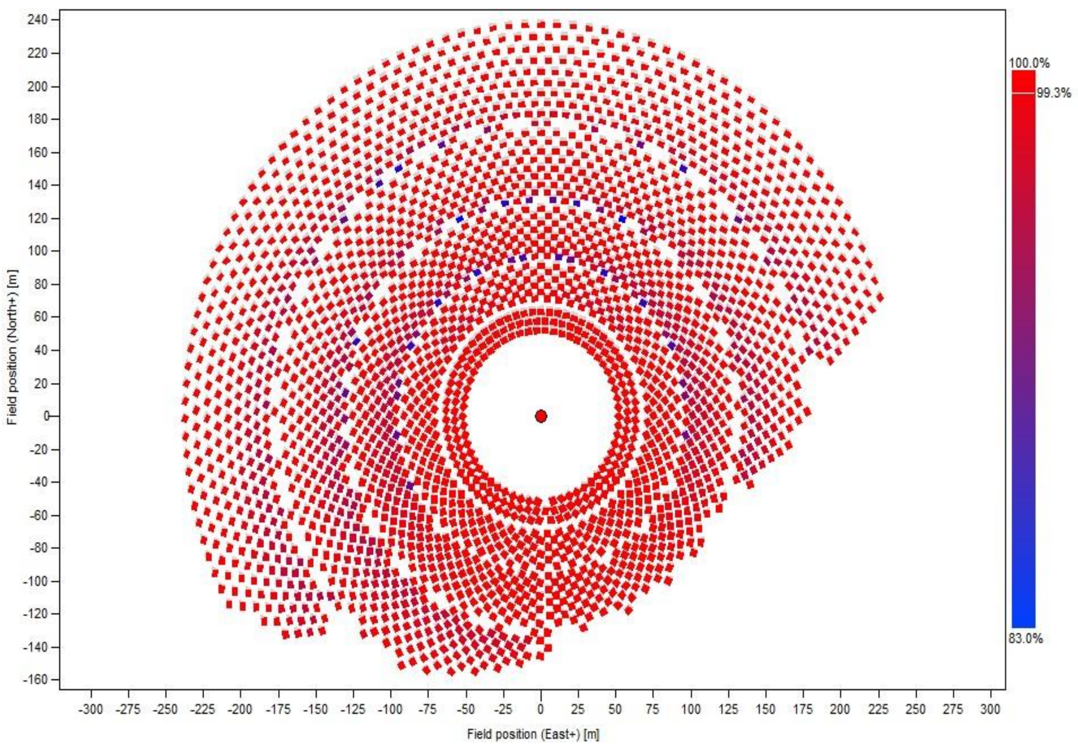

e. Layout based on blocking efficiency

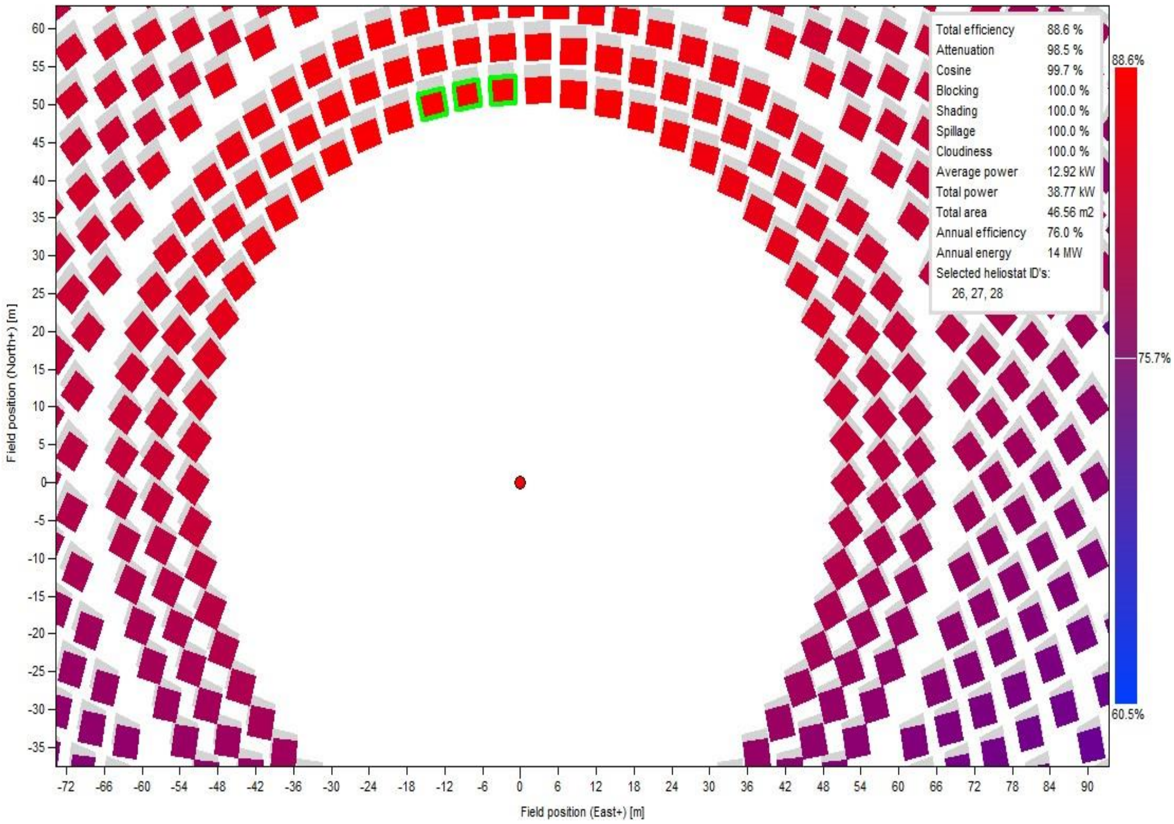

f. The graphical interface of the selected heliostat in the solar field.

Figure 6. 5: Solar field layouts for 65m tower height.

Figure 6.5 shows the heliostat layout of the solar field at tower heights 65 meter. In the Northern Hemisphere, the sun will be in the southern sky for a longer period of time every year. To maximize the amount of sunlight it gets, a south-facing solar collector will be pointed directly towards the sun for a greater portion of the day, which results in:

- Greater energy production
- Improved overall efficiency

6.2Receiver Flux Intensity

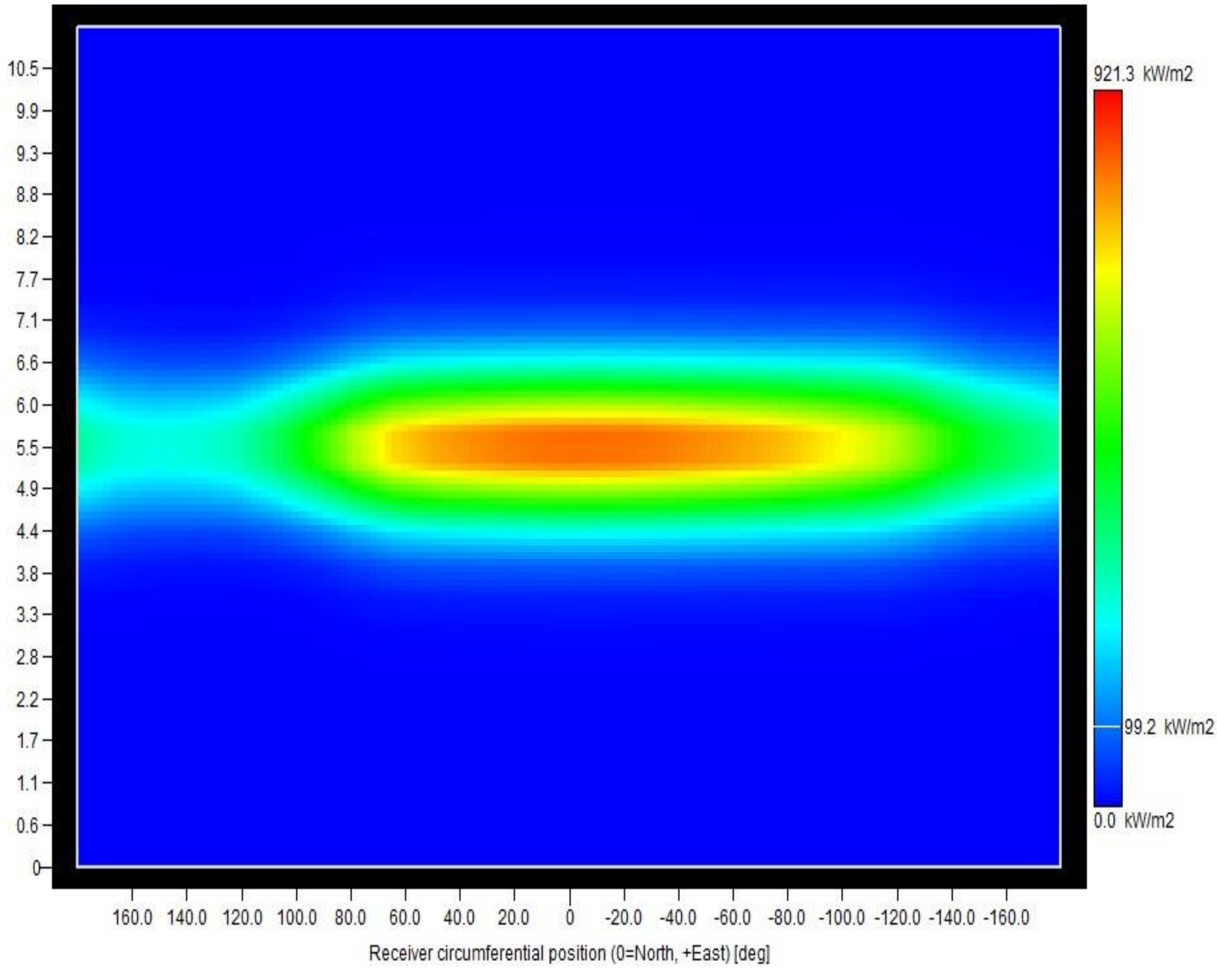

Figure 6. 6: Flux intensity

The graph, which is most likely the result of a Solar Pilot analysis, displays the flux intensity distribution on a central receiver. With 0° representing north, positive values pointing counter-clockwise towards the east, and negative values pointing clockwise towards the west, the y-axis depicts the receiver's height, and the x-axis its circumferential position. The concentration ratio varies across the receiver surface, with the highest concentration occurring at the center and lower concentration towards the edges. This is because the reflected sunlight is focused onto a smaller area at the center.

The flux intensity is displayed on the color map, with the red areas of the graph correspond to the areas of the field where the flux intensity is highest, and the blue areas of the graph correspond to the areas of the field where the flux intensity is lowest.

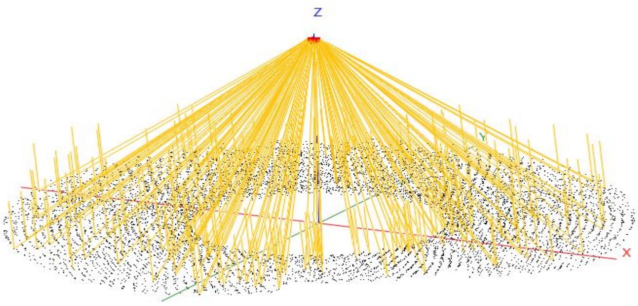

Figure 6. 7: Receiver and ray intersection

Figure6. 7 display where the receiver and the sun's rays intersect. The ray tracing simulation helps visualize how the heliostats reflect sunlight and concentrate it onto the receiver throughout the day. This can guarantee that the receiver gets the most sunlight possible and help to optimize the heliostat field's design. The vertical axis in the image represents the height of the tower, while the horizontal axis represents the position of the heliostats relative to the tower.

6.3 Analysis of useful energy and useful exergy

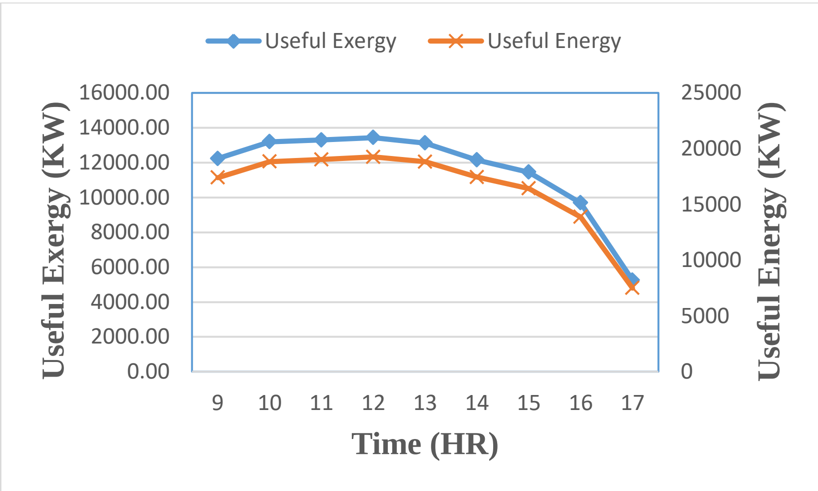

Figure 6. 8: Variation of collected useful energy and exergy with respect to time

Useful energy peaks around solar noon which is 19.267MW when solar irradiation is strongest. This makes sense as solar collector would collect the most energy when the sun is at its highest point. Useful exergy follows a similar curve, peaking at around 13.443MW at solar noon. At 9 am, useful energy is around 17.407MW and Useful exergy around 12.233MW.

6.4Estimation of convective heat loss

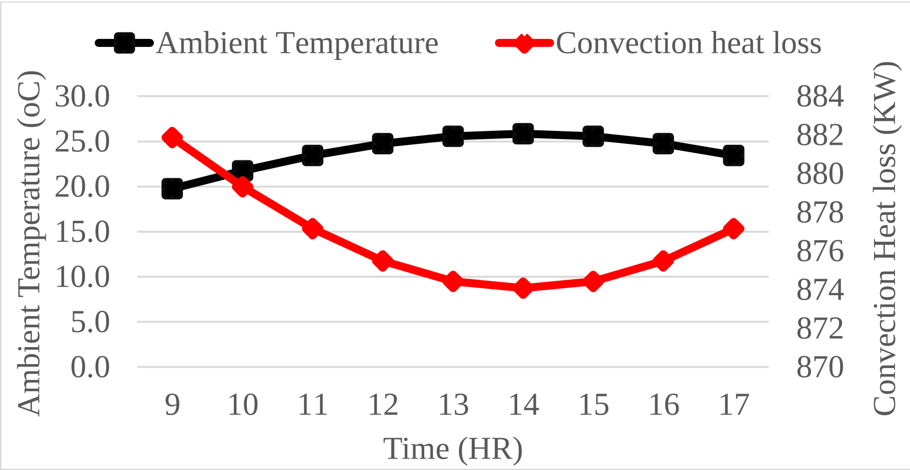

Figure 6. 9: Estimation of hourly variation of convective heat loss

The graph show that convective heat loss peaks around 9-10pm at over 880KW and the ambient temperature is lowest in the morning around 9 am at around 19.8 K. As ambient temperature increases towards the afternoon, convective heat loss decreases. So, convective heat loss is highest when ambient temperature is lower in the morning. As air warms later in the day, convection decreases. This makes sense physically since convection is heat transfer due to temperature differences.

Receiver and Optical Efficiency

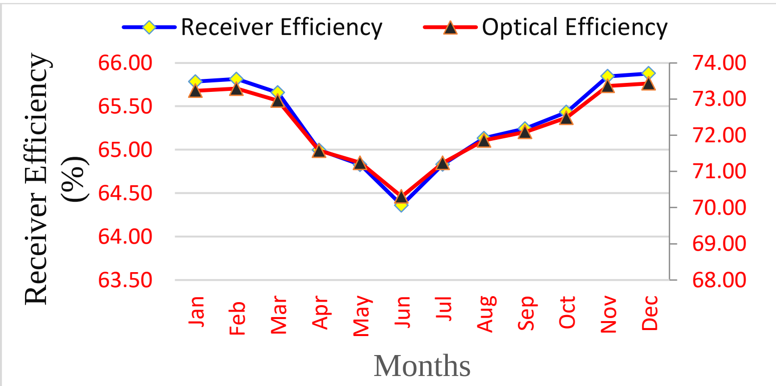

Figure 6. 10: Monthly receiver and optical efficiency

The graph shows the receiver and optical efficiency of a solar collector throughout the year at on average days of the months at solar noon.

The graph also shows that the optical and receiver efficiencies are at their best points during the winter, when the sun is at its highest point in the sky. Efficiency is lowest in the summer when the sun is lower in the sky. This is a result of the sun's rays changing angles throughout the year; the collector cannot capture as much sunlight when the sun is at a lower angle.

Receiver Outlet Temperature over the year

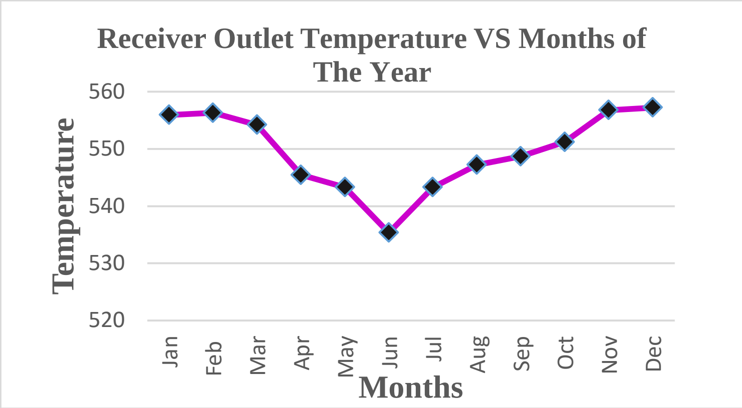

Figure 6. 11: Average monthly receiver outlet temperature

The graph shows that the average receiver outlet temperature is highest in the winter months, at around 556 degrees Celsius. The temperature then drops gradually in the fall and summer months, reaching its lowest point in June at around 535 degrees Celsius.

There are a few reasons why the receiver outlet temperature is higher in the winter months. First, the sun is higher in the sky during the winter. Second, the days are longer in the winter, which means that the collector has more time to heat up.

6.5 Transient Analysis of Mitad

6.5.1 Variation of Temperature of Mitad with its Thickness

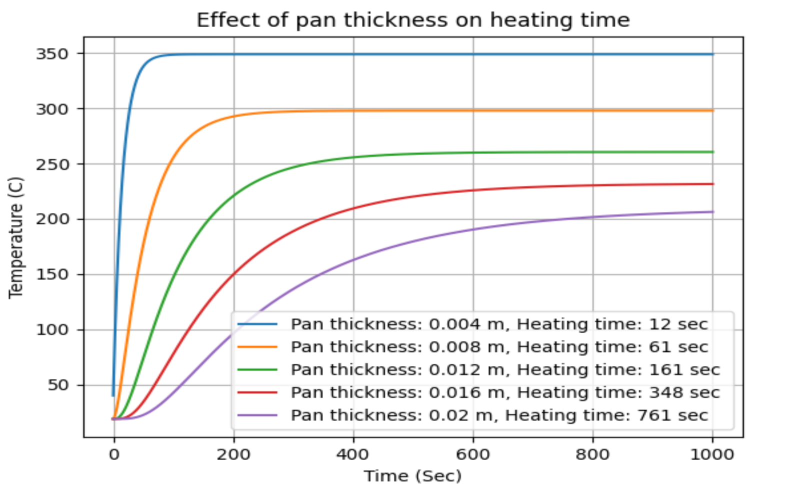

Figure 6. 12: Heat up time versus temperature at different thickness of the pan

Figure6. 12 shows the surface temperature of different thickness baking pan heated from below, plotted against time. Compared to thinner pans, thicker pans require a longer

heating time because they contain a bigger volume of material that heat must travel through.

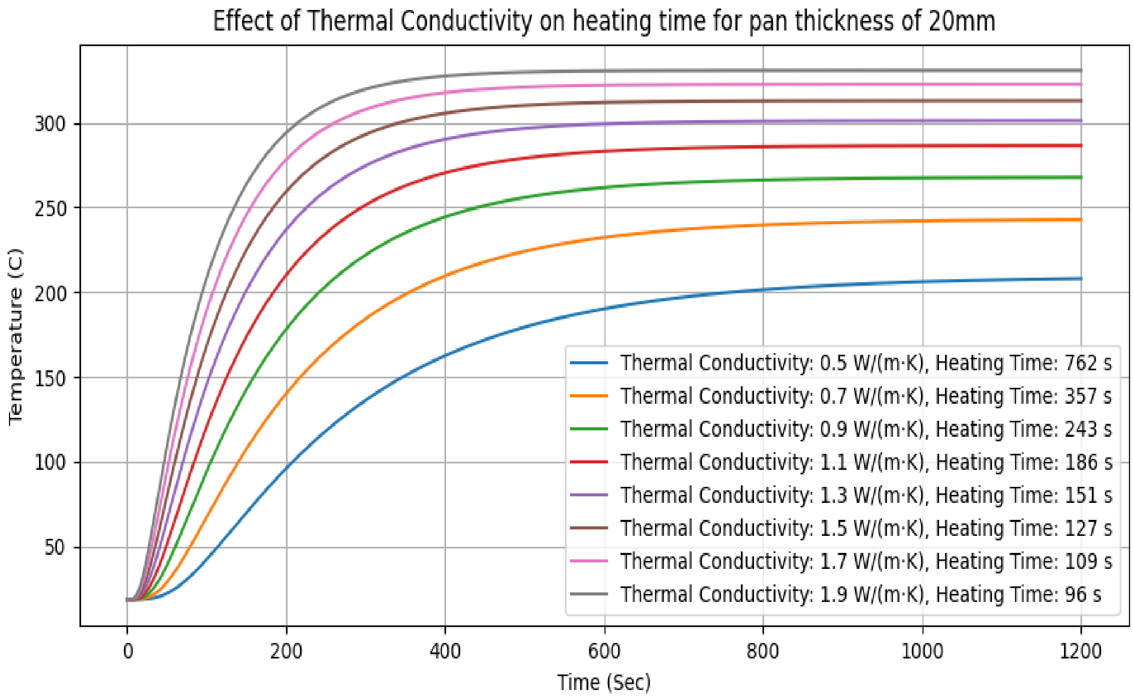

Figure 6. 13: Heat up time versus temperature at different thermal conductivity

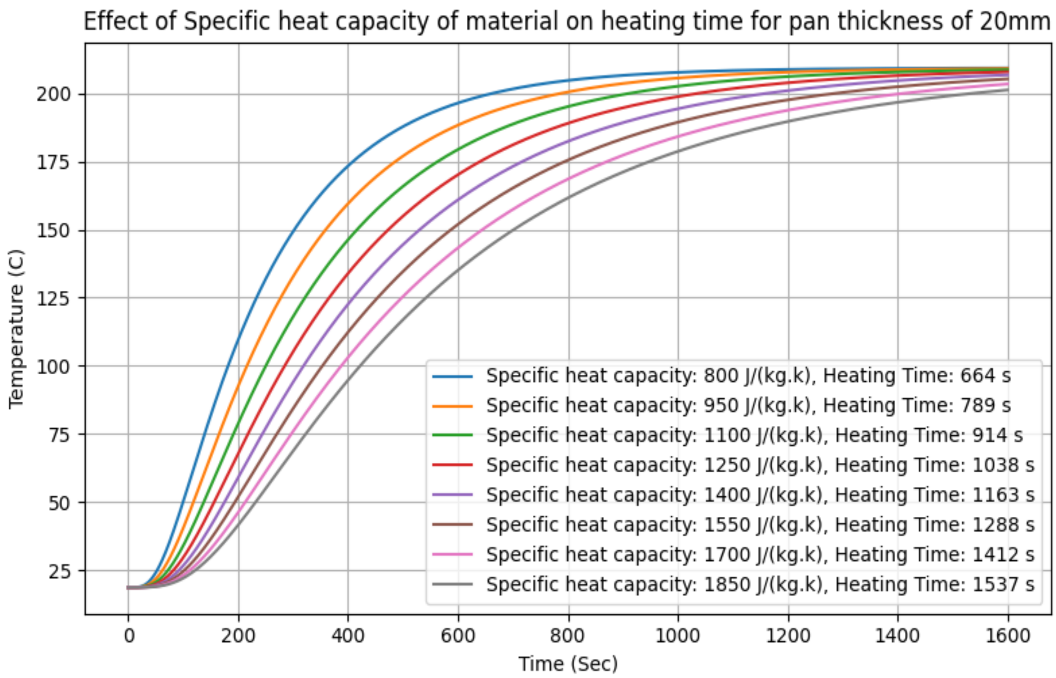

Figure 6. 14 : Effect of specific heat capacity on heating time

When comparing the specific heat capacity of pans, the pan with the larger specific heat capacity will need more heat energy to raise its temperature. The pan with the larger specific heat capacity will therefore require more time to attain the same temperature as the pan with the lower specific heat capacity.

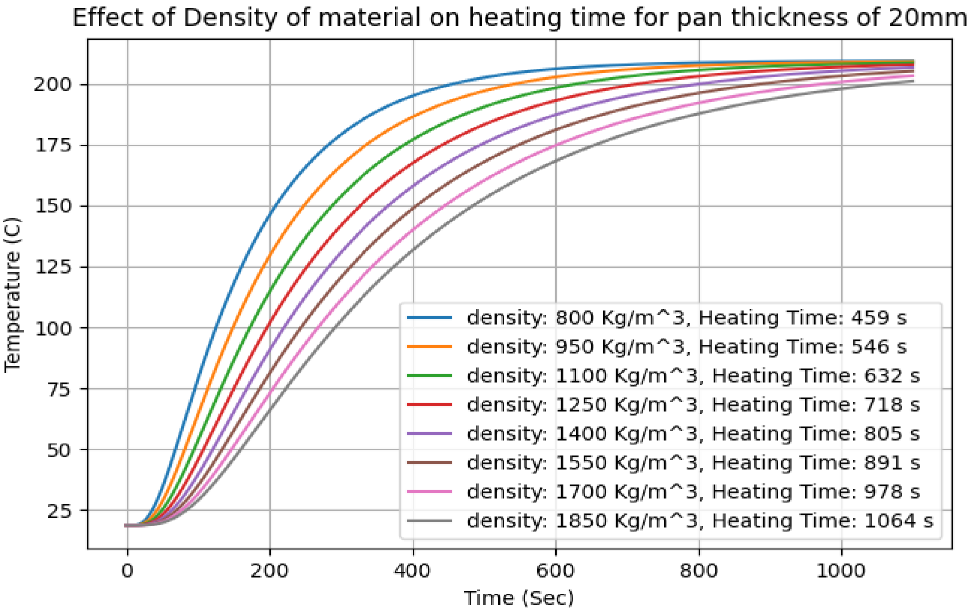

Figure 6. 15 : Effect of density of material on heating time

In comparison to less dense materials, denser materials require more heating time to reach a given temperature. A denser material will need more energy to raise its temperature by the same amount since it has a larger mass for the same volume.

6.5.2 Surface Temperature of the mitad

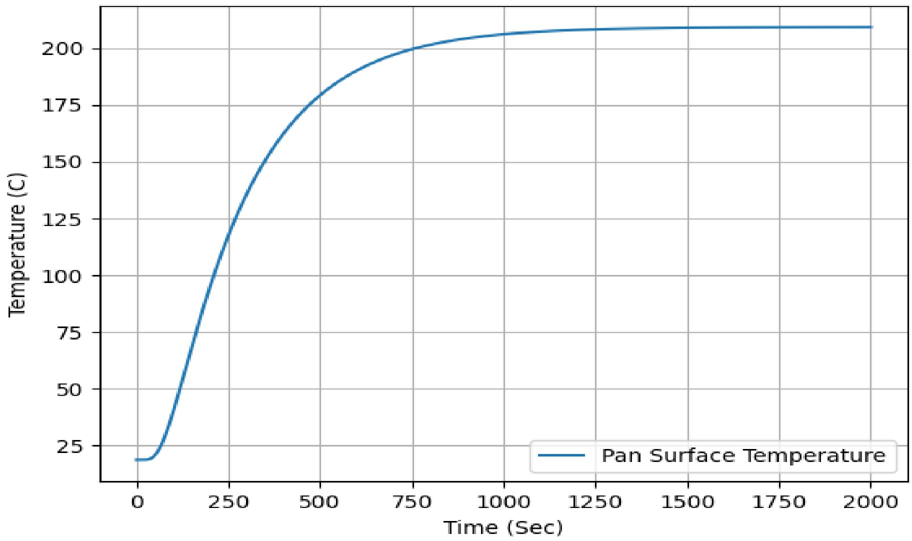

Figure 6. 16: Heating up time

The graph shows a steep curve that rapidly increases as the pre-heating time increases. However, the rate of increase slows down as the temperature approaches the average baking temperature. The curve reaches a temperature close to 200°C within the 12.5 minutes of pre-heating.

6.5.3 Injera Baking Time

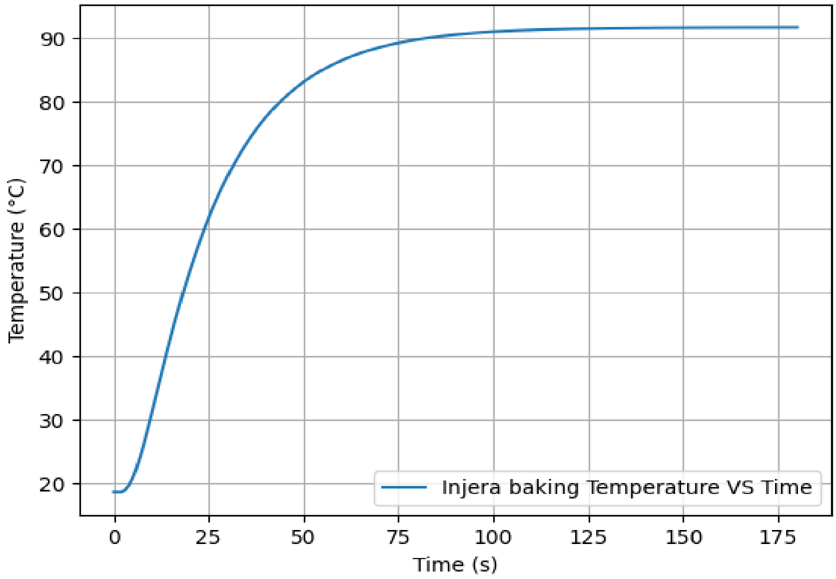

Figure 6. 17: Baking time

It shows the baking time for injera at average baking temperature on the mitad. Temperature of the dough increase steadily at the beginning: however, the rate of increase slows down as the temperature approaches the boiling point of water (92.62°C). The curve reaches a temperature close to 92.62°C within the first 2-3 minutes of baking.

6.5.4 Mitad Re-heat Time

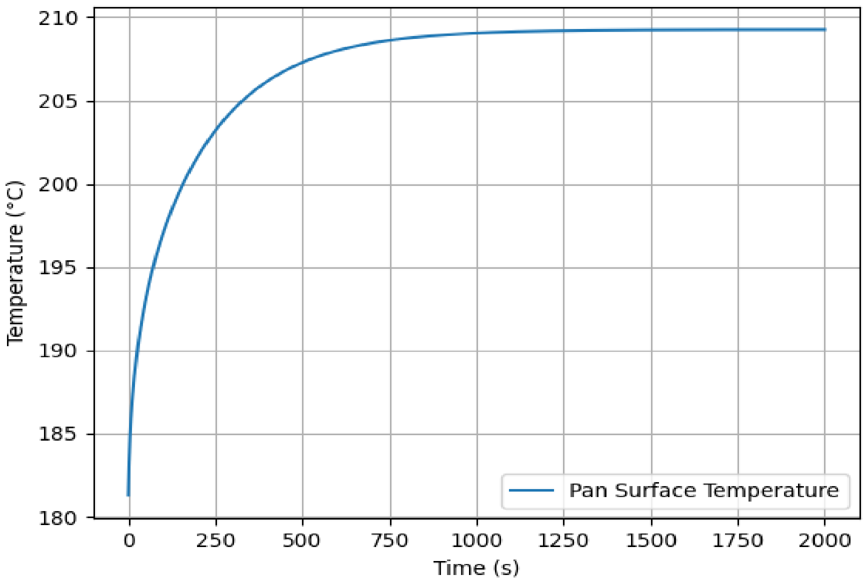

Figure 6. 18: Mitad re-heating time

The graph shows the reheating time of a mitad between consecutive injera baking. The result indicates that, mitad reaches a temperature of about 200 degrees Celsius after about 150 seconds. This is the surface temperature of mitad at which injera is typically cooked. The graph also shows that a mitad would be reheated to baking temperature within 2-3 minutes between consecutive injera baking sessions.

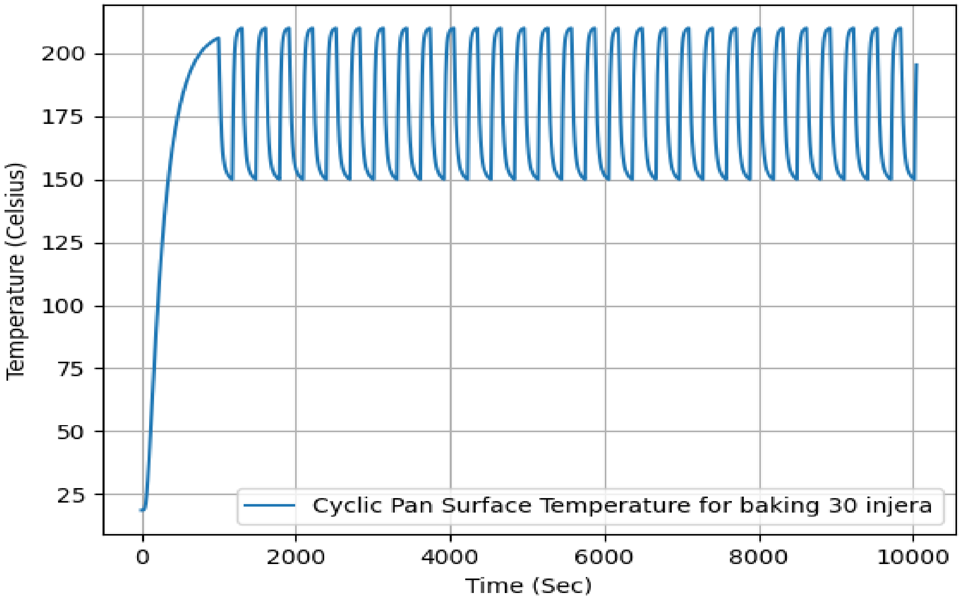

Figure 6. 19: Cyclic Baking of Injera

The descending slopes stand in for the pan's cooling process during the injera-baking process. The injera will immediately warm up as a result of contact with the hot surface once the batter is placed onto the heated pan. The increasing slopes most likely indicate the time spent warming pan in between baking. Therefore, the temperature of the mitad decreases after one injera is cooked and taken out of it. The heat source is required to raise the pan temperature back to the appropriate temperature in order to guarantee a constant cooking temperature for the subsequent injera.

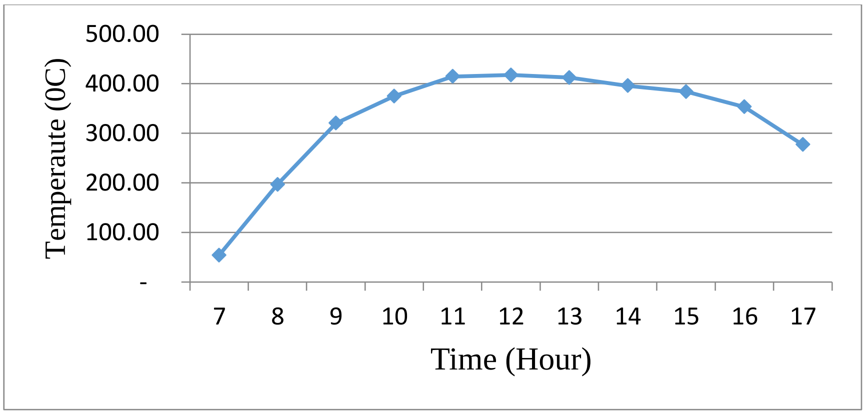

Figure 6. 20: Temperature of HTF under the pan

CHAPTER SEVER

CONCLUSIONS AND RECOMMENDATIONS

7.1 Conclusion

The present work involved numerically modeling the performance of a solar power tower and baking system for mass injera baking applications. Specifically, the solar tower system was modeled using soltrace and SAM software to simulate factors such as heliostat field layout, receiver efficiency, optical efficiency, Economic analysis, and receiver outlet temperatures. Additionally, Python coding modeled transient heat transfer in the injera baking process on traditional mitad pans. Here are some potential conclusions that could be drawn from this study:

- Optimal solar tower height was determined to be 55-75 meters when balancing performance, cost, and operational factors like wind loads and overheating risks.
- Collected useful energy and exergy follow expected trends, peaking at solar noon, which is useful energy is around 19.267MW and Useful exergy around 13.443MW. This validates proper modeling of the system's energy flows.
- Receiver and optical efficiencies peak in the winter months when solar intensity is highest, and decline in the summer as expected.
- Average receiver outlet temperature is highest in the winter months, at around 556 degrees Celsius. The temperature then drops gradually in the fall and summer months, reaching its lowest point in June at around 535 degrees Celsius.
- Thicker mitad pans take longer time to heat up. After sufficient time, temperatures equalize through the thickness at around 210°C in this case. Thinner pans would heat faster.
- During heating up, mitad temperature rises steeply, approaching 200°C within 12.5 minutes. The rate slows as temperature nears typical baking levels.
- Single injera baking is completed within 2-3 minutes at typical mitad surface temperatures around 200°C.
- Between batches, the mitad reheats to 200°C in about 2.5 minutes. This represents the optimal idle time before pouring the next injera.

- The project is financially feasible since it has a positive net present value, a benefit-cost ratio greater than one. Additionally, within eight years and 10 months, the project pays for its original investment.

7.2 Recommendation

The following future improvements are necessary for this work:

- To reduce the heating time in the traditional clay mitad used for the injera baking system, a practical solution is using small thickness mitad and substitutes it with a highly conductive material like pure copper. By implementing this change, the system can achieve faster and more efficient heating, resulting in improved overall performance and increased productivity.
- To achieve significant cost and size reduction in solar tower systems, it is beneficial to introduce nano fluids into the heat transfer fluid (HTF). This approach enhances thermal conductivity and improves the efficiency of heat transfer.
- This study shows that it is technically feasible; however the inability to conduct experiments impedes the practical application of the findings. To fully realize the promise of solar injera baking, future research should prioritize addressing these limitations through an experimental study.

REFERENCES

Abdulkadir, Amibe, H., Demiss A, & Nydal, O. J. (2011). Performance investigation of solar powered Injera Baking oven for indoor cooking. ISES solar world congress proceedings, Kassel, Germany,

Abolhosseini, S., Heshmati, A., & Altmann, J. (2014). A review of renewable energy supply and energy efficiency technologies.

Adem, K. D., & Ambie, D. A. (2017). A review of injera baking technologies in Ethiopia: Challenges and gaps. *Energy for Sustainable Development*, *41*, 69-80. https://doi.org/https://doi.org/10.1016/j.esd.2017.08.003

Aicher, T., & Martin, H. (1997). New correlations for mixed turbulent natural and forced convection heat transfer in vertical tubes. *International journal of heat and mass transfer*, *40*(15), 3617-3626.

Albarbar, A., & Arar, A. (2019). Performance assessment and improvement of central receivers used for solar thermal plants. *Energies*, *12*(16), 3079.

Alemu, G. (2020). *Investigation of Heat Transfer Engine Oil in Solar Powered Injera Baking Oven Using Cuo Particle Nano Fluid*

Ambaw, G. (2015). *Performance analysis and reliablity testing of a ceramic bake ware for an electric injera baking stove* Master Thesis Addis abeba university].

Aramesh, M., Ghalebani, M., Kasaeian, A., Zamani, H., Lorenzini, G., Mahian, O., & Wongwises, S. (2019). A review of recent advances in solar cooking technology. *Renewable Energy*, *140*, 419-435. https://doi.org/https://doi.org/10.1016/j.renene.2019.03.021

Asfafaw, H. T., Kahsay, M. B., & Nydal, O. J. (2019). Numerical and experimental analysis of solar Injera baking with a PCM heat storage. *Momona Ethiopian Journal of Science*, *11*(1), 1-13. https://doi.org/https://doi.org/10.4314/mejs.v11i1.1

Asfafaw, T. H., Nydal, O. J., & Kahsay, M. B. (2014). Energy storage integrated solar stove: A case of solar Injera baking in Ethiopia. IEEE Global Humanitarian Technology Conference (GHTC 2014),

Atif, M., & Al-Sulaiman, F. A. (2017). Energy and exergy analyses of solar tower power plant driven supercritical carbon dioxide recompression cycles for six different locations. *Renewable and Sustainable Energy Reviews*, *68*, 153-167.

Atif, M., & Al-Sulaiman, F. A. (2018). Energy and exergy analyses of recompression Brayton cycles integrated with a solar power tower through a two-tank thermal storage system. *Journal of Energy Engineering*, *144*(4), 04018036. https://doi.org/https://doi.org/10.1061/(ASCE)EY.1943-7897.0000545

Atif, M., & Al-Sulaiman, F. A. (2015). Development of a mathematical model for optimizing a heliostat field layout using differential evolution method. *International Journal of Energy Research*, *39*(9), 1241-1255. https://doi.org/https://doi.org/10.1002/er.3325

Augsburger, G. (2013). *Thermo-economic optimisation of large solar tower power plants*.

Barone, G., Buonomano, A., Forzano, C., & Palombo, A. (2019). Solar thermal collectors. In *Solar hydrogen production* (pp. 151-178). Elsevier. https://doi.org/https://doi.org/10.1016/B978-0-12-814853-2.00006-0

Bellos, E., Tzivanidis, C., & Belessiotis, V. (2017). Daily performance of parabolic trough solar collectors. *Solar Energy*, *158*, 663-678. https://doi.org/https://doi.org/10.1016/j.solener.2017.10.038

Bergman, T. L. (2011). *Fundamentals of heat and mass transfer*. John Wiley & Sons.

Berhanu, H., Bekele, A., Venkatachalam, C., & Sivalingam, S. (2022). Performance improvement of an electric injera baking pan (Mitad) using copper powder as additive material. *Energy for Sustainable Development*, *68*, 242-257.

Bhave, A. G., & Kale, C. K. (2020). Development of a thermal storage type solar cooker for high temperature cooking using solar salt. *Solar Energy Materials and Solar Cells*, *208*, 110394. https://doi.org/https://doi.org/10.1016/j.solmat.2020.110394

Blampain, E. (2018). Development of an integrated tool to design, estimate cost and calculate annual performances of a solar power tower. In.

Bonsa, R. (2020). *Investigating the Performance of Parabolic Trough Solar Collector with Thermal Energy Storage System for Injera Baking Applications* ASTU].

Boukelia, T., Bouraoui, A., Laouafi, A., Djimli, S., & Kabar, Y. (2020). 3E (Energy-Exergy-Economic) comparative study of integrating wet and dry cooling systems in solar tower power plants. *Energy*, *200*, 117567. https://doi.org/https://doi.org/10.1016/j.energy.2020.117567

Chu, Y., & Meisen, P. (2011). Review and comparison of different solar energy technologies. *Global Energy Network Institute (GENI), San Diego, CA*, *1*, 1-52.

Collado, F. J. (2008). Quick evaluation of the annual heliostat field efficiency. *Solar Energy*, *82*(4), 379-384.

Collado, F. J., & Guallar, J. (2013). A review of optimized design layouts for solar power tower plants with campo code. *Renewable and Sustainable Energy Reviews*, *20*, 142-154.

De Meyer, O., Dinter, F., & Govender, S. (2016). Thermal resistance model for CSP central receivers. AIP Conference Proceedings,

Deshmukh, G., Birwal, P., Datir, R., & Patel, S. (2017). Thermal insulation materials: A tool for energy conservation. *Journal of Food Processing & Technology*, *8*(04), 1-5. https://doi.org/0.4172/2157-7110.1000670

Duffie, J. A., & Beckman, W. A. (2013). *Solar engineering of thermal processes*. John Wiley & Sons.

Eddhibi, F., Amara, M. B., Balghouthi, M., & Guizani, A. (2015). Optical study of solar tower power plants. Journal of Physics: Conference Series,

Ewert, M., & Fuentes, O. N. (2015). Modelling and simulation of a solar tower power plant. *Journal article. Available: http://scholar. google. co. za. ezproxy. ukzn. ac. za*, *2048*.

Farinu, A. (2006). *Heat and mass transfer analogy under turbulent conditions of frying*

Farooqui, S. Z. (2014). A review of vacuum tube based solar cookers with the experimental determination of energy and exergy efficiencies of a single vacuum tube based prototype. *Renewable and Sustainable Energy Reviews*, *31*, 439-445. https://doi.org/https://doi.org/10.1016/j.rser.2013.12.010

Faye, K., Thiam, A., & Faye, M. (2021). Optimum height and tilt angle of the solar receiver for a 30 KWE solar tower power plant for the electricity production in the Sahelian Zone. *International Journal of Photoenergy*, *2021*, 1-14.

Group, W. B. (2013). *Global financial development report 2014: Financial inclusion* (Vol. 2). World Bank Publications.

Guangul, F. M., & Chala, G. T. (2019). Solar energy as renewable energy source: SWOT analysis. 2019 4th MEC international conference on big data and smart city (ICBDSC),

Hailu, M. H., Kahsay, M. B., Tesfay, A. H., & Dawud, O. I. (2017). Energy consumption performance analysis of electrical mitad at mekelle city. *Momona Ethiopian Journal of Science*, *9*(1), 43-65. https://doi.org/https://doi.org/10.4314/mejs.v9i1.4

Hailu, M. H., Nydal, O. J., Kahsay, M. B., & Tesfay, A. H. (2017). A direct solar fryer for injera baking application. Proceedings of ISES Solar World Congress,

Hassan, A. (2016). Solar tower power plant optimization: a review. *Ondokuz Mayis University*. https://doi.org/ 10.13140/RG.2.2.13416.78088

Herez, A., Ramadan, M., & Khaled, M. (2018). Review on solar cooker systems: Economic and environmental study for different Lebanese scenarios. *Renewable and Sustainable Energy Reviews*, *81*, 421-432. https://doi.org/https://doi.org/10.1016/j.rser.2017.08.021

Hosseinzadeh, M., Sadeghirad, R., Zamani, H., Kianifar, A., & Mirzababaee, S. M. (2021). The performance improvement of an indirect solar cooker using multi-walled carbon nanotube-oil nano fluid: An experimental study with thermodynamic analysis. *Renewable Energy*, *165*, 14-24. https://doi.org/https://doi.org/10.1016/j.renene.2020.10.078

Indora, S., & Kandpal, T. C. (2018). Institutional cooking with solar energy: A review. *Renewable and Sustainable Energy Reviews*, *84*, 131-154. https://doi.org/https://doi.org/10.1016/j.rser.2017.12.001

Jemal, T., Fatoba, O., Shimels, S., & Tegenaw, Y. (2022). Design and experimental Analyses of enhanced heat transfer performance in solar powered Injera baking pan using Cu/Oil and A12O2/Oil nano fluids. *Materials Today: Proceedings*. https://doi.org/https://doi.org/10.1016/j.matpr.2022.02.382

Jun, S., & Irudayaraj, J. M. (2008). *Food processing operations modeling: design and analysis* (Vol. 107). CRC press.

Kaletunç, G. (2007). Prediction of specific heat of cereal flours: A quantitative empirical correlation. *Journal of food engineering*, *82*(4), 589-594. https://doi.org/https://doi.org/10.1016/j.jfoodeng.2007.03.028

Kalogirou, S. (2003). The potential of solar industrial process heat applications. *Applied Energy*, *76*(4), 337-361. https://doi.org/https://doi.org/10.1016/S0306-2619(02)00176-9

Kalogirou, S. A. (2004). Solar thermal collectors and applications. *Progress in energy and combustion science*, *30*(3), 231-295. https://doi.org/https://doi.org/10.1016/j.pecs.2004.02.001

Kalogirou, S. A. (2013). *Solar energy engineering: processes and systems*. Academic press.

Kang, G.-U., & Chung, B.-J. (2010). The experimental study on transition criteria of natural convection inside a vertical pipe. *International communications in heat and mass transfer*, *37*(8), 1057-1063. https://doi.org/https://doi.org/10.1016/j.icheatmasstransfer.2010.06.016

Kanyowa, T., Nyakujara, G. V., Ndala, E., & Das, S. (2021). Performance analysis of Scheffler dish type solar thermal cooking system cooking 6000 meals per day. *Solar Energy*, *218*, 563-570. https://doi.org/https://doi.org/10.1016/j.solener.2021.03.019

Kitamura, K., & Kimura, F. (2008). Fluid flow and heat transfer of natural convection over upward-facing, horizontal heated circular disks. *Heat Transfer—Asian Research: Co-sponsored by the Society of Chemical Engineers of Japan and the Heat Transfer Division of ASME*, *37*(6), 339-351. https://doi.org/https://doi.org/10.1002/htj.20215

Kobus, C., & Wedekind, G. (1995). An experimental investigation into forced, natural and combined forced and natural convective heat transfer from stationary isothermal circular disks. *International journal of heat and mass transfer*, *38*(18), 3329-3339. https://doi.org/https://doi.org/10.1016/0017-9310(95)00096-R

Ktistis, P. K., Agathokleous, R. A., & Kalogirou, S. A. (2021). Experimental performance of a parabolic trough collector system for an industrial process heat application. *Energy*, *215*, 119288. https://doi.org/https://doi.org/10.1016/j.energy.2020.119288

Kulkarni, K., Havaldar, S., & Bhattacharya, N. (2021). Review on advance tubular receivers for central solar tower system. IOP Conference Series: Materials Science and Engineering,

Li, X., Kong, W., Wang, Z., Chang, C., & Bai, F. (2010). Thermal model and thermodynamic performance of molten salt cavity receiver. *Renewable Energy*, *35*(5), 981-988. https://doi.org/https://doi.org/10.1016/j.renene.2009.11.017

Liyew, K. W., Habtu, N. G., Louvet, Y., Guta, D. D., & Jordan, U. (2021). Technical design, costs, and greenhouse gas emissions of solar Injera baking stoves. *Renewable and Sustainable Energy Reviews*, *149*, 111392. https://doi.org/https://doi.org/10.1016/j.rser.2021.111392

Lizaso, M. (2020). A review of cooking technology around the world and the potential of solar cooking.

Maka, A. O., & Alabid, J. M. (2022). Solar energy technology and its roles in sustainable development. *Clean Energy*, *6*(3), 476-483. https://doi.org/https://doi.org/10.1093/ce/zkac023

Merchán, R., Santos, M., Medina, A., & Hernández, A. C. (2021). High temperature central tower plants for concentrated solar power: 2021 overview. *Renewable and Sustainable Energy Reviews*, 111828. https://doi.org/https://doi.org/10.1016/j.rser.2021.111828

Mulugeta, T. (2020). The Developmental Patterns of Injera Baking Stoves: Review on the Efficiency, and Energy Consumption in Ethiopia. *International Journal of Mechanical Engineering*, *7*(1), 7-16. https://doi.org/http://www.internationaljournalssrg.org/IJME/paper-details?Id=298

Murray, D. (2012). Small-scale solar central receiver system design and analysis. https://doi.org/https://doi.org/10.15368/theses.2012.110

Murray, D. J. (2012). *Small-scale solar central receiver system design and analysis* California Polytechnic State University].

Muthu, S., & Raman, R. (2006). Concentrated paraboloid solar cookers for quantity cookery. de Granada solar cooking conference,

Muthusivagami, R., Velraj, R., & Sethumadhavan, R. (2010). Solar cookers with and without thermal storage—a review. *Renewable and Sustainable Energy Reviews*, *14*(2), 691-701. https://doi.org/https://doi.org/10.1016/j.rser.2008.08.018

Negash, S., Omiogbemi, I., & Dagwa, I. (2021). Development of a partially automated electric injera baking stove with improved efficiency and production rate. AIP Conference Proceedings,

Newell, R., Raimi, D., & Aldana, G. (2019). Global energy outlook 2019: the next generation of energy. *Resources for the Future*, *1*(8).

Ortega, J. I., Burgaleta, J. I., & Téllez, F. M. (2008). Central receiver system solar power plant using molten salt as heat transfer fluid.

Owusu, P. A., & Asumadu-Sarkodie, S. (2016). A review of renewable energy sources, sustainability issues and climate change mitigation. *Cogent Engineering*, *3*(1), 1167990.

Pidaparthi, A. S. (2017). *Heliostat cost reduction for power tower plants* Stellenbosch: Stellenbosch University].

Rathan, N. S., Raut, A., & Rahul, B. G. (2021). Comparative Analysis of Various Insulation Materials for Building Envelope Components. IOP Conference Series: Earth and Environmental Science,

Ratlamwala, T., Dincer, I., & Aydin, M. (2012). Energy and exergy analyses and optimization study of an integrated solar heliostat field system for hydrogen production. *international journal of hydrogen energy*, *37*(24), 18704-18712.

Rawat, P. (2017). INTERNATIONAL JOURNAL OF ENGINEERING SCIENCES & RESEARCH TECHNOLOGY EXERGY PERFORMANCE ANALYSIS OF 300 W SOLAR PHOTOVOLTAIC MODULE.

Rizvi, A. A., Danish, S. N., El-Leathy, A., Al-Ansary, H., & Yang, D. (2021). A review and classification of layouts and optimization techniques used in design of heliostat fields in solar central receiver systems. *Solar Energy*, *218*, 296-311. https://doi.org/https://doi.org/10.1016/j.solener.2021.02.011

Saghafifar, M. (2016). Thermo-economic optimization of hybrid combined power cycles using heliostat solar field. *Masters Degree Thesis Submitted at College of Engineering American University of Sharjah*.

Seid, G. (2021). *Experimental Investigation of Concentrating Solar Baker Using Parabolic Trough Solar Collector Integrated with Thermal Energy Storage* ASTU].

Shah, R. K., & Sekulic, D. P. (2003). *Fundamentals of heat exchanger design*. John Wiley & Sons.

Sharma, C., Bohidar, S., & Sen, P. (2015). Study of solar energy & it's application in daily life. *International Journal of Advance Research in Science and Engineering (IJARSE)*(4).

Shyam, A. T., & Tiwari, G. (2018). Handbook of Solar Energy Theory, Analysis and Applications. In: Springer.

Siebers, D. L., & Kraabel, J. S. (1984). Estimating convective energy losses from solar central receivers. *United States*.

Slootweg, M., Craig, K., & Meyer, J. P. (2019). A computational approach to simulate the optical and thermal performance of a novel complex geometry solar tower molten salt cavity receiver. *Solar Energy*, *187*, 13-29. https://doi.org/https://doi.org/10.1016/j.solener.2019.05.003

Sonawane, P. D., & Bupesh Raja, V. (2018). An overview of concentrated solar energy and its applications. *International Journal of Ambient Energy*, *39*(8), 898-903. https://doi.org/http://dx.doi.org/10.1080/01430750.2017.1345009

Srilakshmi, G., Venkatesh, V., Thirumalai, N., & Suresh, N. (2015). Challenges and opportunities for Solar Tower technology in India. *Renewable and Sustainable Energy Reviews*, *45*, 698-709. https://doi.org/https://doi.org/10.1016/j.rser.2015.02.016

Suman, S., Khan, M. K., & Pathak, M. (2015). Performance enhancement of solar collectors—A review. *Renewable and Sustainable Energy Reviews*, *49*, 192-210. https://doi.org/https://doi.org/10.1016/j.rser.2015.04.087

Telsnig, T., Weinrebe, G., Finkbeiner, J., & Eltrop, L. (2017). Life cycle assessment of a future central receiver solar power plant and autonomous operated heliostat concepts. *Solar Energy*, *157*, 187-200. https://doi.org/https://doi.org/10.1016/j.solener.2017.08.018

Tiwari, G., & Tiwari, A. (2016). *Handbook of solar energy* (Vol. 498). Springer.

TSEGAYE, B. S. (2021). DESIGN OF MODEL REFERENCE ADAPTIVE PID CONTROLLER WITH CLAY-METAL PAN FOR INJERA MITAD USING INDUCTION HEATING.

Wah, H., & Kyaing, N. (2017). Design calculations of heliostat field layout for solar thermal power generation. 105th The IIER International Conference,

Weinrebe, G., Von Reeken, F., Wöhrbach, M., Plaz, T., Göcke, V., & Balz, M. (2014). Towards holistic power tower system optimization. *Energy Procedia*, *49*, 1573-1581. https://doi.org/doi:10.1016/j.egypro.2014.03.166

Xu, C., Wang, Z., Li, X., & Sun, F. (2011). Energy and exergy analysis of solar power tower plants. *Applied Thermal Engineering*, *31*(17-18), 3904-3913. https://doi.org/https://doi.org/10.1016/j.applthermaleng.2011.07.038

YOHANES, A. (2020). *MODELING AND EXPERIMENTAL TESTING OF SOLAR POWERED INJERA BAKING*

Yohannis, E. (2022). Design of Solar Thermal Injera Baking System Using Nano fluid as Heat Transfer Fluid. *American Journal of Bioscience and Bioinformatics*, *1*(1), 1-5.

Zhou, Y., & Zhao, Y. (2014). Heliostat field layout design for solar tower power plant based on GPU. *IFAC Proceedings Volumes*, *47*(3), 4953-4958. https://doi.org/https://doi.org/10.3182/20140824-6-ZA-1003.01581

APPENDIX:

Appendix A: Commonly used insulating materials thermal conductivity.

Table A. 1 Insulating materials thermal conductivity

Item)	**Material**	**Thermal Conductivity (W/m. K)**
1	Paraffin Wax	0.25
2	Rubber	0.35
3	Glass Wool	0.04
4	Glass Fiber	0.03
5	Epoxy	0.35
6	Ceramic fiber	0.08
7	Cotton	0.04
8	Coal	0.24
9	Cellulose	0.08
10	Alucobond	0.15
11	Acrylic	0.2
12	Aerogel	0.02
13	Bitumen	0.17
14	Calcium silicate	0.05
15	Vacuumed panel	0.007
16	Vermiculite	0.06
17	Perlite	0.05
18	Polystyrene (XPS)	0.08
19	Polyurethane	0.02
20	Plywood	0.13

Appendix B: The thermal characteristics of a few specific materials.

Table B. 1 Thermal characteristics of a few specific materials

Materials	**Density ρ (kg/m3)**	**Specific heat Cp(J/kg.k)**	**Thermal conductivity(K)**
Aluminum	2700	903	237
Copper	8930	385	388
Iron	7870	447	80.2
Lead	129	11,300	35.3
Silver	235	10,500	429
Soil	2050	1840	0.52
Tin	227	7310	66.6
Steel, Carbon 1%	7830	460	43
Steel, AISI302	8060	480	15.1

Appendix C: Assembly Drawing of Baker

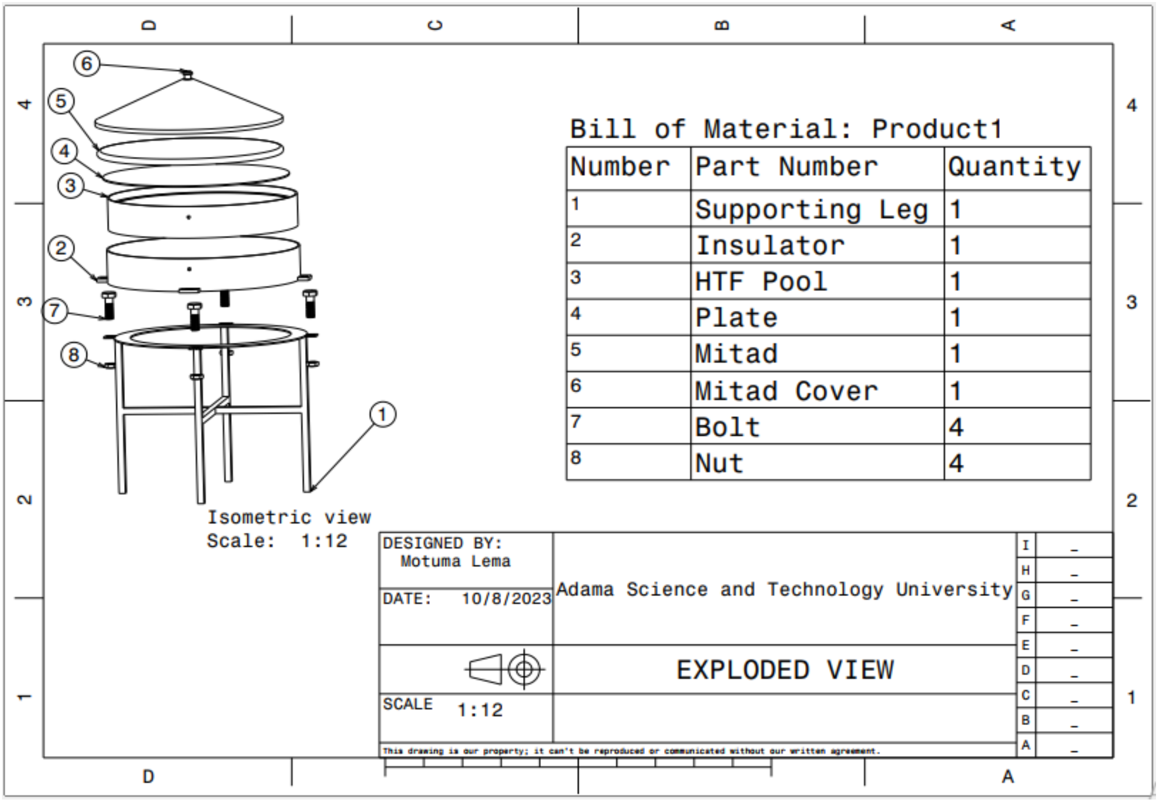

Figure C. 1 Exploded view of Baker

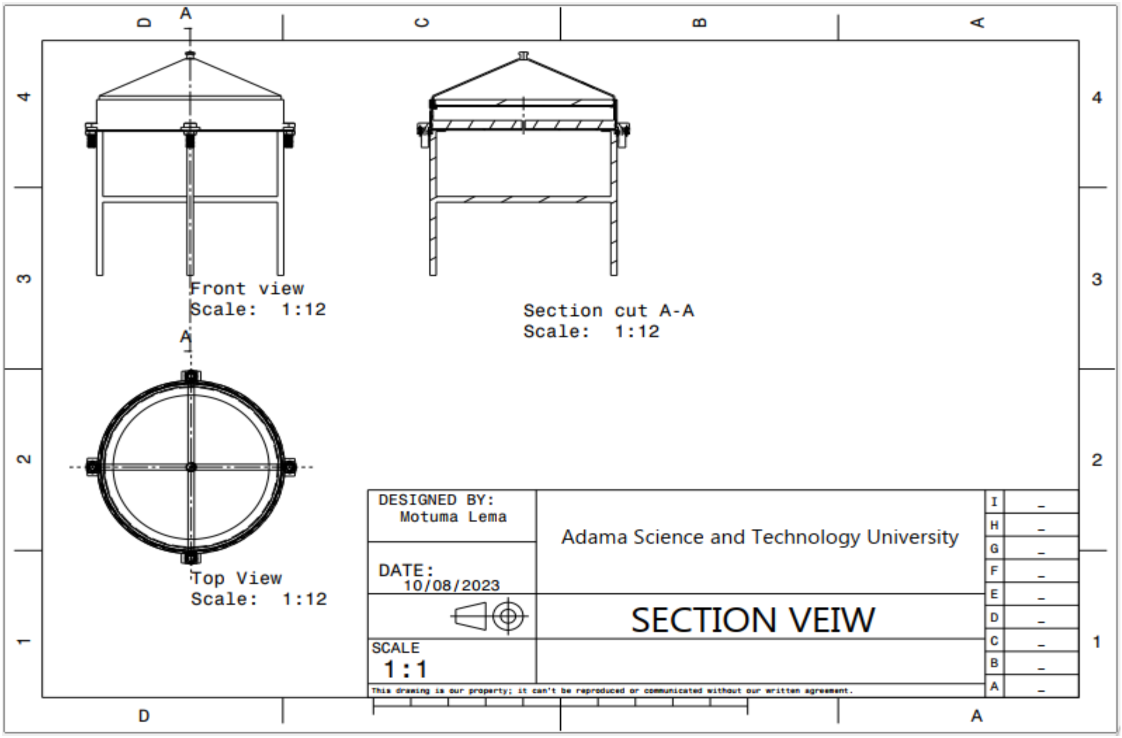

Figure C. 2 Section View of baker

Appendix C: Python code for transient analysis of the baking mitad.

```
import numpy as np

import matplotlib.pyplot as plt

# Parameters

pan_lengths = [0.004, 0.008, 0.012, 0.016, 0.02]

dt = 1

h = 28

k = 0.5

rho = 1325

cp = 900

T_inf = 18.64

# Storage for temperatures and heating times

T_hist_list = []
```

```
heating_times = []
for pan_length in pan_lengths:
    # Calculated parameters
    L = pan_length  # Total length (updated based on pan length)
    dx = 0.004  # Fixed pan thickness
    alpha = k / (rho * cp)  # Thermal diffusivity (m^2/s)
    Bi = h * dx / k  # Biot number
    Fo = alpha * dt / (dx ** 2)  # Fourier number
    # Grid
    nx = int(L / dx) + 1
    x = np.linspace(0, L, nx)
    # Initial condition
    T = T_inf * np.ones(nx)
    # Boundary conditions
    T[0] = 423  # °C
    # Storage for temperatures
    T_hist = []
    # Time loop
    time = 0
    reached_200 = [False] * nx  # List to track if each node has reached 200 degrees
    while time <= 1000:
        T_new = T.copy()
        # Interior nodes
        for i in range(1, nx - 1):
```

```
            T_new[i] = Fo * (T[i + 1] - 2 * T[i] + T[i - 1]) + T[i]

        # Convection boundary

        T_new[-1] = Fo * ((2 * Bi) * T_inf + 2 * T[-2] + (1 / Fo - 2 * Bi - 2) * T[-1])

        # Store temperatures

        T_hist.append(T_new)

        # Check if last node temperature reaches 200 degrees

        if not reached_200[-1] and T_new[-1] >= 200:

            heating_times.append(time)

            reached_200[-1] = True

        # Update

        T = T_new

        # Increment time

        time += dt

    T_hist_list.append(T_hist)

# Extract temperatures at the last node for each time step

last_node_temps = []

for T in T_hist_list:

    last_node_temps.append([T[-1] for T in T])

# Plot the temperature history at the last node

for i, pan_length in enumerate(pan_lengths):

    plt.plot(last_node_temps[i], label=f'Pan thickness: {pan_length} m, Heating time:
{heating_times[i]} sec ')

plt.xlabel('Time (Sec)')

plt.ylabel('Temperature (C)')
```

```
plt.title('Effect of pan thickness on heating time')

plt.legend()

plt.grid(True)  # Add grid to the plot

plt.show()

#Surface Temperature

# Parameters

L = 0.02

dx = 0.002

dt = 1

h = 28

k = 0.5

rho = 1325

cp = 900

T_inf = 18.64

# Calculated parameters

alpha = k / (rho * cp)  # Thermal diffusivity (m^2/s)

Bi = h * dx / k  # Biot number

Fo = alpha * dt / (dx ** 2)  # Fourier number

# Grid

nx = int(L / dx) + 1

x = np.linspace(0, L, nx)

# Initial condition

T = T_inf * np.ones(nx)

# Boundary conditions
```

```
T[0] = 423 # °C
# Storage for temperatures
T_hist = []
# Time loop
time = 0
reached_200 = [False] * nx  # List to track if each node has reached 200 degrees
while time <= 2000:
    T_new = T.copy()
    # Interior nodes
    for i in range(1, nx - 1):
        T_new[i] = Fo * (T[i + 1] - 2 * T[i] + T[i - 1]) + T[i]
    # Convection boundary
    T_new[-1] = Fo * ((2 * Bi) * T_inf + 2 * T[-2] + (1 / Fo - 2 * Bi - 2) * T[-1])
# Check if each node reaches 200 degrees
    for i in range(nx):
        if T_new[i] >= 200 and not reached_200[i]:
            reached_200[i] = True
            print(
                "Node {} ({} mm) reached 200 degrees Celsius at time {} seconds.".format(
                    i, round(i * dx * 1000, 2), time
                ))
    # Store temperatures
    T_hist.append(T_new)
    # Update
```

```
    T = T_new
    # Increment time
    time += dt
# Extract temperatures at the last node for each time step
last_node_temps = []
for T in T_hist:
    last_node_temps.append(T[-1])
# Plot the temperature history at the last node
plt.plot(last_node_temps, label='Pan Surface Temperature')
plt.xlabel('Time (Sec)')
plt.ylabel('Temperature (C)')
plt.legend()
plt.grid(True)  # Add grid to the plot
plt.show()
#Baking Time
# Parameters
L = 0.004  # Thickness of the Injera (m)
dx = 0.001  # Spatial step size (m)
dt = 1  # Time step size (s)
k = 0.6  # Thermal conductivity of the dough (W/(m K))
rho = 1160.5  # Density of the dough (kg/m^3)
cp = 3096  # Specific heat capacity of the dough (J/(kg K))
T_inf = 18.64  # Ambient temperature (°C)
# Calculated parameters
```

```
alpha = k / (rho * cp)  # Thermal diffusivity (m^2/s)

Bi = 222 * dx / k  # Biot number

Fo = alpha * dt / (dx ** 2)  # Fourier number

# Grid

nx = int(L / dx) + 1

x = np.linspace(0, L, nx)

# Initial condition

T = T_inf * np.ones(nx)

# Boundary conditions

T[0] = 200  # Initial temperature at the bottom boundary (°C)

# Storage for temperatures

T_hist = []

# Time loop

time = 0

while time <= 180:

    T_new = T.copy()

    # Interior nodes

    for i in range(1, nx - 1):

        # Finite difference scheme for heat conduction

        T_new[i] = Fo * (T[i + 1] - 2 * T[i] + T[i - 1]) + T[i]

    # Convection boundary condition

    T_new[-1] = Fo * ((2 * Bi) * T_inf + 2 * T[-2] + (1 / Fo - 2 * Bi - 2) * T[-1])

    # Store temperatures

    T_hist.append(T_new)
```

```
    # Update temperature
    T = T_new
    # Increment time
    time += dt
# Extract temperatures at the last node for each time step
last_node_temps = []
for T in T_hist:
    last_node_temps.append(T[-1])
# Plot the temperature history at the last node
plt.plot(last_node_temps, label='Injera baking Temperature VS Time')
plt.xlabel('Time (s)')
plt.ylabel('Temperature (°C)')
plt.legend()
plt.grid(True)  # Add gridlines to the plot
plt.show()
#Re-heating Time
# Parameters
L = 0.02  # Length of the pan (m)
dx = 0.002  # Spatial step size (m)
dt = 1  # Time step size (s)
h = 28 # Convective heat transfer coefficient (W/(m^2 K))
k = 0.5  # Thermal conductivity of the pan material (W/(m K))
rho = 1325  # Density of the pan material (kg/m^3)
cp = 900  # Specific heat capacity of the pan material (J/(kg K))
```

```
T_inf = 18.41  # Ambient temperature (C)

# Calculated parameters

alpha = k / (rho * cp)  # Thermal diffusivity (m^2/s)

Bi = h * dx / k  # Biot number

Fo = alpha * dt / (dx ** 2)  # Fourier number

# Grid

nx = int(L / dx) + 1

x = np.linspace(0, L, nx)

# Initial condition

T = np.linspace(432, 180, nx)

# Storage for temperatures

T_hist = []

# Time loop

time = 0

while time <= 2000:

    T_new = T.copy()

    # Interior nodes

    for i in range(1, nx - 1):

        # Finite difference scheme for heat conduction

        T_new[i] = Fo * (T[i + 1] - 2 * T[i] + T[i - 1]) + T[i]

    # Convective boundary condition

    T_new[-1] = Fo * ((2 * Bi) * T_inf + 2 * T[-2] + (1 / Fo - 2 * Bi - 2) * T[-1])

    # Store temperatures

    T_hist.append(T_new)
```

```
    # Update temperature
    T = T_new
    # Increment time
    time += dt
# Extract temperatures at the last node for each time step
last_node_temps = []
for T in T_hist:
    last_node_temps.append(T[-1])
# Plot the temperature history at the last node
plt.plot(last_node_temps, label='Pan Surface Temperature')
plt.xlabel('Time (s)')
plt.ylabel('Temperature (°C)')
plt.legend()
plt.grid(True)  # Add gridlines to the plot
plt.show()
```